LUND UNIVERSITY

Probing Electron Collisions in Nanostructures

Damtie, Fikeraddis

2017

Link to publication

Citation for published version (APA):
Damtie, F. (2017). *Probing Electron Collisions in Nanostructures*. [Doctoral Thesis (compilation), Mathematical Physics]. Lund University, Faculty of Science, Department of Physics.

Total number of authors:
1

General rights
Unless other specific re-use rights are stated the following general rights apply:
Copyright and moral rights for the publications made accessible in the public portal are retained by the authors and/or other copyright owners and it is a condition of accessing publications that users recognise and abide by the legal requirements associated with these rights.
• Users may download and print one copy of any publication from the public portal for the purpose of private study or research.
• You may not further distribute the material or use it for any profit-making activity or commercial gain
• You may freely distribute the URL identifying the publication in the public portal

Read more about Creative commons licenses: https://creativecommons.org/licenses/

Take down policy
If you believe that this document breaches copyright please contact us providing details, and we will remove access to the work immediately and investigate your claim.

LUND UNIVERSITY

PO Box 117
221 00 Lund
+46 46-222 00 00

Probing Electron Collisions in Nanostructures

FIKERADDIS AHMED DAMTIE
DEPARTRMENT OF PHYSICS | FACULTY OF SCIENCE | LUND UNIVERSITY

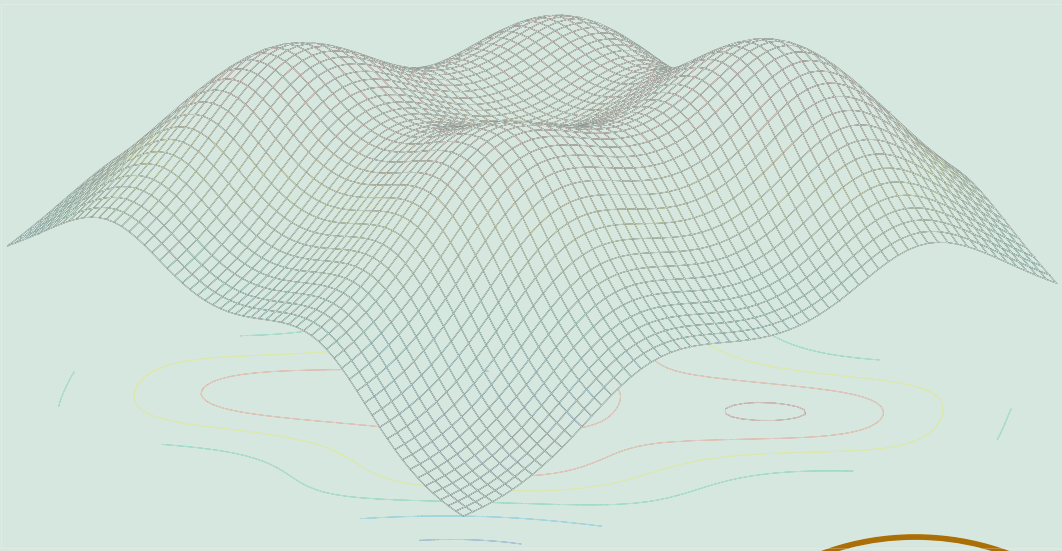

Probing Electron Collisions in Nanostructures

Probing Electron Collisions in Nanostructures

by Fikeraddis Ahmed Damtie

LUND
UNIVERSITY

Thesis for the degree of Doctor of Philosophy
Thesis advisors: Prof. Andreas Wacker, Assoc.Prof. Peter Samuelsson
Faculty opponent: Prof. Tilmann Kuhn

To be presented, with the permission of the Faculty of Science of Lund University, for public criticism in the Rydberg lecture hall (Rydbergsalen) at the Department of Physics on Wednesday, 31 of May 2017 at 09:00

Organization
LUND UNIVERSITY
Department of Physics
Box 118
SE–221 00 LUND
Sweden

Author(s)
Fikeraddis Ahmed Damtie

Document name
DOCTORAL DISSERTATION

Date of disputation
2017-05-31

Sponsoring organization

Title and subtitle
Probing Electron Collisions in Nanostructures:

Abstract
This thesis studies the role of interaction between charged particles for transport and optical properties in nanostructures. Simulations are provided for a quantitative description of the system dynamics probed by either current spectroscopy or light absorption. In the first part of the thesis (Part I) the basic theories are described and in the second part of the thesis (Part II) the papers listed below are presented.

Paper I studies the effect of different types of electron-electron interaction terms in triple quantum dot transport.

Paper II describes a method of calculating the yield for a quantum dot model due to Multiple Exciton Generation (MEG) which is an effect of electron-electron interaction.

Paper III suggests optimization schemes for an efficient yield due to Multiple exciton generation in Nanocrystal quantum dots.

Paper IV describes two dimensional spectroscopy based on phase modulation technique to study the dynamics of ultrafast processes in nanostructures in real time.

Key words
Electron-Electron Interaction, Time Dependent Dynamics, Multiple Exciton Generation, Two dimensional Spectroscopy

Classification system and/or index terms (if any)

Supplementary bibliographical information

Language
English

ISSN and key title

ISBN
978-91-7753-206-4 (print)
978-91-7753-207-1 (pdf)

Recipient's notes

Number of pages
159

Price

Security classification

Distributor
Fikeraddis A. Damtie, Division of Mathematical Physics, Department of Physics, Sölvegatan 14A, SE-223 62 Lund, Sweden

I, the undersigned, being the copyright owner of the abstract of the above-mentioned dissertation, hereby grant to all reference sources the permission to publish and disseminate the abstract of the above-mentioned dissertation.

Signature _____ Date 2017-04-21

DOKUMENTDATABLAD enl SIS 61 41 21

Probing Electron Collisions in Nanostructures

by Fikeraddis Ahmed Damtie

LUND
UNIVERSITY

A doctoral thesis at a university in Sweden takes either the form of a single, cohesive research study (monograph) or a summary of research papers (compilation thesis), which the doctoral student has written alone or together with one or several other author(s).

In the latter case the thesis consists of two parts. An introductory text puts the research work into context and summarizes the main points of the papers. Then, the research publications themselves are reproduced, together with a description of the individual contributions of the authors. The research papers may either have been already published or are manuscripts at various stages (in press, submitted, or in draft).

Cover illustration: Real part of the double quantum coherence two-dimensional spectrum at zero population time. Adapted from paper IV.

Funding information: The thesis work was financially supported by NanoLund, Knut and Alice Wallenberg Foundation (KAW) and the Swedish Research Council (VR).

© Fikeraddis Ahmed Damtie 2017

Faculty of Science, Department of Physics

ISBN: 978-91-7753-206-4 (print)
ISBN: 978-91-7753-207-1 (pdf)

Printed in Sweden by Media-Tryck, Lund University, Lund 2017

Dedicated to my Parents

Contents

List of publications and author's contributions iv

Acknowledgments vii

Popular summary in English ix

I Background and Theory 1

1 Introduction 3

2 Transport in quantum dots 9
- 2.1 Current Spectroscopy for Single Quantum Dot . . . 10
- 2.2 Quantum Master Equations . . . 14
- 2.3 Equation of Motion for the Density Matrix. . . . 17
- 2.4 Pauli Master Equation . . . 19
- 2.5 Coulomb Matrix Element Calculations for Triple Quantum Dots . . . 20

3 Exciton Dynamics 27
- 3.1 Excitons . . . 27
- 3.2 Excitons in Nanostructures . . . 28
- 3.3 Calculation of Energy Levels and Dipole Matrix Elements . . . 30
- 3.4 Dipole Matrix Elements . . . 35
- 3.5 Pulse Parameters . . . 38

4 Multiple Exciton Generation and Extraction 41
- 4.1 Multiple Exciton Generation (MEG) . . . 41
- 4.2 MEG Yield (Paper II) . . . 42
- 4.3 MEG Yield Optimization with Extraction and Injection (Paper III) . . . 48

5 Two Dimensional Spectroscopy 55
- 5.1 Our Approach for Calculating 2D Signals . . . 56
- 5.2 2D Data Collection and Analysis Example . . . 59
- 5.3 Double Sided Feynman Diagrams . . . 69
- 5.4 Study of Dynamics using 2D Spectroscopy (Paper IV) . . . 75

6 Discussion and Outlook 77

References 79

II The papers 89

Paper I: Transport in Serial Spinful Multiple-Dot Systems: The Role of Electron-Electron Interactions and Coherences. 91

Paper II: Time Dependent Study of Multiple Exciton Generation in Nanocrystal Quantum Dots. 107

Paper III: Optimization Schemes for Efficient Multiple Exciton Generation and Extraction in Colloidal Quantum Dots. 119

Paper IV: Simulation of Two Dimensional Spectroscopy for Excitonic Systems Based on Phase Modulation Technique. 127

List of publications and author's contributions

This thesis is based on the following publications, referred to by their Roman numerals:

I **Transport in Serial Spinful Multiple-Dot Systems: The Role of Electron-Electron Interactions and Coherences.**

Bahareh Goldozian, **Fikeraddis A. Damtie**, Gediminas Kiršanskas and Andreas Wacker
Scientific Report, 6, 22761 (2016)

©2016 Nature Publishing Group

In this paper the effects of different terms in the electron-electron interaction terms on transport in the triple quantum dot structure was studied.
Contribution: I calculated the Coulomb matrix elements for the electron-electron interaction. I also participated in writing and reviewing of the manuscript.

II **Time Dependent Study of Multiple Exciton Generation in Nanocrystal Quantum Dots.**

Fikeraddis A. Damtie, and Andreas Wacker
Journal of Physics: Conference Series, 696, 012012 (2016)

Published 2016 under license (CC-BY) by American Institute of Physics

In this work the quantum yield for a PbS quantum dot was calculated by evaluating the ratio between the total number of recombined electron-hole pairs and the number of absorbed photons with an energy about 3 times the band gap. A yield which is comparable to experimental values for quantum dots was obtained.

Contribution: I performed all simulations and produced all figures. I also wrote the first draft of the manuscript.

III **Optimization Schemes for Efficient Multiple Exciton Generation and Extraction in Colloidal Quantum Dots.**

Fikeraddis A. Damtie, Khadga J. Karki, Tõnu Pullerits and Andreas Wacker
The Journal of Chemical Physics, 145, 064703 (2016)

©2016 AIP Publishing LLC

Here optimization schemes for an efficient yield due to multiple exciton generation in nanocrystal quantum dots are described.

Contribution: I adapted the program, performed all simulations and produced all figures. I also wrote the first draft of the manuscript.

IV **Simulation of Two Dimensional Spectroscopy for Excitonic Systems Based on Phase Modulation Technique.**

Fikeraddis A. Damtie, Tõnu Pullerits, Andreas Wacker and Khadga J. Karki
Draft

©2017 the authors

In this work two dimensional spectroscopy based on the phase modulation technique is used to study the dynamics of ultrafast processes in nanostructures in real time.

Contribution: In cooperation with Khadga Karki (division of Chemical Physics) I initiated the project. I modified an existing code for calculating two dimensional spectra. I also produced all figures in time domain and wrote the first draft.

All papers are reproduced with permission of their respective publishers.

Acknowledgments

During my study time in Lund, many people have directly or indirectly contributed for the completion of this thesis. I will try to mention some of the people that contributed the most and if I forget some names, it is not intentional.

First and foremost, I would like to thank my supervisor Andreas Wacker for introducing me to the field of quantum transport since the start of my master thesis. I benefited enormously over the years from his scientific supervision and very useful advices. Andreas has always been available for discussions even on personal matters whenever I needed it. Thank you very much Andreas!

I am also very thankful to my collaborators, Khadga Karki and Tõnu Pullerits from the division of chemical physics and Bahareh Goldozian and Gediminas Kiršanskas from our group. From the collaborations with Khadga and Tõnu, I learned important lessons about exciton dynamics and multi-dimensional spectroscopy. In addition, I also benefited from the various group meetings with the past and current members of our group; Olov, Martin, David, Susanna, Kevin, Tim, and Alex.

The division of mathematical physics feels like one big family thanks to the all the staff members. Special thanks to Peter Samuelsson who is also my second supervisor for common group seminars, personal advices and good administration as the head of the division. I would also like thank all the seniors in the division: Sven Åberg, Claudio Verdozzi, Ferdi Aryasetiawan, Stephanie Reimann and Gillis Carlsson from whom I have learned in one way or the other through courses, seminars and meetings.

When it comes to practical matters, Katarina Lindqvist has always been very helpful. Thank you very much Katarina for all practical advises and help. Florido and Lennart have been helpful in fixing all sorts of computer related problems.

Gunnar Eriksson, whom I shared office since the time I did my master thesis has taught me the Swedish language and culture over the years. I also enjoyed discussing physics and different tips on computers and programming. Many thanks to Gunnar for organizing a

trip to the ”northern” part of Sweden, where we were welcomed by his parents. My office mates, Emil, Tineke, and Asimina, thank you for the time we had in the office. Emil also contributed to my Swedish vocabulary since we moved to *B*317.

I enjoyed sharing good experiences with all PhD students and post-docs at the division on many occasions. To mention some names here; Ognjen and Gediminas (special thanks for reading and giving valuable comments during my thesis writing), Miroslav, Joseph, Sara, Jakob, Johannes, Daniel, Florinda, both Fredriks and Martin.

Special thanks to Cecilia Jarlskog for very broad and interesting discussions on scientific and non-scientific topics at several occasions, even during weekends.

I came from an extended family and it is not possible to list everyone here. I thank my parents, Ahmed Damtie and Tsehaynesh Dagne for all the love they have given me. My siblings, Yonatan, Abel, Natnael and Sofia have all been a constant source encouragement. I always feel lucky to have you all. My niece (Soliana) and nephew (Kirubel) make me laugh every time we call each other.

Bekele and Fikirte's family have always been welcoming me in their home on many holiday occasions in Norway. I thank the Ethiopian community in Lund with whom I attended several social events.

Yohannes, Maedn and their family in Eslöv, including Robel, Endreas and Haile, thank you for being good friends. I also would like to thank Wondwosen, Alem, Solomon, Nebiyu and Mahlet, Getu, Mulugeta, Tes, Befikadu , Simon, and their families for the good times in Lund.

My friends outside Lund, Tseganeh, Abrham, Getch, Sami and Betel thank you all for the good conversations. Special thanks for my student corridor mates Christian Nilsson and Oliver kruz, for all the good times during and after my time in the student corridor.

Popular summary in English

We live in a time of wireless technologies, robotics and small computers with very high computing power. This is mainly due to a large emphasis given towards the study of semiconductor materials which are the building blocks of today's electronic industry. One of the secrets behind creating faster computers is the ability to integrate more and more transistors on a small semiconductor chip. Gordon Moore, the co-founder of Intel predicted in 1965 that the number of transistors per integrated circuit will be doubled every two years. His prediction accurately worked for several decades. To fit in large number of transistors in a small computer chip, a reduction in the size of the transistors is a key. This is where the emergence of a relatively newer field of technology comes in to play, nano engineering. With nano engineering, transistors as small as few nm size can be fabricated. In 2016 Intel has reported a processor where 7.2 billions of transistors integrated only on a $456mm^2$ area chip.

As the size of the transistors gets smaller and smaller, the laws of physics governing the motion of charge carriers through the devices has to be modified compared to larger transistors. One of the most common experimental setup is the measurement of current through the device which is connected to a potential difference (voltage).

In macroscopic size electronic circuits, the dependence of the current on the applied voltage can be either linear or non-linear depending on the circuit elements. For a regular resistance, such as light bulb, the current is linearly proportional to the applied voltage (Ohm's law). However, if the circuit is composed of non-linear elements such as transistors or diodes, the dependence of the current on the applied voltage is non-linear, but typically the current increases with bias. This situation is different in nano scale electronic devices which are characterized by discrete energy levels due to confinement. In this case the current displays discrete peaks which are dependent on the accessibility of energy levels for the applied bias.

In the first part of this thesis, a study of electron transport properties of quantum dots has been performed. Due to confinement, the electron-electron (ee) interaction is enhanced in quantum dots compared to macroscopic size devices. As a result, understanding and

careful description of the interaction types and their strength to the transport of charge carriers through the device is of great importance. One peculiar behavior in nanoscale devices is that the ee interaction becomes a factor that greatly determines the transport behavior across these devices.

In the second part of the thesis, interaction of light with nanostructures is studied with the aim of simulating the microscopic physical processes in efficient quantum dot based solar cells. The photovoltaic effect in which a material generates an electric current as a result of exposure to light has been known for more than a century. Many countries are now giving priorities for utilization of renewable energy sources for electric power generation. Semiconductor based solar cells have already been used to convert solar energy to a usable form of electric current. However, they are not as popular yet as fossil fuel due to their limited efficiency. In 1961 a famous work by William Shockley and Hans Queisser puts a limit on the maximum theoretical conversion efficiency of a solar cell using a single p-n junction to be not more than 33.7%. Finding possibilities to circumvent the Shockley-Queisser limit is an active area of current research.

In recent years, quantum-dot based solar cells demonstrated enhanced conversion efficiency. An understanding on a microscopic level how the charge carriers and the light field interacts in quantum dot based solar cells plays a key role in the design of the future solar cells. One mechanism which is described in this thesis is the multiple exciton generation (MEG) in which a generation of more than one electron-hole pairs (exciton) per absorbed photon enhances the conversion efficiency.

Part I

Background and Theory

Chapter 1

Introduction

The semiconductor industry has shown a rapid growth in the past couple of decades with an increased capability of fabricating nanostructures. Quantum dots, nanowires, nanoparticles are among the most common forms of nanostructures which are characterized by a size that ranges between microscopic and molecular size at least in one dimension. Their wide range of technological applications in modern electronics industries has been a driving factor for the ever increasing popularity of nanostructures. These days, one can buy Light Emitting Diodes (LED) and Television displays that are made from quantum dots [1]. In addition, their potential applications in photovoltaic devices [2–4], quantum computing [5], biology and medical imaging [6], optics [7] etc., make quantum dots and other forms of nanostructures exceptionally useful in the future.

The potential future applications for nanostructures demand a systematic study of how they work as part of an integrated system. Due to their small dimensions, quantum effects become important and their operation mechanism can not be fully explained with the laws of classical mechanics. Quantization of conductance [8–12], [13, 14],and exciton formation [15, 16] are some of the quantum effects that become dominant as a consequence of confinement in nanostructures. As a result one needs to employ the laws of quantum mechanics to explain and predict the operation of nanostructures.

The interaction of charged particles in low dimensional structures is enhanced compared to their bulk counterparts due to confinement [16]. The electron-electron (ee) interaction energy scales as an inverse length which is more significant at smaller separations between the interacting particles.

These interactions play a major role in describing important physical processes in solid state systems. The electron transport in quantum dots can be modified greatly due to interaction. This can have an effect of blockade or transparency depending on the geometry

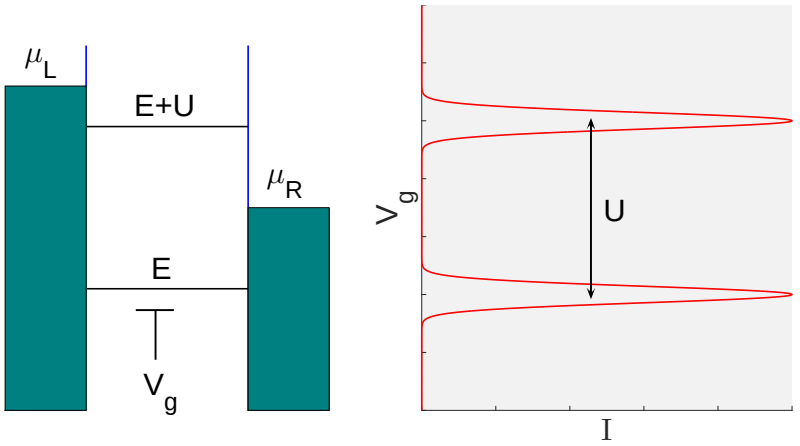

Figure 1.1: Energy level diagram of a quantum dot coupled to metallic leads under biasing condition (left) and the corresponding current spectrum as a function of gate voltage (right). The distance between the peaks in the I-V curve reveals the interaction strength if changes in quantization energy are negligible.

and arrangement of the dots and the environment.

In spectroscopic measurements changes in the system behavior can be probed (measured) via different techniques. Two different probing techniques are discussed in this thesis. The first probing technique is to study the current or conductance as a function of applied voltages. In quantum dots at low temperature the current is non-zero as long as there is an available state within the bias window ($\mu_L - \mu_R$), where μ_L and μ_R are the chemical potentials of the left and right leads respectively. For a fixed bias voltage $V_{bias} = (\mu_L - \mu_R)/e$, where e is the electron charge, the level energies within the dot can be controlled by varying the gate voltage V_g (cf. Fig. 1.1 (left)). In the linear response regime (with $V_{\text{bias}} \ll U/e$) [12] as shown in Fig. 1.1 (right) a peak in the current appears for each available state within the bias window. The distance between these peaks corresponds to the Coulomb charging energy needed to add one extra charge to the dot. Hence the name Coulomb oscillation. A more detailed information can also be obtained by using a two dimensional scan as a function of the gate and bias voltage to produce the so-called Coulomb diamonds [17, 18].

The second probing technique is to study optically the change in the emission and absorption spectrum of the system as a result of interaction with a light field. Several linear and non-linear spectroscopic techniques exist for studying the dynamics and structures of nanostructures and molecules. One of the simplest type of experiment in this regard is to study a two-level system coupled with an oscillating light field. The resulting population of the two levels as a function of time exhibit the so-called Rabi-oscillation [19, 20]. As shown in Fig. 1.2 information about the system such as the level splitting can be obtained

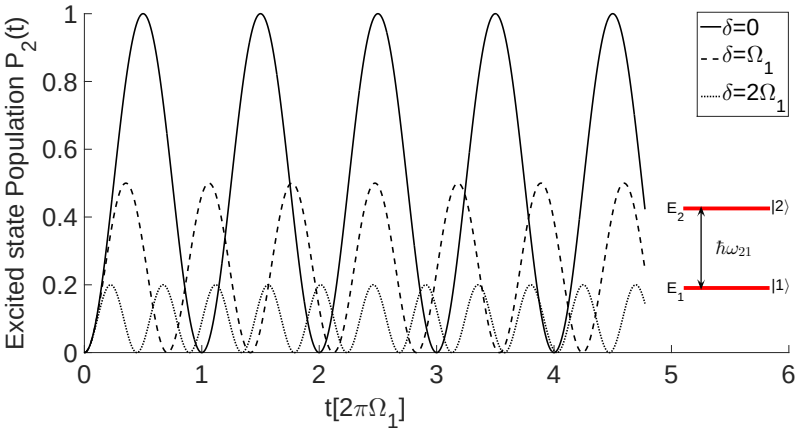

Figure 1.2: Rabi oscillations for the population of the excited $P_2(t)$ state in a two level system, $P_2(t) = \frac{\Omega_1^2}{\Omega_1^2+\delta^2}\sin^2(\frac{\Omega}{2}t)$ following Ref. [20]. $\delta = \omega - \omega_{21}$ is the detuning, which is the difference between the level splitting $\hbar\omega_{21} = E_2 - E_1$ and the pulse frequency $\omega = 3\Omega_1$ assumed here. $\delta = 0$ is the resonance condition in which the driving frequency matches the level splitting. $\Omega_1 = \mu_{12}E_0$ is the Rabi-frequency. For larger detunings δ the oscillation frequency $\Omega = \sqrt{\Omega_1^2 + \delta^2}$ increases.

by looking at the oscillation frequencies and amplitudes. In excitonically coupled systems the oscillations can indicate the strength of the Coulomb coupling between excitons.

One potential application of quantum dots is their usability as a building block in efficient solar cells. The solar spectrum covers a range of frequencies in the electromagnetic spectrum ranging from infrared to ultraviolet (see Fig. 1.3). For any type of single junction solar cell the maximum percentage of power converted to electrical energy from solar radiation is about 33% which is also called the Shockley-Queisser limit [21]. The rest of the radiation, about 67%, is lost due to several reasons. As discussed in Ref. [22] there are two major intrinsic losses and few other extrinsic losses which can be eliminated.

The first intrinsic loss is due to the mismatch between the broad solar spectrum and the gap energy of single junction solar cells. Photons with smaller energies than the band gap $\hbar\omega < E_g$ can not be absorbed. An absorbed photon with energy higher than the band gap $\hbar\omega > E_g$ can generate an electron-hole pair which will immediately loose almost all energy in excess of the band gap by emitting phonons, which heat the lattice.

The second intrinsic loss is due to radiative recombination of newly created electrons and holes. Some of the extrinsic losses that can limit solar cell efficiency are reflection, contact shadowing, series resistance etc.

Ross and Nozik in 1982 [23] pushed the limit of theoretical conversion efficiency up to 66%

for single junction solar cells by their suggestion to collect the hot carriers before relaxation in the form of heat. The hot carriers are "hot" in the sense that they have large kinetic energy as a result of absorbing a photon with energy much larger than the band gap energy.

Several proposals have been suggested to improve the efficiency of solar cells beyond the Shockley-Queisser limit [21]. A recent review on various aspects of optical energy conversion is given in Ref. [24]. Some of the proposals include the following techniques: The use of multijunction photovoltaic cells (also called "tandem cells") [25]. Concentration of the absorbed sunlight using lenses and curved mirrors onto a small multijunction solar cells [26]. Intermediate band photovoltaics in which the solar cells incorporate an energy band that is partially filled within the gap to let photons with less energy than the band gap to be absorbed [27]. Hot electron capture where a carrier after excitation with photon energy way above the band gap is extracted before relaxing to the band edge with special contacts [28]. Photon upconversion in which a special material is introduced in the module which can absorb two or more photons with energy below the band gap and emit one photon with energy above the band gap [29] and finally Multiple exciton generation (MEG) [3, 4, 28, 30–35].

MEG sometimes also called carrier multiplication is a physical process in which absorption of a high energy photon results in a creation of more electron-hole pairs by the excess energy instead of dissipating as heat. This process is mainly due to ee interaction in which the initial high energy exciton is disintegrated via inverse Auger recombination into two excitons with lower energy. A conversion efficiency as high as 44% for single sun and 85% for maximum concentration (46300 suns) has been demonstrated via MEG for quantum dots of various small band gap samples [36]. The MEG effect is enhanced in nanostructures compared to their bulk materials due to larger Coulomb interaction and the absence of requirements for momentum conservation.

This thesis is organized as follows: In chapter two the basic theory for calculating transport through coupled quantum dot is discussed. Since the calculations are based on the density matrix approach, introduction to the basics of density matrix and equation of motion for the density matrix is given in the beginning. Following the introduction of the density matrix, the model Hamiltonian is explained. Since the main focus of paper I is the study of the effects of different ee interaction terms for transport calculation, the Coulomb matrix elements and their evaluation for triple quantum dot of a given dimension is discussed in chapter two.

Chapter three begins by introducing the theory of excitons, which are the main subject of paper II and paper III. In addition, an outline of the calculations for evaluating the energy levels, Coulomb and dipole transition matrix elements for the model systems used in paper II and paper III is described. Chapter four discusses the method used for calculating MEG yield with and without a contact. Here the results obtained in Paper II and paper

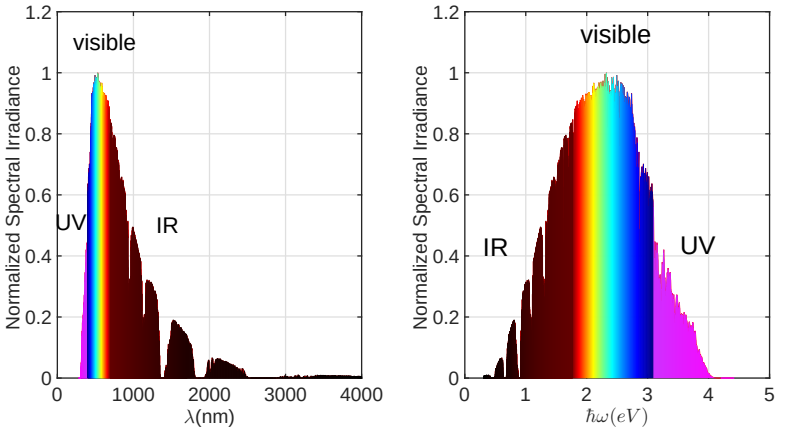

Figure 1.3: Direct solar irradiance based on the data from Ref. [37] in wavelength (left) and in energy (right).

III are summarized and discussed. Chapter five describes a method of two-dimensional spectroscopy, which is one of the extensively used techniques to measure ultra-fast processes in quantum dots and molecules. Finally, in chapter six an outlook and a conclusion is given.

Chapter 2

Transport in quantum dots

The topic of electron transport in nanostructures has been an active area of research in recent years following the rapid growth in fabrication methods of nanostructures. A typical theoretical challenge in this regard is the description of charge and energy transport through a quantum system coupled to electron reservoirs (metallic leads). The quantum system can be a single or coupled system which is characterized by discrete energy levels. The metallic leads on the other hand are considered to be composed of non-interacting electrons that obey the Fermi-Dirac distribution.

As already mentioned in the introduction chapter, current spectroscopy could provide sufficient information about transport of electrons through single and coupled quantum dots connected to metallic contacts. In paper I we investigated the effect of different electron-electron (ee) interaction terms in electron transport through a serially coupled triple quantum dot attached to metallic leads. One of the most common ways of representing measurement data in current spectroscopy is by using charge stability diagrams [38]. These diagrams are sometimes called Coulomb diamonds in the case of single quantum dot attached to metallic leads. The name "diamond" is due to the shapes of Coulomb blockade regions in the two dimensional plot of current as a function of gate voltage and bias voltage (see Fig. 2.1).

This chapter discusses the methods used to calculate the current through a triple quantum dot system with an emphasis on the effect of ee interaction on transport. Before discussing the transport calculation for coupled quantum dots, a brief motivation on the information that can be obtained via current spectroscopy through a single quantum dots is given in the following section.

2.1 Current Spectroscopy for Single Quantum Dot

The motivation in this section is to give an overview of the type of information obtained via current measurements by focusing only on transport through single quantum dot. The common setup is that a quantum dot is connected to metallic source and drain leads both from left and right to create an applied bias. By varying the chemical potential on the leads, a bias window can be opened or closed. In addition, the energy levels in the dot can be varied by changing the gate voltage V_{gate}. By raising or lowering the gate voltage, additional electrons can be added into or removed from the dot.

In Fig. 2.1 a plot of current (in the left) and differential conductance (in the right) as a function of the gate energy and the difference in the right and left chemical potential (bias energy) is shown. The current is calculated as the net flow of electrons through the left lead for an arbitrary parameter sets (given in the caption). The Pauli master equation approach is used to calculate the current, which will be discussed later in this chapter.

The charge stability diagrams in Fig. 2.1 provide a large amount of information on conditions of the gate energy with respect to the bias energy. This way one can identify regions on the two dimensional map where current is non zero or blocked. Fig. 2.1 displays the basic principle of the transport mechanism with Coulomb blockade. On the x-axis the bias is varied symmetrically. This is done by increasing the difference in the left/right chemical potentials. For positive bias the chemical potential for the left lead is positive and the chemical potential for the right lead is negative with the same magnitude. On the y-axis the dot energies are varied. By pulling downward the gate voltage, new states can enter the bias window.

Figure 2.2 shows the scenario for some selected points (A-F) on the two dimensional plot in Fig. 2.1(left). The points for zero (low) bias (A, C and E) are colored light green, the points that correspond to positive bias (B and F) are colored light red and the point that correspond to negative bias (D) is colored light blue. At points (A and C) the net current is zero as it is equally probable to tunnel through either side of the leads. The number of electrons in the dot is fixed in the diamond or Coulomb blockade regions indicated by light green in Fig. 2.1(left). On the boundary points between two diamonds, such as point (A), the number of particles in the dot fluctuates between N and $N+1$. In the specific model used in Fig. 2.1, the number of particles varied from zero to four. At point (E) the total number of electrons in the dot is 1. For the next level to come to the bias window at this point, one needs to pull downward the dot chemical potential by an amount proportional to the charging energy U plus separation between the levels ΔE.

By increasing the bias window, non-zero current can be obtained for regions outside the Coulomb blockade diamonds. For very large bias, more than one level can be in the bias window giving multiple transport channels which result in a finite current. This behavior

can be observed as we go further in the bias with more enhanced current signals. In experimental measurements, it is very common to represent the data in terms of differential conductance as shown in Fig. 2.1(right). In differential conductance plots the border lines of the Coulomb diamonds are more visible. One obtains information such as the charging energy and level splitting by measuring the width and height of the Coulomb diamonds.

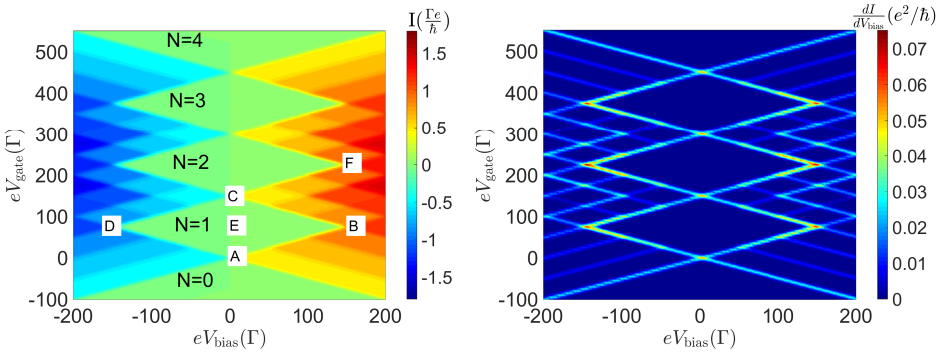

Figure 2.1: Current (left) and the corresponding differential conductance (right) as a function of bias and gate energy for a single quantum dot attached to two metallic leads. Coulomb blockade areas with fixed number of particles are indicated in diamond shapes. The size of each diamond is proportional to the interaction strength $U = 100\Gamma$ plus the level splitting $\Delta E = 50\Gamma$ assumed. We consider a spin-polarized system, where each level is only occupied once. Other parameters used are $k_B T = 2\Gamma$, $\Gamma_L = \Gamma_R = \Gamma$ are the coupling strength of the dot levels to the left and right lead respectively. For convenience the units are all given in energy units normalized by the lead-dot coupling strength Γ.

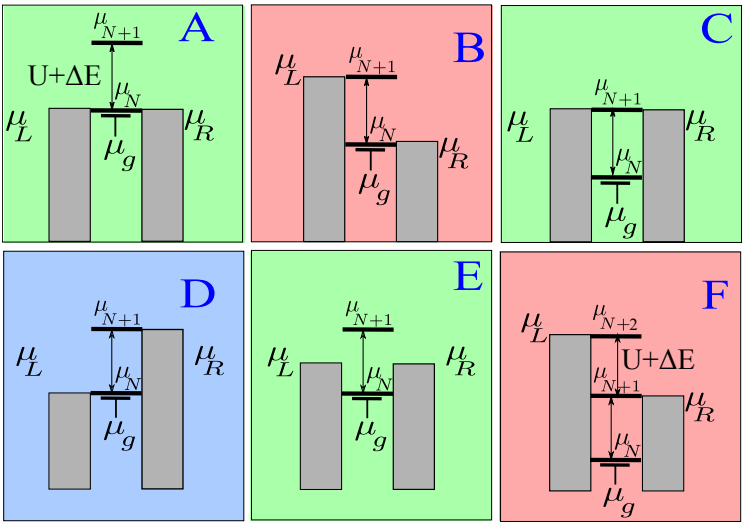

Figure 2.2: Schematic diagrams describing the transport situation for the different points marked in Fig. 2.1. The points A, E and C are zero (low) bias points, point D is negative bias and points B and F are positive bias points. The bias voltage is defined as $V_{bias} = (\mu_L - \mu_R)/e$. μ_N, μ_{N+1} and μ_{N+2} are the chemical potential of the dot containing N, $N+1$ and $N+2$ electrons respectively.

Once we discussed the basic principles of current spectroscopy through a single quantum dot, we can start discussing the transport calculations carried out in paper I. The main observable is the current through the serially coupled three quantum dots under a biasing condition as shown in Fig. 2.4. The methods used for calculating the current is based on the density matrix theory as discussed in Refs. [39–41].

In order to follow the discussions in the next sections, introducing the concept of a density matrix will be helpful at this stage.

2.1.1 Density Matrix and its Properties

Following Ref. [42] a density matrix (also called density operator) can be defined for a quantum system, that can be represented by a general time dependent wave function $|\psi(t)\rangle$ as,

$$\rho(t) = |\psi(t)\rangle\langle\psi(t)|. \tag{2.1}$$

For an arbitrary basis set $\{|i\rangle\}$ such that $|\psi(t)\rangle = \sum_i c_i(t)|i\rangle$, Eq. 2.1 becomes

$$\rho(t) = |\psi(t)\rangle\langle\psi(t)| = \sum_i \sum_j c_i(t)c_j^*(t)|i\rangle\langle j| = \sum_{ij} \rho_{ij}(t)|i\rangle\langle j|, \tag{2.2}$$

where $\rho_{ij}(t) = c_i(t)c_j^*(t)$ is the density matrix element. The system in question can be in a *pure* state, where it can be described by a single wave function (state vector). Otherwise it is said to be in a *mixed* state, in which case it is described by a mixture of different states $|\psi_i\rangle$ with their respective probabilities P_i. In such a case density matrix can be written as:

$$\rho(t) = \sum_i P_i|\psi_i(t)\rangle\langle\psi_i(t)|, \tag{2.3}$$

where P_i is the probability of the system to be in the state $|\psi_i(t)\rangle$ which is non-negative and normalized to unity:

$$P_i \geq 0, \tag{2.4}$$

$$\sum_i P_i = 1. \tag{2.5}$$

In the case of a pure state all $P_i = 0$ except one of them which is $P_i = 1$. The corresponding density matrix element for a system in a mixed state can be obtained from Eq. 2.3

$$\rho_{ij}(t) = \langle i|\rho(t)|j\rangle = \sum_i P_i\langle i|\psi_i(t)\rangle\langle\psi_i(t)|j\rangle. \tag{2.6}$$

Below a summary of important properties of the density matrix is given:

1. The density matrix is Hermitian, i.e.,

$$\rho_{ij}^{*}(t) = \rho_{ji}(t). \tag{2.7}$$

2. The diagonal elements of the density matrix cannot be negative since they represent probabilities of occupation of states. For a general case in a mixed state,

$$\rho_{ii}(t) = \sum_{i} P_i \langle i|\psi_i(t)\rangle\langle\psi_i(t)|i\rangle = \sum_{i} P_i |\langle i|\psi_i(t)\rangle|^2 \geq 0. \tag{2.8}$$

   These diagonal matrix elements are often called *populations*.

3. The off-diagonal elements of the density matrix $\rho_{ij}(t)$ with $i \neq j$ are generally complex. These off-diagonal matrix elements are often called *coherences* which describe superposition of states.

4. The trace of the density matrix is unity. This condition is called the normalization condition analogous to the normalization of the wave function. This is due to the fact that the trace is the sum of the diagonal elements which are occupation probabilities of the individual states.

$$Tr\rho(t) = 1. \tag{2.9}$$

5. The square of the trace of the density matrix satisfies

$$Tr\rho^2(t) \leq 1, \tag{2.10}$$

   where the equality is true for pure states while for mixed state $Tr\rho^2(t) < 1$. This quantity can be used as a measure for purity of a state.

6. The Schwartz inequality for the density matrix: *The magnitude of each off-diagonal element of the density matrix is smaller than or equal to the geometric mean of the corresponding diagonal elements*

   - For a pure state

$$\rho_{ii}\rho_{jj} = |\rho_{ij}|^2 \qquad \text{for all i,j.} \tag{2.11}$$

   - For a mixed state

$$\rho_{ii}\rho_{jj} \geq |\rho_{ij}|^2. \tag{2.12}$$

2.2 Quantum Master Equations

2.2.1 Model System and Many Particle Representation.

Most of the derivations in this chapter strictly follow previous works developed in our group [39–41, 43] for transport calculations through nanostructures. For transport calculations through nanostructures the first step towards the solution is to define the system Hamiltonian. In a typical transport calculation the total Hamiltonian can be separated into parts that describe the quantum system, the leads and the coupling between the lead and the system. For quantum dots and coupled quantum dots the energy level within the dot is assumed to be discrete. Depending on the size of the dots and type of the materials, the spacing between energy levels can vary. For metallic leads one usually assumes Fermi-Dirac distribution of electrons in the lead. The lead and the dot systems are coupled via a tunneling process. The general form for the total system-lead Hamiltonian is given by:

$$H_{\text{total}} = H_{\text{Dot}} + H_{\text{Lead}} + H_{\text{Dot-Leads}}, \tag{2.13}$$

H_{Dot} is the dot Hamiltonian in the single particle basis, which can be written as

$$H_{\text{Dot}} = \sum_{i\sigma} E_i d^{\dagger}_{i\sigma} d_{i\sigma}, \tag{2.14}$$

where the summation i runs through all levels of the quantum dot. $d^{\dagger}_i$ and d_i are the creation and annihilation operator in the dot level i with spin σ respectively. For coupled quantum dot system, an additional term to the Hamiltonian in Eq. 2.14 is needed to describe the coupling between the states in the different dots and the single particle energies in each dot. This modifies Eq. 2.14 as

$$H_{\text{Dot}} = \sum_{i\sigma} E_i d^{\dagger}_{i\sigma} d_{i\sigma} + \sum_{ij\sigma} \Omega_{ij} d^{\dagger}_{i\sigma} d_{j\sigma}, \tag{2.15}$$

where Ω_{ij} is the coupling matrix element between the ith level in one dot and the jth level in the neighboring with spin σ. In the case where more than one electron is considered, ee interactions become relevant. In this case an additional term for the dot Hamiltonian in Eq. 2.15 is needed.

$$H_{\text{Dot}} = \sum_{i\sigma} E_i d^{\dagger}_{i\sigma} d_{i\sigma} + \sum_{ij\sigma} \Omega_{ij} d^{\dagger}_{i\sigma} d_{j\sigma} + \frac{1}{2} \sum_{ijkl\sigma\sigma'} V_{mnkl} d^{\dagger}_{i\sigma} d^{\dagger}_{j\sigma'} d_{k\sigma'} d_{l\sigma}, \tag{2.16}$$

where V_{mnkl} is the Coulomb matrix element. In most cases, for electrons in different quantum dots that have significant spatial separation, the ee contribution to the dot Hamiltonian is significantly small. Often for quantum dots that are not immediate neighbors, both the coupling between the levels in the dots, Ω, and the Coulomb matrix elements are zero.

Details on the calculation of the Coulomb matrix element V_{mnkl} for a specific model system will be given in Sec. 2.5. The Hamiltonian describing the metallic lead ℓ is given as:

$$H_{\mathrm{Lead}} = \sum_{k\sigma\ell} E_{k\sigma\ell} c^{\dagger}_{k\sigma\ell} c_{k\sigma\ell}, \tag{2.17}$$

where $E_{k\sigma\ell}$ in Eq. 2.17 is the energy of an electron in the lead ℓ with spin σ and wave vector k. $c^{\dagger}_{k\sigma\ell}$ and $c_{k\sigma\ell}$ are fermion creation and annihilation operators for the lead states respectively. The remaining term from Eq. 2.13 is the lead-dot coupling Hamiltonian $H_{\mathrm{Dot-Lead}}$ which is a tunneling process of creating an electron in the dot state by destroying one in the lead state and vice-versa:

$$H_{\mathrm{Dot-Lead}} = \sum_{i,k\sigma\ell} \left(t_i(k\sigma\ell) d^{\dagger}_{i\sigma} c_{k\sigma\ell} + t^{*}_i(k\sigma\ell) c^{\dagger}_{k\sigma\ell} d_{i\sigma} \right), \tag{2.18}$$

$t_i(k\sigma\ell)$ in Eq. 2.18 is the tunnel matrix element between the level in the dot and the lead state. The evaluation of the tunneling matrix element can be done via different approaches that depend on the problem at hand. In paper I we assumed energy independent tunnel couplings $t_i(k\sigma\ell) = t_i(\sigma\ell)$.

A many particle state $|a\rangle$ is obtained by exact diagonalisation of the dot Hamiltonian H_{Dot}. In this many particle basis, the dot Hamiltonian is diagonal.

$$H_{\mathrm{Dot}}|a\rangle = E_a|a\rangle. \tag{2.19}$$

By using the second quantization representation [44] the general form of the many particle state is given by

$$|a\rangle = \sum_{i_1, i_2 \cdots i_{N_a}} a(i_1, i_2 \cdots i_{N_a}) d^{\dagger}_{i_1} d^{\dagger}_{i_2} \cdots d^{\dagger}_{i_{N_a}} |0\rangle = \sum_{i_1, i_2 \cdots i_{N_a}} a(i_1, i_2 \cdots i_{N_a}) |i_1 i_2 \cdots i_{N_a}\rangle, \tag{2.20}$$

where $d^{\dagger}_{i_1} d^{\dagger}_{i_2} \cdots d^{\dagger}_{i_{N_a}}$ create particles in the levels $i_1, i_2, \cdots, i_{N_a}$ respectively. Here the ordering of the indices $i_1 \leq i_2 \leq \cdots \leq i_{N_a}$ is assumed to avoid double counting. One is often interested in the problem of coupling between the lead and the many particle states of the system. Here the tunneling Hamiltonian can be reformulated in the many-particle basis by inserting the complete set $\sum_a |a\rangle\langle a|$, $\sum_b |b\rangle\langle b|$ in to Eq. 2.18

$$H_{\mathrm{Dot-Lead}} = \sum_{k\sigma\ell,a,b} \left(|b\rangle \underbrace{\sum_i t_i(k\sigma\ell) \langle b| d^{\dagger}_{i\sigma} |a\rangle}_{=T_{ba}(k\sigma\ell)} \langle a| c_{k\sigma\ell} + c^{\dagger}_{k\sigma\ell} |a\rangle \underbrace{\sum_n t^{*}_i(k\sigma\ell) \langle a| d_{i\sigma} |b\rangle}_{=T^{*}_{ba}(k\sigma\ell)} \langle b| \right), \tag{2.21}$$

which can be further simplified as

$$H_{\mathrm{Dot-Lead}} = \sum_{k\sigma\ell,a,b} T_{ba}(k\sigma\ell)c_{k\sigma\ell}|b\rangle\langle a| + T^{*}_{ba}(k\sigma\ell)c^{\dagger}_{k\sigma\ell}|a\rangle\langle b|. \tag{2.22}$$

In Eq. 2.22 the first term on the right side of the equal sign describes the transition in the dot from state $|a\rangle \rightarrow |b\rangle$ when an electron tunnels in to the dot from the lead ℓ with spin σ and wave vector k. The second term is its Hermitian conjugate. It describes tunneling out of the dot system $|a\rangle \rightarrow |b\rangle$ and creating an electron in the lead ℓ with spin σ and wave vector k. The convention for the many particle eigenstates $|a\rangle, |b\rangle, |c\rangle \cdots$ is that the number of particle increases by 1 in increasing order of the *letters*. i.e, $N_c = N_b + 1, N_b = N_a + 1$ etc. Therefore the first term in the right part of Eq. 2.22 describes an increase in the particle number of the dot system by 1 due to the tunneling from the lead. On the other hand, the complex conjugate term describes a tunneling out of the dot which causes a reduction of the number of particles in the dot by 1.

Following the notation described in Ref. [40], for the coupled system (in our case the dots and the leads) a general state vector can be written as a product state $|ag\rangle = |a\rangle \otimes |g\rangle$ with $|a\rangle$ being the many-particle states of the central region and $|g\rangle = |\{N_{k\sigma\ell}\}\rangle$ being the state of the leads, where $N_{k\sigma\ell} \in \{0, 1\}$.

We introduce the following notation, which is consistent with the anti-commutation relations.

- $c^{\dagger}_{k\sigma\ell}|g\rangle \equiv \delta_{N_{k\sigma\ell},0}|g + k\sigma\ell\rangle$ and $c_{k\sigma\ell}|g\rangle \equiv \delta_{N_{k\sigma\ell},1}|g - k\sigma\ell\rangle$.
- $|gk\sigma\ell\rangle \equiv c^{\dagger}_{k\sigma\ell}c_{k\sigma\ell}|g\rangle$ and $|g\overline{k\sigma\ell}\rangle \equiv c_{k\sigma\ell}c^{\dagger}_{k\sigma\ell}|g\rangle$. I.e., $|g\overline{k\sigma\ell}\rangle = \delta_{N_{k\sigma\ell},1}|g\rangle$.
- Taking into account the anti-commutation rule of the operators, the order of indices is opposite to the order of the operators. For example,
  $|g + k\sigma\ell - k'\sigma'\ell'\rangle = c_{k'\sigma'\ell'}c^{\dagger}_{k\sigma\ell}|g\rangle = -c^{\dagger}_{k\sigma\ell}c_{k'\sigma'\ell'}|g\rangle = -|g - k'\sigma'\ell' + k\sigma\ell\rangle$.

As the many-particle state $|a\rangle$ implies the presence of N_a creation operators, see Eq.(2.20), one obtains

$$c_{k\sigma\ell}|ag\rangle = c_{k\sigma\ell}|a\rangle \otimes |g\rangle = (-1)^{N_a}|a\rangle \otimes c_{k\sigma\ell}|g\rangle = (-1)^{N_a}|ag - k\sigma\ell\rangle,$$

and similarly $c^{\dagger}_{k\sigma\ell}|ag\rangle = (-1)^{N_a}|ag + k\sigma\ell\rangle$.
The elements of the density matrix ρ in a general way can be written as,

$$\rho^{[n]}_{ag;bg'} = \langle ag|\hat{\rho}|bg'\rangle, \tag{2.23}$$

where the label n indicates the total number of electron-hole excitations (*ehx*) involved in transforming g to g'. The hole in this case is the absence of an electron. It participates in transport with opposite charge to the electron. In the calculation we restrict ourselves to a maximum of $n = 1$.

2.3 Equation of Motion for the Density Matrix.

The time evolution of the density operator is given by the von-Neumann equation:

$$i\hbar\frac{d}{dt}\rho = [H, \rho]. \tag{2.24}$$

From Eq. 2.24 the equations of motion for the $0-ehx$ and $1-ehx$ matrix elements are

$$\begin{aligned} i\hbar\frac{d}{dt}\rho^{[0]}_{bg;b'g} &= (E_b - E_{b'})\rho^{[0]}_{bg;b'g} + \sum_{a,k\sigma\ell}(-1)^{N_a}T_{ba}(k)\rho^{[1]}_{ag+k;b'g} \\ &+ \sum_{c,k\sigma\ell}(-1)^{N_b}T^*_{cb}(k)\rho^{[1]}_{cg-k;b'g} - \sum_{c,k\sigma\ell}(-1)^{N_b}T_{cb'}(k')\rho^{[1]}_{bg';cg-k} \\ &- \sum_{a,k\sigma\ell}(-1)^{N_a}\rho^{[1]}_{bg;ag+k}T^*_{b'a}(k), \end{aligned} \tag{2.25}$$

and

$$\begin{aligned} i\hbar\frac{d}{dt}\rho^{[1]}_{cg-k\sigma\ell;bg} &= (E_c - E_b - E_k)\rho^{[1]}_{cg-k;bg} + \sum_{b'}(-1)^{N_b}T_{cb'}(k)\delta_{N_{k,1}}\rho^{[0]}_{b'g;bg} \\ &- \sum_{c'}(-1)^{N_b}\rho^{[0]}_{cg-k;c'g-k}T^*_{c'b}(k) + \sum_{k'\sigma'\ell'}\Big[\sum_{b'}(-1)^{N_b}T_{cb'}(k')\rho^{[2]}_{b'g-k+k';bg} \\ &+ \sum_{d}(-1)^{N_c}T^*_{dc}(k')\rho^{[2]}_{dg-k-k';bg} - \sum_{c'}(-1)^{N_b}\rho^{[2]}_{cg-k;c'g-k'}T_{c'b}(k') \\ &- \sum_{a}(-1)^{N_a}\rho^{[2]}_{cg-k;ag+k'}T^*_{ba}(k')\Big]. \end{aligned} \tag{2.26}$$

For most physical quantities, one is interested in the processes involving the dot states. As the number of degrees of freedom for the lead states (described by the Fermi-Dirac distribution) is much larger than the degrees of freedom for the dot states, the occupation

of the lead states is not affected by the coupling to the dots. Hence one can trace out all the lead states g to obtain a reduced density matrix,

$$\Phi^{[0]}_{b'b} = \sum_{g} \rho^{[0]}_{b'g;bg} \tag{2.27}$$

We also introduce the following current amplitudes neglecting excitations with $n \geq 2$

$$\Phi^{[1]}_{ba}(k\sigma\ell) = (-1)^{N_a} \sum_{g} \rho^{[1]}_{bg-k;ag}. \tag{2.28}$$

Using the Markov approximation for $\Phi^{[1]}_{ba}(k\sigma\ell)$ and equilibrium distribution in the leads we obtain the first order von-Neumann (1vN) equation, which we used in paper I. The change in occupation of the state k with spin σ and in lead ℓ can be expressed in terms of $\Phi^{[1]}_{ba}(k\sigma\ell)$ as follows

$$\begin{aligned}
\frac{d}{dt} n_{k\sigma\ell} &= \frac{d}{dt}\langle c^{\dagger}_{k} c_{k}\rangle = \frac{i}{\hbar}\sum_{gb}\langle gb|[\hat{H}, c^{\dagger}_{k}c_{k}]\hat{\rho}|gb\rangle \\
&= \frac{i}{\hbar}\left(\sum_{abg'}(-1)^{N_a} T_{ba}(k)\rho^{[1]}_{ag'+k;bg'} - \sum_{bcg}(-1)^{N_b} T^{*}_{cb}(k)\rho^{[1]}_{cg-k;bg}\right) \\
&= \frac{i}{\hbar}\sum_{gbc}\left((-1)^{N_b} T_{cb}(k)\rho^{[1]}_{bg;cg-k} - (-1)^{N_b} T^{*}_{cb}(k)\rho^{[1]}_{cg-k;bg}\right) \\
&= \frac{2}{\hbar}\sum_{cb}\Im\{T^{*}_{cb}(k)\Phi^{[1]}_{cb}(k)\}.
\end{aligned} \tag{2.29}$$

The running indices a, b, g' were replaced by b, c, g in the third line in the above equation and $|g\rangle = c^{\dagger}_{k}|g'\rangle$ were taken.
From Eq.(2.29), it is easy to see that the elements $\Phi^{[1]}_{cb}(k)$ describe current amplitudes associated with the single-particle transitions.

The particle current J_ℓ from the lead ℓ into the structure is given by

$$J_\ell = -\sum_{k\sigma(\ell)} \frac{d}{dt} n_{k\sigma\ell} = -\frac{2}{\hbar}\sum_{k\sigma(\ell)cb}\Im\{T^{*}_{cb}(k)\Phi^{[1]}_{cb}(k)\}, \tag{2.30}$$

which is represented by the particle losses in the respective lead due to the current amplitudes. $\Im$ in Eq. 2.30 is used to indicate that the the imaginary part of the quantity in the bracket is considered.

2.4 Pauli Master Equation

Sometimes the contribution from the off-diagonal elements of the density matrix to transport can be negligible. In such cases the calculation of observables such as current based on the Pauli master equation approach can provide similar result to those calculated via the first order von-Neumann approach. Numerically it is much simpler to calculate than other similar approaches as the number of non-zero matrix elements are reduced significantly. The Pauli master equation is a set of differential equations for occupation probabilities of the many particle states $\{|a\rangle, |b\rangle \cdots\}$ given. Following Refs. [41, 43]:

$$\begin{aligned}\frac{dP_b}{dt} = &\sum_{a\ell} P_a \underbrace{\Gamma_{a\to b,\ell} f_\ell(E_b - E_a)}_{\gamma^{\text{in}}_{a\to b}(\ell)} + \sum_{c\ell} P_c \underbrace{\Gamma_{c\to b,\ell}(1 - f_\ell(E_c - E_b))}_{\gamma^{\text{out}}_{c\to b}(\ell)} \\ &- P_b \sum_{a\ell} \underbrace{\Gamma_{b\to a,\ell}(1 - f_\ell(E_b - E_a))}_{\gamma^{\text{out}}_{b\to a}(\ell)} - P_b \sum_{c\ell} \underbrace{\Gamma_{b\to c,\ell} f_\ell(E_c - E_b)}_{\gamma^{\text{in}}_{b\to c}(\ell)},\end{aligned} \tag{2.31}$$

where the indices $\{a, c\}$ run over the many particle states $\{|a\rangle, |b\rangle \cdots\}$, $\Gamma_{a\to b,\ell}$ is the transition rate to tunnel from lead ℓ to the dot which causes the dot state to change from $|a\rangle$ to $|b\rangle$, which can be calculated by Fermi's golden rule:

$$\Gamma_{a\to b,\ell} = \frac{2\pi}{\hbar} \sum_{k\sigma} |T_{ba}(k\sigma\ell)|^2 \delta(E_a - E_b + E_k), \tag{2.32}$$

P_a, P_b and P_c are probabilities of finding the system in a state $|a\rangle$, $|b\rangle$ and $|c\rangle$ respectively, which are the diagonal elements of the reduced density matrix with different particle numbers. $f_\ell(E_b - E_a)$ is the Fermi-Dirac distribution function given by

$$f_{k\sigma\ell}(E) = \frac{1}{\exp(\frac{E_{k\sigma\ell} - \mu_\ell}{k_B T} + 1)}, \tag{2.33}$$

where μ_ℓ is the chemical potential of the lead ℓ, k_B is the Boltzmann constant, and T is the system temperature.

The role of each term on the right hand side of Eq. 2.31 will be discussed below. The first term describes a contribution to occupy state $|b\rangle$ by tunneling from the lead state to the dot which were initially in state $|a\rangle$. The rate of this process is given by the generalized rate $\gamma^{\text{in}}_{a\to b}(\ell)$. The second term describes a contribution to occupy state $|b\rangle$ by tunneling out from the dot which was initially in state $|c\rangle$ to the lead state. This happens with the corresponding generalized rate $\gamma^{\text{out}}_{c\to b}(\ell)$. The third term describes a reduction in occupation of state $|b\rangle$ by tunneling out to the lead from the dot state $|b\rangle$. This happens with

a generalized rate $\gamma^{\text{out}}_{b\to a}(\ell)$. Finally the fourth term described a reduction of occupation for state $|b\rangle$ as a result of tunneling in from the lead to the dot which was initially in state $|b\rangle$. The corresponding generalized rate for this process is $\gamma^{\text{in}}_{b\to c}(\ell)$. All the above processes conserve energy.

In this approach the particle current from the lead ℓ to the dot is given by:

$$J_\ell = \sum_{ab}[P_a\Gamma_{a\to b,\ell}f_\ell(E_b - E_a) - P_b\Gamma_{b\to a,\ell}(1 - f_\ell(E_b - E_a))], \tag{2.34}$$

This approach is valid for weak tunnel coupling (Γ) compared other energies of the system such as temperature (k_BT) and level spacing (ΔE).

$$\Gamma \ll k_BT, \Delta E \tag{2.35}$$

The current through a single quantum dot shown in Fig. 2.1 was calculated based on Eq. 2.34.

2.5 Coulomb Matrix Element Calculations for Triple Quantum Dots

In paper I, the importance of Coulomb ee scattering for enabling transport through serial triple quantum dot is discussed. In this section an outline of the calculations for the Coulomb matrix elements will be given. For the purpose of obtaining non-degenerate levels, the individual quantum dots are assumed to have a cuboid geometry as shown in Fig 2.3. Experimentally it is common to grow nanowires which are cylindrical for the dimensions used in paper I and hexagonal for larger diameters as they form facets when the thickness increases [45]. Approximation by an elongated cuboid can still capture the major features. The wavefunctions for the levels shown in the model can be obtained by solving the Schrödinger equation assuming a particle confined in a box model for each dot:

$$|\psi(n_x, n_y, n_z, s)\rangle = \sqrt{\frac{8}{L_xL_yL_z}}\sin(\frac{n_x\pi x}{L_x})\sin(\frac{n_y\pi y}{L_y})\sin(\frac{n_z\pi z}{L_z})\chi(s), \tag{2.36}$$

where n_x, n_y, n_z denote the quantum numbers in the x,y and z directions respectively and $\chi(s)$ is the spin wave function. L_x, L_y, L_z determine the dimension of the box with $L_z > L_y > L_x$ which are adjusted to obtain appropriate energies.

For spinfull simulations a total of 10 states with 4 in the first and second dot and two in the third dot are considered see Fig. 2.4. In the case of spinless simulations only 5 states

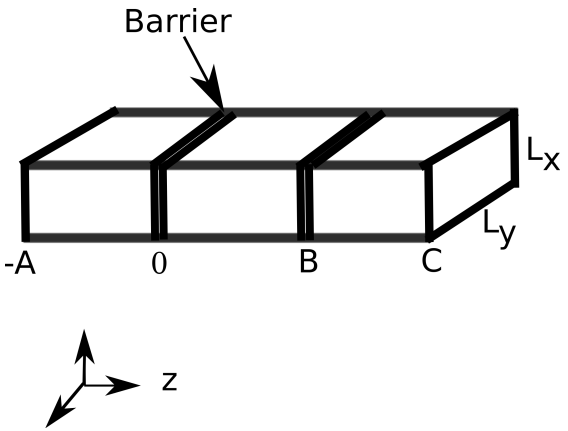

Figure 2.3: Schematics of cuboid triple quantum dot

with states 1 and 2 and in the first dot states 3 and 4 are in the second dot and state 5 in the third dot are considered.

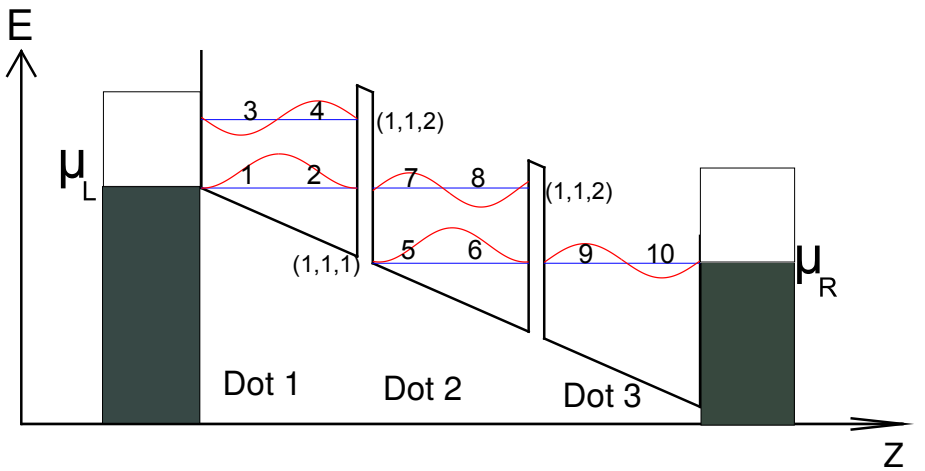

Figure 2.4: Schematics of serially coupled triple quantum dots attached with left and right leads. Spin degenerate energy levels are labeled from 1 to 10. Only the levels in the first dot and the third dot are coupled to the leads. In addition, the (n_x, n_y, n_z) is indicated for some of the levels.

The Coulomb matrix element for a given wave function $\Psi(\mathbf{r}, s)$ can be evaluated as:

$$V_{n_1 n_2; m_1 m_2} = \langle \chi_{n_1} | \chi_{m_2} \rangle \langle \chi_{n_2} | \chi_{m_1} \rangle \int \int d^3\mathbf{r} d^3\mathbf{r}' \phi^*_{n_1}(\mathbf{r}) \phi^*_{n_2}(\mathbf{r}') V(\mathbf{r} - \mathbf{r}') \phi_{m_1}(\mathbf{r}') \phi_{m_2}(\mathbf{r}), \tag{2.37}$$

which conserves spin for the pairs (n_1, m_2) and (n_2, m_1). With the (screened) Coulomb potential

$$V(\mathbf{r\text{-}r'}) = \frac{e^2 \mathrm{e}^{-\lambda|\mathbf{r}-\mathbf{r'}|}}{4\pi\epsilon_{\mathrm{host}}\epsilon_0|\mathbf{r}-\mathbf{r'}|}, \tag{2.38}$$

where ϵ_{host} is the dielectric constant of the host material, ϵ_0 is the permittivity of free space and λ is the screening length. Eq. 2.38 can be written as a Fourier transform which will simplify further calculations:

$$\begin{aligned} V(\mathbf{r\text{-}r'}) =& \frac{e^2}{\epsilon_{\mathrm{host}}\epsilon_0}\frac{1}{(2\pi)^3}\int d^3\mathbf{q}\frac{e^{i\mathbf{q}.(\mathbf{r}-\mathbf{r'})}}{(|\mathbf{q}|^2+\lambda^2)} \\ =& \frac{e^2}{\epsilon_{\mathrm{host}}\epsilon_0}\frac{1}{V_N}\sum_{\mathbf{q}}\frac{e^{i\mathbf{q}.(\mathbf{r}-\mathbf{r'})}}{(|\mathbf{q}|^2+\lambda^2)}. \end{aligned} \tag{2.39}$$

Putting Eq. 2.39 into Eq.2.37,

$$V_{n_1n_2;m_1m_2} = \frac{e^2}{\epsilon_{\mathrm{host}}\epsilon_0}\frac{1}{V_N}\sum_{\mathbf{q}}\frac{1}{(|\mathbf{q}|^2+\lambda^2)}\underbrace{\int d^3\mathbf{r}\phi^*_{n_1}(\mathbf{r})e^{i\mathbf{q}.\mathbf{r}}\phi_{m_2}(\mathbf{r})}_{A(q)_{n_1,m_2}}\underbrace{\int d^3\mathbf{r'}\phi^*_{n_2}(\mathbf{r'})e^{-i\mathbf{q}.\mathbf{r'}}\phi_{m_1}(\mathbf{r'})}_{A^*(q)_{m_1,n_2}}. \tag{2.40}$$

The A integrals can be solved separately for all the possible pairs which correspond to transitions between states.

$$A(q)_{n_1,m_2} = \int d^3\mathbf{r}\phi^*_{n_1}(\mathbf{r})e^{i\mathbf{q}.\mathbf{r}}\phi_{m_2}(\mathbf{r}). \tag{2.41}$$

The possible set of (n_1, m_2) pairs that are important for the processes considered are summarized in table 2.1.

All the Coulomb matrix elements in table 2.1 were evaluated numerically from Eq. 2.40 by using wave functions in cuboids with $L_x = 33\mathrm{nm}$, $L_y = 35\mathrm{nm}$ and $L_z = 40\mathrm{nm}$ for each dots. These results were used for comparison with the estimated matrix elements used in the paper. In some of the cases, the estimates are based on dipole matrix elements obtained from a tight-binding superlattice model [46]. The important steps will be sketched below. Here the two major categories are the *Intradot* and *Interdot* interactions based on if the interaction is localized only within the same dot or not.

Table 2.1: Important matrix elements considered in the calculation and their explanations.

V_{1221}	Intradot interaction -direct (Within the same dot between degenerate electrons with different spin).
V_{4334}	Intradot interaction -direct (Within the same dot between degenerate electrons with different spin).
V_{1331}	Intradot interaction -direct (Within the same dot between electrons in different levels with same spin).
V_{2442}	Intradot interaction -direct (Within the same dot between electrons in different levels with same spin).
V_{1313}	Intradot interaction -exchange (Within the same dot between electrons in different levels with same spin).
V_{1423}	Intradot interaction -scattering (Within the same dot between electrons in different levels with different spin).
V_{1243}	Intradot interaction -scattering (Within the same dot between electrons in different levels with different spin).
V_{1551}	Interdot interaction -direct (Within different dots between electrons in different levels with same spin).
V_{1753}	Interdot interaction -scattering (Within different dots between electrons in different levels with same spin).
V_{1771}	Interdot interaction -direct (Within different dots between electrons in different levels with same spin).
V_{1553}	Interdot interaction (Within different dots between electrons in different levels with same spin).

Intradot Interaction

In this case all the participating levels $n_1 n_2 m_1 m_2$ arise from the same dot. By employing the normalization condition for the wave functions one obtains for the direct elements an estimate:

$$V_{n_1 n_2 n_2 n_1} \approx \frac{e^2}{4\pi\varepsilon_r\varepsilon_0\sigma} = U, \tag{2.42}$$

where $\sigma = \sqrt{\langle(\mathbf{r} - \langle\mathbf{r}\rangle)^2\rangle}$ is the standard deviation for the spatial extension of the dot wave functions. A second set of intradot interaction matrix elements are of the type $V_{n_1 n_2 n_1 n_2}$, that act as exchange terms in the case of equal spins and as scattering terms in the case of different spins. A typical value in this case is:

$$V_{n_1 n_2 n_1 n_2} \approx U_{ex} \quad \text{with } U_{ex} = \frac{U}{5}, \tag{2.43}$$

which is confirmed by our numerical integration (see Table 2.2)

Interdot Interaction

For interdot interaction not all the levels $n_1 n_2 m_1 m_2$ are from the same dot. In the same way as Eq. (2.42) the direct interaction between two states in the neighboring dot can be

Table 2.2: Comparison for selected Coulomb matrix elements calculated via a numerical integration Eq. 2.40 and approximation using Eqs. 2.42- 2.47. For the estimation, the following parameters are used. $\epsilon_{\mathrm{r,InAs}} = 15$ (see Ref. [48]), $d = 43$ nm, $\sigma = 11$ nm and the dipole matrix element $|S_{21} = 8nm|$. Regarding the spins, the convention that odd numbered levels are spin up and even numbered levels are spin down is used.

Matrix Element	Numerical evaluation	Estimate based on Eqs. 2.42- 2.47
V_{1221}	7.5 meV	$U = 8.6$ meV
V_{1331}	6.6 meV	$U = 8.6$ meV
V_{2442}	6.6 meV	$U = 8.6$ meV
V_{1313}	1.7 meV	$U_{\mathrm{ex}} = 1.7$ meV
V_{1551}	2.0 meV	$U_{\mathrm{n}} = 2.2$ meV
V_{1423}	1.7 meV	$U_{\mathrm{ex}} = 1.7$ meV
V_{1243}	1.7 meV	$U_{\mathrm{ex}} = 1.7$ meV
V_{1753}	-0.16 meV	$U_{\mathrm{sc}} = -0.15$ meV
V_{1771}	2.1 meV	$U_{\mathrm{n}} = 2.2$ meV
V_{1553}	0.4 meV	$U_{\mathrm{dc}} = 0.4$ meV

written as:

$$V_{n_1 n_2 n_2 n_1} \approx \frac{e^2}{4\pi\varepsilon_r\varepsilon_0 d} = U_n, \tag{2.44}$$

where d is an approximate distance between the centers of the dots. In addition to the direct terms, the dipole-charge U_{dc} and dipole-dipole scattering U_{sc} can be defined as:

$$V_{lnml} \approx \frac{e^2}{4\pi\varepsilon_r\varepsilon_0} \frac{\mathbf{s}_{nm} \cdot (\mathbf{R}_i - \mathbf{R}_j)}{d^3} = \pm U_{dc}, \tag{2.45}$$

$$V_{mnkl} \approx \frac{-e^2}{4\pi\varepsilon_r\varepsilon_0} \frac{2\mathbf{s}_{ml} \cdot \mathbf{s}_{nk}}{d^3} = U_{sc}, \tag{2.46}$$

with the intradot dipole matrix element

$$\mathbf{s}_{nm} = \int \mathrm{d}^3\mathbf{r}\varphi_n^*(\mathbf{r})\mathbf{r}\varphi_m(\mathbf{r}), \tag{2.47}$$

where the Taylor expansion of $1/|\mathbf{r} - \mathbf{r}'|$ around the centers of the respective dots $\mathbf{R}_i, \mathbf{R}_j$, see Ref. [47] and $|\mathbf{R}_i - \mathbf{R}_j| = d$ for neighboring dots was used in Eq. 2.45 and Eq. 2.46 above.

A good agreement between the two sets of calculation was obtained as shown in Table 2.2 for few selected elements.

For serially coupled triple quantum dots with level configurations as shown in Fig. 2.4, one of the main findings from the paper is discussed as follows. In a biasing condition where the states $1/2$ are aligned with the chemical potential of the left dot μ_L and the states $9/10$ are aligned with the chemical potential of the right lead μ_R, no current is predicted by varying the levels in the middle dot by standard considerations of coherent transport. However, via scattering interaction a current flow is enabled. Considering similar spins for

example (only spin up electrons labeled by odd numbers) in the condition where levels 1 and 4 are occupied, an energy conserving scattering creates simultaneous transitions $1 \rightarrow 3$ and $7 \rightarrow 5$ (for $E_7 - E_5 = E_3 - E_1$) which will then tunnel to the right lead through state 9.

These calculations were the basis for paper I, which discusses furthermore the validity of the Pauli master equation. This was checked by comparing the agreement of the results obtained using the Pauli master equation with the results of the 1vN approach. Here the difference between the two approaches is that the Pauli master equation approach neglects coherences while 1vN takes into account the full density matrix elements of the reduced quantum dot system. By using the Pauli master equation one can, to large extent, reproduce qualitatively all the resonances correctly. In some regimes where the lead coupling is larger than the energy splitting, i.e., $\Gamma > \Delta E$, the current can be overestimated by this approach. This can happen due to the fact that it is the regime where coherences strongly reduce the current.

Chapter 3

Exciton Dynamics

In this chapter, an introduction to the concept of excitons and their properties will be given. Excitons and the study of their dynamics constitute a major part in this thesis. Following the introduction, methods used to calculate energy levels and the dipole matrix elements for PbS quantum dot, which is the model system in most of the calculations, will be discussed. The chapter will be concluded by describing the modeling of the light field, which is used for the simulations in paper II and paper III.

3.1 Excitons

In bulk systems, excitation of a semiconductor with a light field causes an electron to jump across the band gap to an available state in the conduction band leaving a "hole" behind in the valence band. The hole, treated as an effective particle, has an opposite charge to that of the negatively charged electron. As a result, the hole and the electron feel an attractive Coulomb force. In the limit where the electron and the hole wavefunctions do not spread over a large number of atoms, they form a bound state. These electrically neutral, bound electron-hole pairs are called *Excitons* [49–53]. Yakov Frenkel in 1931 was the first to formulate the exciton as a non-conductive electronic excitation. The so called Frenkel excitons [54, 55] are one of the two major divisions of excitons, where the electron and the hole are tightly bound to each other, allowing them to fit in the same lattice site. Frenkel excitons are sometimes called zero-radius excitons due to their small exciton Bohr radius, in analogy to the Bohr radius of a hydrogen atom. Frenkel excitons are a common type of excitons in several small dielectric molecular systems and biological materials. On the other hand, materials with large dielectric constant, such as ionic crystals and inorganic semiconductors, have a large exciton Bohr radius. Due to screening, the Coulomb binding energy of

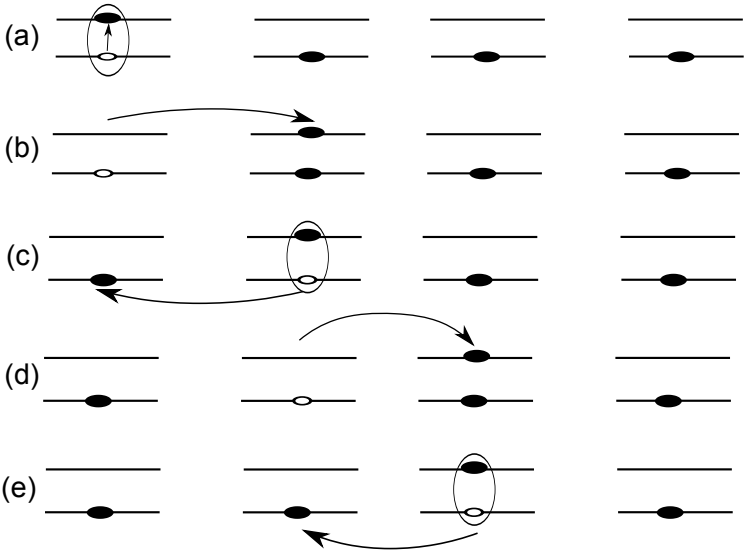

Figure 3.1: Exciton transfer in the Frenkel picture (inspired by Fig.2.2 from Ref. [51]). In a chain of two level systems an excitation is initiated by light in (a). The excited electron can now be transferred to the neighboring same energy level (b). A repulsive Coulomb force pushes the electron in the valence band to the neighboring atom (c). As a result the exciton which was located in the first site in (a) is moved to the second site in (c). the process repeats in (d) and (e) transferring the exciton by one more site

the electron and the hole in this case is not as large as compared to the Freknel excitons. These large radius weakly bound excitons are the second type of excitons called Wannier excitons [56]. Excitons play large role in energy transfer without transferring charge due to their electrically neutral nature. For Frenkel excitons an energy transfer across a chain of two level systems, which can represent coupled molecules, is schematically shown in Fig. 3.1. In a chain of two level systems, an excitation initiated in the beginning is transferred across the different sites.

3.2 Excitons in Nanostructures

Nanostructures have a characteristic discrete energy levels due to confinement. In quantum dots and molecules, an exciton can be formed by exciting the system using light field with an energy that matches the allowed transitions from the valence to the conduction band levels. As long as the transitions are allowed by selection rules the pulse energy can be varied to create spectrum of excitons cf. Fig. 3.2. In nanostructures, in addition to the type of the material, parameters such as the shape and the size of the structure greatly influence the properties of excitons [53]. Unlike the case in bulk materials, in nanostructures the exciton size is determined not only by the Coulomb interaction strength between the electron and

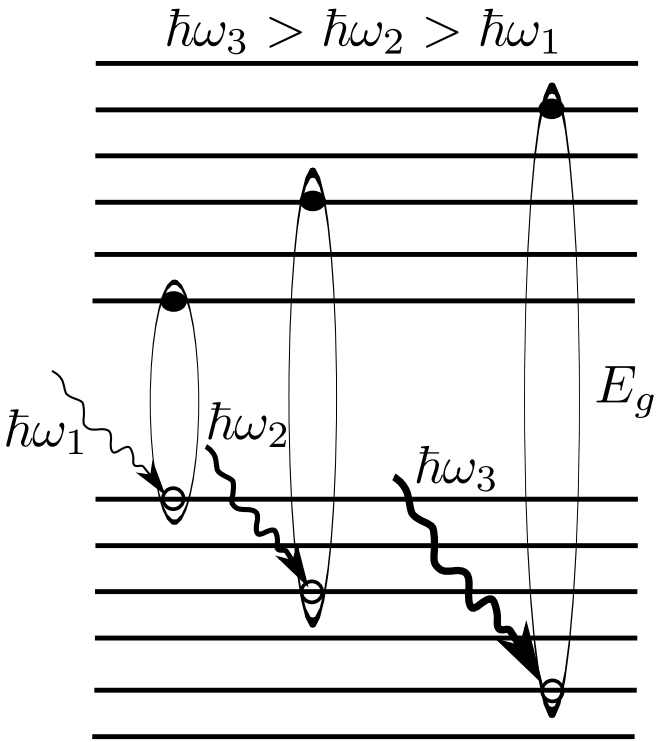

Figure 3.2: Excitation with different light energies can create spectrum of excitons in nanostructures.

the hole but also the physical size and shape of the system. The technological advancements in nanostructure fabrication provide freedom for controlling the growth parameter, which makes it possible to tune the sizes of excitons.

Due to their potential applications for optoelectronic and solar cell devices [57], lead sulfide (PbS) colloidal quantum dots and their size dependent optical properties have been investigated intensively. Colloidal quantum dots are different from the gate defined quantum dots in a nanowire, described in the previous chapter. They are chemically synthesized quantum dots which are suspended in solution [58]. In most of the simulations described in this thesis, parameters of a 4 nm PbS colloidal quantum dot is used. This is motivated by the availability of experimental data for such systems.

3.3 Calculation of Energy Levels and Dipole Matrix Elements

For evaluating the single particle energy spectra, a calculation based on the $\mathbf{K} \cdot \mathbf{P}$ method is used. The spectra depend on material parameters such as the size of the quantum dot and the effective mass for both the electron and the hole. Whenever needed, the parameters from Table 1 of Ref. [59] were used. In the following section a brief introduction to the calculation of single particle spectra based on the $\mathbf{K} \cdot \mathbf{P}$ approach is given.

3.3.1 The $\mathbf{K} \cdot \mathbf{P}$ Method

Several theoretical models are available for calculating band structures of bulk semiconductors and energy spectra for their nanostructure counterpars. The choice of methods generally depends on their capacity to include realistic effects to better predict band structures that agree well with experiments. One method which provides an accurate prediction of energy spectra for small PbS quantum dots is the $\mathbf{K} \cdot \mathbf{P}$ method [59, 60].

Fig. 3.3 shows a band structure for bulk PbS from Ref. [61]. It can be seen from the figure that PbS is a direct band gap material with the principal conduction band minimum and valence band maximum at the L point of the Brillouin zone. The conduction band minimum has L_6^- symmetry (with p_z-like spatial Bloch function where z is the $\langle 111 \rangle$-direction of the cubic lattice) and the valence band maximum has L_6^+ symmetry (with s-like spatial Bloch function).

The corresponding band edge Bloch functions are denoted as $|L_6^- \uparrow / \downarrow\rangle$, $|L_6^+ \uparrow / \downarrow\rangle$ for conduction and valence band for both spins, respectively.

The $\mathbf{K} \cdot \mathbf{P}$ model of Mitchel and Wallis [60] has been used extensively to describes the band structure near the band extrema (in this case the L point) for bulk PbS. This model takes into account coupling between the highest valence band and conduction bands and the lowest conduction band and valence bands in the second order perturbation approximation. In addition, the model considers the spin-orbit interaction and treats the four-band problem with two spin-degenerate states in the conduction band and two in the valence band exactly.

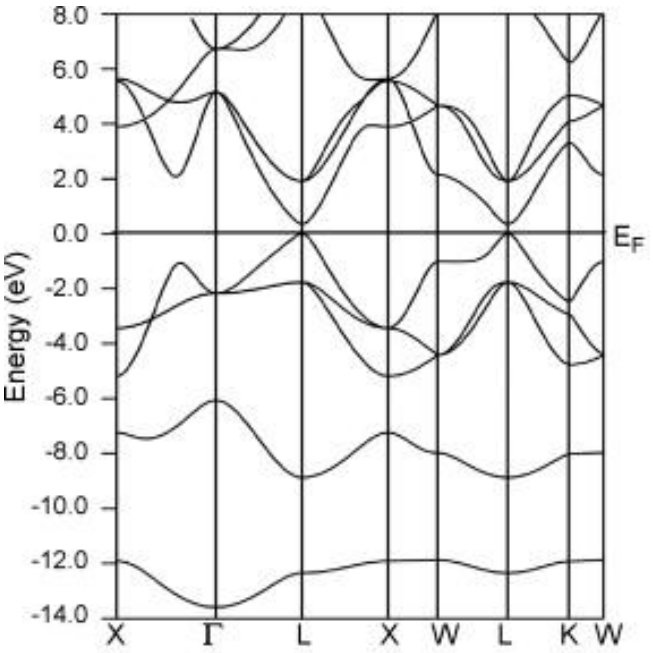

Figure 3.3: Band structure of bulk PbS along high symmetry directions of the first Brillouin zone. Indicated $\vec{k}$ points along the horizontal axis are $X(\frac{1}{2},\frac{1}{2},0)$, $\Gamma(0,0,0)$, $L(\frac{1}{2},\frac{1}{2},\frac{1}{2})$, $K(\frac{3}{4},\frac{3}{8},\frac{3}{8})$ and $W(\frac{3}{4},\frac{1}{2},\frac{1}{4})$. Picture reproduced with permission from Ref. [61], Copyright ©2007 Elsevier.

The Hamiltonian matrix is:

$$\hat{H} = \begin{pmatrix} |L_6^- \uparrow\rangle & |L_6^- \downarrow\rangle & |L_6^+ \uparrow\rangle & |L_6^+ \downarrow\rangle \\ \frac{E_g}{2} + \frac{\hbar^2 k_t^2}{2m_t^-} + \frac{\hbar^2 k_\ell^2}{2m_\ell^-} & 0 & \frac{\hbar}{m} P_\ell k_\ell & \frac{\hbar}{m} P_t k_- \\ 0 & \frac{E_g}{2} + \frac{\hbar^2 k_t^2}{2m_t^-} + \frac{\hbar^2 k_\ell^2}{2m_\ell^-} & \frac{\hbar}{m} P_t k_+ & -\frac{\hbar}{m} P_\ell k_\ell \\ \frac{\hbar}{m} P_\ell k_\ell & \frac{\hbar}{m} P_t k_- & -\frac{E_g}{2} - \frac{\hbar^2 k_t^2}{2m_t^+} - \frac{\hbar^2 k_\ell^2}{2m_\ell^+} & 0 \\ \frac{\hbar}{m} P_t k_+ & -\frac{\hbar}{m} P_\ell k_\ell & 0 & -\frac{E_g}{2} - \frac{\hbar^2 k_t^2}{2m_t^+} - \frac{\hbar^2 k_\ell^2}{2m_\ell^+} \end{pmatrix}. \tag{3.1}$$

The different terms in the above Hamiltonian matrix will be explained below.

$\vec{k}$ is the electron wave vector for the state considered relative to the band extrema:

$$\vec{k} = \vec{K} - 2\pi/a(1/2, 1/2, 1/2), \tag{3.2}$$

where $\vec{K}$ is the reduced wave vector of the state [62].
The longitudinal component of the wave vector k_ℓ is in the direction parallel to the $\langle 111 \rangle$-direction.
A Cartesian coordinate is defined in such a way that z is parallel to the $\langle 111 \rangle$-direction. This gives,

$$k_\ell = k_z. \tag{3.3}$$

Perpendicular to the k_ℓ is the transversal component k_t which itself has two components perpendicular to each other denoted here as k_x and k_y with $k_t^2 = k_x^2 + k_y^2$. In terms of k_x and k_y one obtains

$$\begin{aligned} k_- &= (k_x - ik_y), \\ k_+ &= (k_x + ik_y). \end{aligned} \tag{3.4}$$

E_g is the bulk band gap, m is the mass of a free electron. The diagonal elements include far-band contributions $\frac{\hbar^2 k_t^2}{2m_t^-} + \frac{\hbar^2 k_\ell^2}{2m_\ell^-}$ for the conduction band and $\frac{\hbar^2 k_t^2}{2m_t^+} + \frac{\hbar^2 k_\ell^2}{2m_\ell^+}$ for the valence band. The masses $m_{t/\ell}^+$ are the transversal and longitudinal components of the conduction band effective mass, respectively. Similarly, $m_{t/\ell}^-$ are the transversal and longitudinal components of the valence band effective mass, respectively. The momentum matrix elements $P_{t/\ell}$ are the transversal and longitudinal components taken between the extremal conduction and valence band states.

The detailed evaluation of the individual Hamiltonian matrix elements in Eq. 3.1 requires knowledge of the full wavefunctions. However, by looking at a general form of perturbation Hamiltonian which includes the spin-orbit coupling [60, 62]

$$\hat{H}' = \frac{\hbar}{m}\mathbf{K} \cdot \pi = \frac{\hbar}{m}\mathbf{K} \cdot (\mathbf{P} + \frac{\hbar}{4mc^2}\sigma \times \nabla V), \tag{3.5}$$

one can argue which part of the Hamiltonian couples which states. In Eq. 3.5 the first term on the right hand side couples states between the different bands with similar spins. This is the $\mathbf{K} \cdot \mathbf{P}$ perturbation without the spin orbit coupling. Since the conduction band states are p_z like and the valence band states are s like only the z (longitudinal) components become non-zero while evaluating elements such as $\langle L_6^- \uparrow | \frac{\hbar}{m}\mathbf{K} \cdot \mathbf{P} | L_6^+ \uparrow \rangle = \frac{\hbar}{m} P_\ell k_\ell$. The mixing between conduction band and valence band level with different spins are due to the spin-orbit coupling term proportional to $\mathbf{K} \cdot (\sigma \times \nabla V)$.

The Hamiltonian in Eq. 3.1 can be diagonalized to obtain a dispersion relation for the valence and conduction band

$$\left[\frac{E_g}{2}+\frac{\hbar^2k_t^2}{2m_t^-}+\frac{\hbar^2k_\ell^2}{2m_\ell^-}-E(\mathbf{k})\right]\left[-\frac{E_g}{2}-\frac{\hbar^2k_t^2}{2m_t^+}-\frac{\hbar^2k_\ell^2}{2m_\ell^+}-E(\mathbf{k})\right]=\frac{\hbar^2}{m^2}(P^2k_t^2+P^2k_\ell^2), \tag{3.6}$$

similar to Eq.2 in Ref. [59]. In the limit

$$m^\pm=m_t^\pm=m_\ell^\pm, \tag{3.7}$$

and

$$P=P_t=P_\ell \tag{3.8}$$

one obtains a k dependent expression where $k^2=k_t^2+k_\ell^2$

$$\begin{aligned}E_V(k)=&\frac{1}{2}\left[\left(\frac{\hbar^2k^2}{2m^-}-\frac{\hbar^2k^2}{2m^+}\right)-\sqrt{\left(E_g+\frac{\hbar^2k^2}{2m^-}+\frac{\hbar^2k^2}{2m^+}\right)^2+\frac{4\hbar^2k^2P^2}{m^2}}\right]\\ E_C(k)=&\frac{1}{2}\left[\left(\frac{\hbar^2k^2}{2m^-}-\frac{\hbar^2k^2}{2m^+}\right)+\sqrt{\left(E_g+\frac{\hbar^2k^2}{2m^-}+\frac{\hbar^2k^2}{2m^+}\right)^2+\frac{4\hbar^2k^2P^2}{m^2}}\right],\end{aligned} \tag{3.9}$$

for the valence and the conduction band energies, respectively.

However, the same limit specified in Eq. 3.11 and Eq. 3.10 is not always valid since the bands are not isotropic. Due to anisotropy the longitudinal and the transversal masses and momentum matrix elements can become different. Following Ref. [59], in this case we use the effective parameters

$$3P^2=2P_t^2+P_\ell^2, \tag{3.10}$$

and

$$3/m^\pm=2/m_t^\pm+1/m_\ell^\pm. \tag{3.11}$$

For a spherical quantum dot with radius a the simplest solution can be obtained by solving the Schrödinger equation for a particle of mass m in a spherical potential well. In this case one obtains the wavefunctions [63]

$$\Phi_{n,l,m}(r,\theta,\phi)=C\frac{j_l(k_{n,l}r)Y_l^m(\theta,\phi)}{r}, \tag{3.12}$$

where C is a normalization constant, $Y_l^m(\theta,\phi)$ are the spherical harmonics and $j_l(k_{n,l}r)$ is the lth order spherical Bessel function, and

$$k_{n,l} = \alpha_{n,l}/a, \tag{3.13}$$

where $\alpha_{n,l}$ is the nth zero of the Bessel function j_l. The corresponding energy spectrum is

$$E_{n,l} = \frac{\hbar^2 k_{n,l}^2}{2m} = \frac{\hbar^2 \alpha_{n,l}^2}{2ma^2}, \tag{3.14}$$

where $n(1,2,3,...)$ and $l(s,p,d,...)$ are the quantum numbers. Using the $\mathbf{K}\cdot\mathbf{P}$ method, one obtains energy spectrum for the states in the conduction and valence bands with a similar form as Eq. 3.9

$$\begin{aligned} E_{nl}^v &= \frac{1}{2}\left[\left(\frac{E_{nl}^0 m_e}{m^-} - \frac{E_{nl}^0 m_e}{m^+}\right) - \sqrt{\left(E_g + \frac{E_{nl}^0 m_e}{m^-} + \frac{E_{nl}^0 m_e}{m^+}\right)^2 + 4E_p E_{nl}^0}\right], \\ E_{nl}^c &= \frac{1}{2}\left[\left(\frac{E_{nl}^0 m_e}{m^-} - \frac{E_{nl}^0 m_e}{m^+}\right) + \sqrt{\left(E_g + \frac{E_{nl}^0 m_e}{m^-} + \frac{E_{nl}^0 m_e}{m^+}\right)^2 + 4E_p E_{nl}^0}\right], \end{aligned} \tag{3.15}$$

with

$$\begin{aligned} E_{nl}^0 &= \frac{\hbar^2 \alpha_{nl}^2}{2m_e a^2} \qquad \text{and} \\ E_p &= \frac{2P^2}{m_e}. \end{aligned} \tag{3.16}$$

An energy spectrum using the formulas in Eq. 3.15 is plotted in Fig 3.4. As an input for the formulas in Eq. 3.15, the material parameters for PbS quantum dots were adopted from Table 1 of article [59]. These values area displayed in Table 3.1, where Eq. 3.10 and Eq. 3.11 were used in evaluations.

Table 3.1: Parameters for the $\mathbf{K}\cdot\mathbf{P}$ Hamiltonian for PbS. Adopted from Table 1. of Ref. [59]

Parameters	values
E_g(T=300k)(eV)	0.41
m/m_t^-	1.9
m/m_ℓ^-	3.7
m/m^-	2.5
m/m_t^+	2.7
m/m_ℓ^+	3.7
m/m^+	3.0
$2P_t^2/m(eV)$(eV)	3.0
$2P_\ell^2/m(eV)$(eV)	1.6
$2P^2/m(eV)$(eV)	2.5

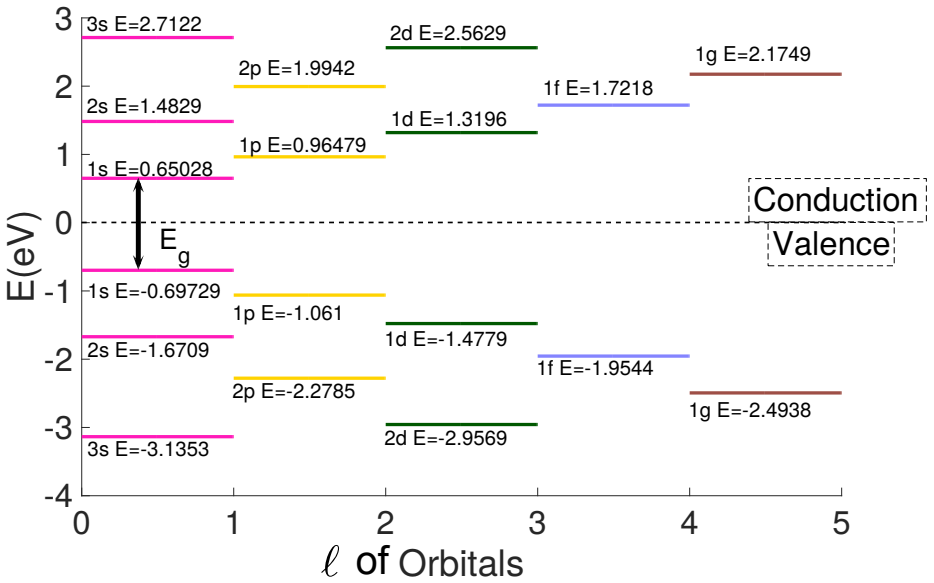

Figure 3.4: Single particle spectrum for the spherical quantum dot of diameter 4 nm calculated with the $\mathbf{K}\cdot\mathbf{P}$ method.

3.4 Dipole Matrix Elements

Once the energy levels are calculated, the determination of the transition matrix elements will be the next step. In chapter 10 of Ref. [64] a treatment for dipole matrix elements in quantum wells is given. Here we provide the important steps in evaluating the dipole transition matrix elements for quantum dots. The two major categories in this case are the *interband* and *intraband* matrix elements. Interband matrix elements involve transitions

between states that originate from the conduction and valence band while intraband matrix elements involve transitions between states originating from the same band. The methods used for calculating both types of the matrix elements will be discussed below.

3.4.1 Interband Matrix Elements

The dipole transition matrix element is given by the overlap integral [64]

$$\mu_{c,v} = \langle \Psi_c(\vec{r}) | \vec{e} \cdot \vec{p} | \Psi_v(\vec{r}) \rangle, \tag{3.17}$$

where $\vec{e}$ denotes the polarization of the light field and the total wave functions for the conduction and the valence band electrons are given by $|\Psi_c(\vec{r})\rangle$ and $|\Psi_v(\vec{r})\rangle$, respectively. At the band extrema, these wave functions are proportional to the product of an envelope function (χ_n) and the appropriate Bloch functions (u_{nk}), where $n \in \{c, v\}$ and k is the wave vector at the band extrema. However, near the band edge the Bloch function is weakly dependent on the wave vector k [64]. As a result one can assume k-independent Bloch functions $u_{nk} \approx u_n$,

$$|\Psi_c(\vec{r})\rangle \propto \chi_c(\vec{r}) u_c(\vec{r}), \tag{3.18}$$
$$|\Psi_v(\vec{r})\rangle \propto \chi_c(\vec{r}) u_v(\vec{r}). \tag{3.19}$$

Both the envelope and the Bloch functions are usually treated independently and normalized separately,

$$\int_V |\chi_n(\vec{r})|^2 d^3\vec{r} = 1, \tag{3.20}$$
$$\int_V |u_{nk}(\vec{r})|^2 d^3\vec{r} = 1, \tag{3.21}$$

both integrals above run over the volume of the sample Ω. The total wave functions can be set to have the form

$$|\Psi_n(\vec{r})\rangle = \sqrt{\Omega} \chi_n(\vec{r}) u_n(\vec{r}), \tag{3.22}$$

so that it obeys the same normalization as the components. The matrix element is then

$$\mu_{c,v} = \langle \Psi_c(\vec{r}) | \vec{e} \cdot \vec{p} | \Psi_v(\vec{r}) \rangle = \Omega \int_V \chi_c^*(\vec{r}) u_c^*(\vec{r}) (\vec{e} \cdot \vec{p}) \chi_v(\vec{r}) u_v(\vec{r}) d^3\vec{r}. \tag{3.23}$$

The above integral can be split into two parts as it contains functions which vary on two length scales. The Bloch functions $u_n(\vec{r})$ vary within each unit cells (they are the same

within each unit cell) while the envelope functions $\chi_n(\vec{r})$ vary on a much longer scale and almost constant within each unit cell. Thus the envelope functions can be pulled out of the integral as being constant within each cell and the integral can be considered as the sum over each unit cell j such that

$$\mu_{c,v} = \langle \Psi_c(\vec{r})|\vec{e}\cdot\vec{p}|\Psi_v(\vec{r})\rangle \approx \Omega \sum_{j}^{\text{cells}} \chi_c^*(\vec{r_j})\chi_v(\vec{r_j}) \int_{\text{cell j}} \underbrace{u_c^*(\vec{r})(\vec{e}\cdot\vec{p})u_v(\vec{r})d^3\vec{r}}_{(\Omega_{\text{cell}}/\Omega)\vec{e}\cdot\vec{p}_{cv}}, \tag{3.24}$$

with $\vec{p}_{cv}$ being the momentum matrix element between the Bloch wave functions at the band extrema. Thus

$$\mu_{c,v} = \langle \Psi_c(\vec{r})|\vec{e}\cdot\vec{p}|\Psi_v(\vec{r})\rangle \approx \vec{e}\cdot\vec{p}_{cv}\Omega_{\text{cell}} \sum_{j}^{\text{cells}} \chi_c^*(\vec{r_j})\chi_v(\vec{r_j}). \tag{3.25}$$

The sum over the cells can be turned to an integral over the sample as

$$\mu_{c,v} = \langle \Psi_c(\vec{r})|\vec{e}\cdot\vec{p}|\Psi_v(\vec{r})\rangle \approx \vec{e}\cdot\vec{p}_{cv} \int \chi_c^*(\vec{r})\chi_v(\vec{r})d^3\vec{r}. \tag{3.26}$$

From this expression we note that for transitions to be allowed, the matrix element in Eq. 3.26 must satisfy selection rules that

- The Bloch functions of the band edges must satisfy the dipole selection rules, i.e. two states with same parity can not be coupled via electric dipole Hamiltonian [20, 64].
- The spin component of the initial and final wavefunctions must be the same.

Numerical estimate for the allowed interband dipole matrix elements which are independent of the geometry for the dot can be obtained by considering the momentum matrix element for PbS from the article [59] with the convention that $P = P_\ell = P_t$.

Depending on the polarization of the light field, the dipole matrix element is a multiple of P. That is, if the light is polarized in the z direction $\vec{e} = \hat{e}_z$, then

$$\mu_{c,v} \approx \vec{e}\cdot\vec{p}_{cv} = P. \tag{3.27}$$

The above result is the value for the momentum matrix element. The corresponding position matrix element can be found by equating the dimensionless oscillator strength f in momentum and position space (see Ref. [64])

$$f_{cv} = \frac{2}{mE_g}|\langle \Psi_c(\vec{r})|\vec{e}\cdot\vec{p}|\Psi_v(\vec{r})\rangle|^2 = \frac{2mE_g}{\hbar^2}|\langle \Psi_c(\vec{r})|\vec{e}\cdot\vec{r}|\Psi_v(\vec{r})\rangle|^2, \tag{3.28}$$

such that the position matrix element becomes

$$|\langle\Psi_c(\vec{r})|\vec{e}\cdot\vec{r}|\Psi_v(\vec{r})\rangle|^2 = \frac{\hbar^2}{m^2E_g^2}|\langle\Psi_c(\vec{r})|\vec{e}\cdot\vec{p}|\Psi_v(\vec{r})\rangle|^2. \tag{3.29}$$

A typical value for the dipole matrix element by considering parameters from Table 3.1 is:

$$|\langle\Psi_c(\vec{r})|\vec{e}\cdot\vec{r}|\Psi_v(\vec{r})\rangle| = 0.7371 \text{ nm}. \tag{3.30}$$

3.4.2 Intraband Matrix Elements

If both initial and final states originate from the same band, the evaluation of the dipole matrix elements can be obtained by direct integration in position space. Here we considered the states either in the conduction or valence band that satisfy the dipole section rule and conserve spin.

For the polarization in the z direction $\vec{e} = (0, 0, 1)$, consider the initial and final states

$$\begin{aligned} |\Psi_i\rangle =& |\psi(n_x, n_y, n_z)\rangle \quad \text{and} \\ |\Psi_f\rangle =& |\psi(n_x, n_y, (n_z+1))\rangle, \end{aligned} \tag{3.31}$$

with both having same spin, and only the quantum number along the z direction is different,

For transitions within the conduction band for example, this can correspond to

$$\begin{aligned} |\Psi_i\rangle =& |\psi_c(1, 1, 1)\rangle \quad \text{and} \\ |\Psi_f\rangle =& |\psi_c(1, 1, 4)\rangle. \end{aligned} \tag{3.32}$$

For $L_x = 2.7925$ nm, $L_y = 3$ nm and $L_z = 4$ nm one obtains

$$\langle\Psi_f|\hat{z}|\Psi_i\rangle = -0.57640\text{Å}. \tag{3.33}$$

3.5 Pulse Parameters

In paper II and paper III, the excitation of a quantum system by a time dependent single pulse is considered. The time dependence in the interaction Hamiltonian originates from the electric field of the pulse

$$\hat{H}_I(t) = -\hat{\mu}\cdot\vec{E}(t). \tag{3.34}$$

where $\hat{\mu}$ is the electric dipole operator and $\vec{E}(t)$ is the time dependent electric field. In the calculation, $\vec{E(t)}$ is assumed to be a sinusoidal with a Gaussian envelope,

$$\vec{E}(t) = \vec{E}_0 \exp(-4ln2\big(\frac{t-t_0}{\tau}\big)^2) \cos(\omega_{\text{pulse}}(t-t_0)), \tag{3.35}$$

where in the above expression

- ω_{pulse} is the central frequency for the pulse, which can be tuned to have a value close to the resonance frequency between the different many-particle states. Typically this value is chosen to be in resonance to one of the main transitions.
- τ is the full width at half maximum (FWHM) of the pulse with a typical values ranging from picoseconds (ps) to femtoseconds (fs) for short pulses.
- $|E_0|$ is the electric field amplitude. A typical value can be obtained from an experiment. In the supplementary material of Ref. [65], a laser pulse with energy $E = 1.2$ mJ with a pulse duration of about $\tau = 150$ fs and a pump diameter at the focus of 0.7 mm is given. This gives an electric field peak value

  $$|E_0| = \sqrt{\frac{EZ_0}{A\tau}} \approx 2.8 \times 10^8 \text{V/m},$$

  with $A = \pi(d/2)^2$ being the area of the beam and $Z_0 = \sqrt{\frac{\mu_0}{\varepsilon_0}} = 377\Omega$ being the free space impedance.
- t_0 is the center of the pulse.

The electric field in Eq. 3.35 has been used in simulations for paper II and paper III. In paper IV, four Gaussian pulses each having similar form as in Eq. 3.35 with time delays is used.

Chapter 4

Multiple Exciton Generation and Extraction

4.1 Multiple Exciton Generation (MEG)

MEG is a process in which the absorption of a single high-energy photon results in the creation of more than one electron hole-pair (exciton) [15, 31, 66–68]. MEG is a result of Coulomb electron-electron interaction in the form of an inverse Auger process also called impact ionization (II). It is a radiation-less transition in which a relaxation of charge carrier with high energy causes a creation of another electron hole pair as depicted in Fig. 4.1. MEG effect is more significant in QDs than in bulk structures due to the forced overlap

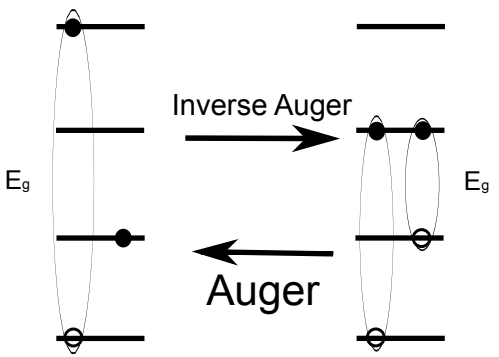

Figure 4.1: Auger recombination versus its inverse process. From left to right a relaxation from the upper level causes a creation of a new exciton. From right to left, the inverse process where the recombination of an electron and a hole causes an excitation to a higher energy.

of electronic wavefunctions [16]. Furthermore, spatial confinement leads to the absence of conservation of momentum, modified carrier-cooling rates and reduced dielectric screening, which altogether account for enhanced MEG in QDs [16, 69]. For an efficient design of solar cells utilizing MEG, a detailed microscopic description of MEG in QDs is essential.

Schaller and Klimov in 2004 [31] demonstrated the first efficient MEG in PbSe QDs. Following their work, a significant attention has been given towards the study of QD based systems for efficient MEG by several groups [2, 15, 69, 70]. The common QDs used for efficient MEG study include Lead Chalcogenide QDs (PbS and PbSe), Cadmium Chalcogenide QDs, Indium based QDs (InAs and InP) and Silicon QDs [30, 71–75]. Experimentally the most common setup to measure MEG is by using ultrafast transient absorption spectroscopy [76]. This is due to the fact that the main processes of bi-exciton formation and Auger recombination occur on the ps time scale [77]. This is a much faster timescale as compared to the lifetimes of single excitons (ns time scale) [78].

In this chapter the method used to calculate the yield, a measure of how many electron-hole pairs are created upon absorption of a single photon with energy much higher than the band gap, will be discussed. Two different ways have been used to measure the yield. In the case where there is no extraction and injection process (paper II), the ratio between the total number of recombination at the band gap to the total absorbed energy is used to evaluate the yield. In Paper III where extraction and injection processes are considered, the ratio between the total extraction to the total absorbed energy is used instead to calculate the yield. In both cases, a similar type of quantum dot as described in chapter 3 was used. Below a summary of the papers Paper II and Paper III is given.

4.2 MEG Yield (Paper II)

A quantum yield of about 20% due to MEG in lead chalcogenide nanocrystals has been reported by Karki et.al. [65]. This means that an absorbed photon generates in average 1.2 electron-hole pairs. Here we calculate the yield of a PbS quantum dot by properly defining the total number of recombination and total absorbed energy using the density matrix approach.

The time evolution of the density matrix is solved in the Lindblad form [79] which also consistently takes into account the relaxation processes by the Lindblad jump operators:

$$\hbar\frac{d}{dt}\hat{\rho}_S(t) = i[\hat{\rho}_S(t), \hat{H}_{\text{eff}}(t)] + \sum_{j=1}^{N_{\text{jump}}} \Gamma_j \left[\hat{L}_j\hat{\rho}_S(t)\hat{L}_j^\dagger - \frac{1}{2}\left(\hat{\rho}_S(t)\hat{L}_j^\dagger\hat{L}_j + \hat{L}_j^\dagger\hat{L}_j\hat{\rho}_S(t)\right)\right] \tag{4.1}$$

where in Eq. 4.1 the Hamiltonian of the system in single particle basis is given by

$$\hat{\mathrm{H}}_{\mathrm{eff}}(t) = \underbrace{\sum_i E_i \hat{a}_i^\dagger \hat{a}_i + \hat{H}_{\mathrm{ee}}}_{\hat{H}_0} + \hat{H}_I(t), \tag{4.2}$$

which is the sum of the time independent Hamiltonian $\hat{H}_0$ and the time dependent interaction Hamiltonian $\hat{H}_I(t)$. The time independent Hamiltonian $\hat{H}_0$ is composed of the total single particle energies and the electron-electron interaction term $\hat{H}_{\mathrm{ee}}$ as described in chapter 2. The interaction Hamiltonian $\hat{H}_I(t)$ is given by

$$\hat{H}_I(t) = -\hat{\mu} \cdot \vec{E}(t). \tag{4.3}$$

where $\hat{\mu}$ is the electric dipole operator and $\vec{E}(t)$ is the time dependent electric field described in section 3.6.

The following jump operators were considered in relation to the different decoherence mechanisms. The energy levels are labeled according to Fig. 4.2

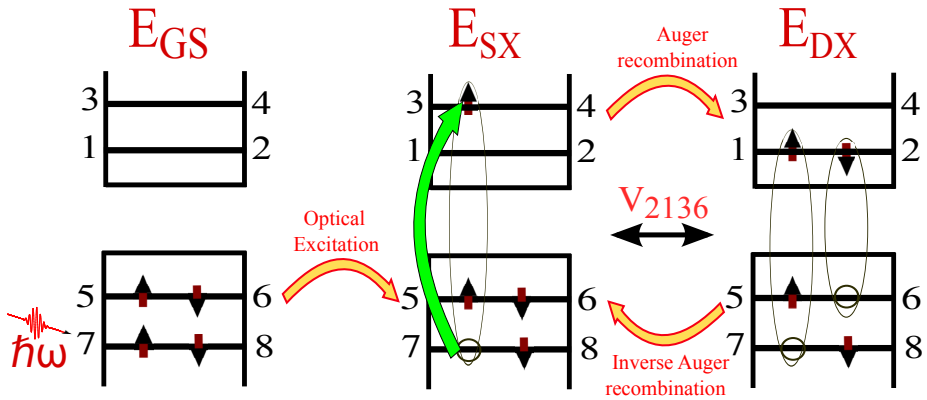

Figure 4.2: Schematic single particle energies for PbS quantum dot indicating the ground state E_{GS}, single exciton E_{SX} and double exciton E_{DX} in many particle configuration. Levels associated with spin up are labeled by odd numbers and those with spin down are labeled with even numbers. Optical excitation upon absorption of photon followed by Auger recombination and the inverse process is shown.

Relaxation in the conduction band

$$\hat{L}_{\mathrm{rel}} = \hat{a}_{1\uparrow}^\dagger \hat{a}_{3\uparrow} + \hat{a}_{2\downarrow}^\dagger \hat{a}_{4\downarrow}, \qquad \text{with strength} \qquad \Gamma_{\mathrm{Relaxation}}. \tag{4.4}$$

Relaxation in the valence band

$$\hat{L}_{\mathrm{rel}} = \hat{a}_{7\uparrow}^\dagger \hat{a}_{5\uparrow} + \hat{a}_{4\downarrow}^\dagger \hat{a}_{8\downarrow}, \qquad \text{with strength} \qquad \Gamma_{\mathrm{Relaxation}}. \tag{4.5}$$

Recombination across the band gap

$$\hat{L}_{\text{rec}} = \hat{a}^{\dagger}_{5\uparrow}\hat{a}_{1\uparrow} + \hat{a}^{\dagger}_{6\downarrow}\hat{a}_{2\downarrow}, \qquad \text{with strength} \qquad \Gamma_{\text{Recombination}}. \tag{4.6}$$

Dephasing in the conduction band

$$\begin{aligned} \hat{L}_{\text{deph}} &= \hat{a}^{\dagger}_{1\uparrow}\hat{a}_{1\uparrow} + \hat{a}^{\dagger}_{2\downarrow}\hat{a}_{2\downarrow}, \qquad \text{with strength} \qquad \Gamma_{\text{Dephasing}} \\ \hat{L}_{\text{deph}} &= \hat{a}^{\dagger}_{3\uparrow}\hat{a}_{3\uparrow} + \hat{a}^{\dagger}_{4\downarrow}\hat{a}_{4\downarrow}, \qquad \text{with strength} \qquad \Gamma_{\text{Dephasing}}. \end{aligned} \tag{4.7}$$

Dephasing in the valence band

$$\begin{aligned} \hat{L}_{\text{deph}} &= \hat{a}^{\dagger}_{5\uparrow}\hat{a}_{5\uparrow} + \hat{a}^{\dagger}_{6\downarrow}\hat{a}_{6\downarrow}, \qquad \text{with strength} \qquad \Gamma_{\text{Dephasing}} \\ \hat{L}_{\text{deph}} &= \hat{a}^{\dagger}_{7\uparrow}\hat{a}_{7\uparrow} + \hat{a}^{\dagger}_{8\downarrow}\hat{a}_{8\downarrow}, \qquad \text{with strength} \qquad \Gamma_{\text{Dephasing}}. \end{aligned} \tag{4.8}$$

These jump operators are defined in such a way that they all conserve the total spin.

In Fig. 4.2 the lowest eight single particle states for a 4 nm quantum dot, 4 in the valence band and 4 in the conduction band, are considered. All possible Coulomb interaction matrix elements as well as the transition matrix elements were calculated based on the methods discussed in chapter 3. We define the recombination rate as

$$\text{Rec(t)} = \Gamma_{\text{Recombination}}\, Tr\{\hat{L}_{\text{rec}}\hat{\rho}\hat{L}^{\dagger}_{\text{rec}}\}. \tag{4.9}$$

Integrating Eq. 4.9 over time provides the total number of recombined electron-hole pairs generated by the pulse.

$$\text{Number of recombinations} = \int_{-\infty}^{\infty} \text{dt Rec(t)}. \tag{4.10}$$

In addition, the power transferred to the system by the oscillating field has to be calculated in order to obtain the yield. Here we show that this quantity can be calculated via two different approaches which provided similar numerical results for integrated values over time. The time rate of the expectation value of an arbitrary time independent observable $\hat{O}$ can be evaluated as [80]

$$\frac{d}{dt}\langle\hat{O}\rangle = \frac{d}{dt}[\text{Tr}\{\hat{O}\hat{\rho}(t)\}] = \text{Tr}\{\hat{O}\frac{d}{dt}\hat{\rho}(t)\}, \tag{4.11}$$

where

$$\frac{d}{dt}\hat{\rho}(t) = \frac{i}{\hbar}[\hat{\rho}_S(t), \hat{H}_{\text{eff}}(t)] + \sum_{j=1}^{N_{\text{jump}}} \Gamma_j \left[\hat{L}_j\hat{\rho}_S(t)\hat{L}^{\dagger}_j - \frac{1}{2}\left(\hat{\rho}_S(t)\hat{L}^{\dagger}_j\hat{L}_j + \hat{L}^{\dagger}_j\hat{L}_j\hat{\rho}_S(t)\right)\right]. \tag{4.12}$$

The power $\mathrm{P(t)}$ can be evaluated by the energy balance for the interaction with the light field [42]. Considering the energy of the system as $\langle \hat{H}_0 \rangle$ one obtains the time rate of change of the system energy or rate of energy absorption [42] as

$$
\begin{aligned}
\frac{d}{dt}\langle \hat{H}_0 \rangle =& \mathrm{Tr}\{\hat{H}_0 \frac{d}{dt}\hat{\rho}(t)\} \qquad (4.13)\\
=& \mathrm{Tr}\left\{ \hat{H}_0 \frac{i}{\hbar}[\hat{\rho}_S(t), \hat{H}_{\mathrm{eff}}(t)] \right\} \\
&+ \sum_{j=1}^{N_{\mathrm{jump}}} \Gamma_j \mathrm{Tr}\left\{ \hat{H}_0 \left[\hat{L}_j \hat{\rho}_S(t) \hat{L}_j^\dagger - \frac{1}{2}(\hat{\rho}_S(t)\hat{L}_j^\dagger \hat{L}_j + \hat{L}_j^\dagger \hat{L}_j \hat{\rho}_S(t)) \right] \right\} \\
=& \mathrm{Tr}\left\{ \left(\frac{i}{\hbar}[\hat{H}_{\mathrm{eff}}(t), \hat{H}_0] + \sum_{j=1}^{N_{\mathrm{jump}}} \Gamma_j \left[\hat{L}_j \hat{H}_0 \hat{L}_j^\dagger - \frac{1}{2}(\hat{H}_0 \hat{L}_j^\dagger \hat{L}_j + \hat{L}_j^\dagger \hat{L}_j \hat{H}_0) \right] \right) \hat{\rho}_S(t) \right\} \\
=& \mathrm{Tr}\left\{ \left(\frac{i}{\hbar}[\hat{H}_I(t), \hat{H}_0] + \sum_{j=1}^{N_{\mathrm{jump}}} \Gamma_j \left[\hat{L}_j \hat{H}_0 \hat{L}_j^\dagger - \frac{1}{2}(\hat{H}_0 \hat{L}_j^\dagger \hat{L}_j + \hat{L}_j^\dagger \hat{L}_j \hat{H}_0) \right] \right) \hat{\rho}_S(t) \right\} \\
=& \underbrace{\left\langle \frac{i}{\hbar}[\hat{H}_I(t), \hat{H}_0] \right\rangle}_{\mathrm{P(t)}} + \sum_{j=1}^{N_{\mathrm{jump}}} \Gamma_j \underbrace{\left\langle \hat{L}_j \hat{H}_0 \hat{L}_j^\dagger - \frac{1}{2}(\hat{H}_0 \hat{L}_j^\dagger \hat{L}_j + \hat{L}_j^\dagger \hat{L}_j \hat{H}_0) \right\rangle}_{\dot{Q}_j},
\end{aligned}
$$

where $\mathrm{P(t)}$ is the power transferred from the pulse to the system and $\dot{Q}_j$ is the energy transfer by the jump process j. Alternatively one can consider the energy of the system as

$\langle \hat{H}_{\text{eff}} \rangle$. In this case

$$
\begin{aligned}
\frac{d}{dt}\langle \hat{H}_{\text{eff}}(t)\rangle =& \text{Tr}\{\hat{H}_{\text{eff}}(t)\frac{d}{dt}\hat{\rho}(t)\} + \text{Tr}\{\rho(t)\frac{d}{dt}\hat{H}_{\text{eff}}(t)\} \\
=& \underbrace{\text{Tr}\left\{\hat{H}_{\text{eff}}(t)\frac{i}{\hbar}[\hat{\rho}_S(t), \hat{H}_{\text{eff}}(t)]\right\}}_{=0} \\
&+ \sum_{j=1}^{N_{\text{jump}}} \Gamma_j \text{Tr}\left\{\hat{H}_{\text{eff}}(t)\left[\hat{L}_j\hat{\rho}_S(t)\hat{L}_j^\dagger - \frac{1}{2}(\hat{\rho}_S(t)\hat{L}_j^\dagger\hat{L}_j + \hat{L}_j^\dagger\hat{L}_j\hat{\rho}_S(t))\right]\right\} \\
&+ \text{Tr}\left\{\rho(t)\frac{d}{dt}\hat{H}_{\text{I}}(t)\right\} \\
=& \text{Tr}\left\{\left(\frac{d}{dt}\hat{H}_{\text{I}}(t) + \sum_{j=1}^{N_{\text{jump}}} \Gamma_j\left[\hat{L}_j\hat{H}_{\text{eff}}\hat{L}_j^\dagger - \frac{1}{2}(\hat{H}_{\text{eff}}\hat{L}_j^\dagger\hat{L}_j + \hat{L}_j^\dagger\hat{L}_j\hat{H}_{\text{eff}})\right]\right)\hat{\rho}_S(t)\right\} \\
=& \underbrace{\left\langle \frac{d}{dt}\hat{H}_{\text{I}}(t)\right\rangle}_{\text{P(t)}} + \sum_{j=1}^{N_{\text{jump}}} \Gamma_j \underbrace{\left\langle \hat{L}_j\hat{H}_{\text{eff}}\hat{L}_j^\dagger - \frac{1}{2}(\hat{H}_{\text{eff}}\hat{L}_j^\dagger\hat{L}_j + \hat{L}_j^\dagger\hat{L}_j\hat{H}_{\text{eff}})\right\rangle}_{\dot{Q}_j},
\end{aligned}
\tag{4.14}
$$

The evaluation of the power transferred to the system from the light field based on Eq. 4.13 and Eq. 4.14 provide similar numerical values. For the yield calculation in paper II the power is calculated based on Eq. 4.13, i.e.

$$
\text{P(t)} = \left\langle \frac{i}{\hbar}[\hat{H}_I(t), \hat{H}_0]\right\rangle. \tag{4.15}
$$

The absorbed energy is obtained by integrating Eq.4.15 over time

$$
\text{Absorbed Energy} = \int_{-\infty}^{t} \text{dtP(t)} = \int_{-\infty}^{t} dt\left\langle \frac{i}{\hbar}[\hat{H}_I(t), \hat{H}_0]\right\rangle. \tag{4.16}
$$

The yield is a measure of the total number of recombined electron-hole pairs per absorbed photon. In this regard, it is defined as the ratio between the number of recombinations and the absorbed photons.

$$
\text{Yield} = \frac{\text{Number of recombination}}{\text{Absorbed Energy}} \times \hbar\omega_{\text{pulse}}. \tag{4.17}
$$

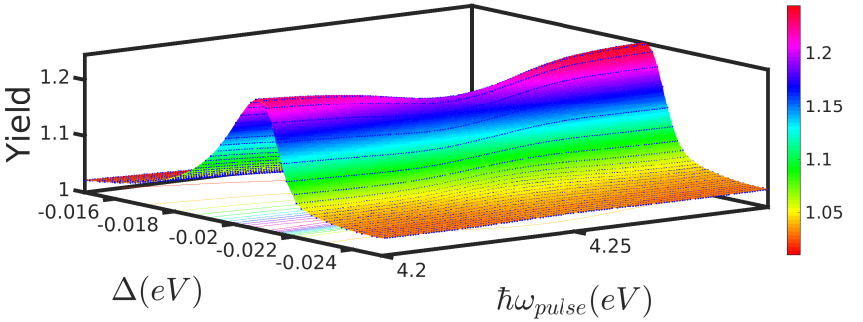

Figure 4.3: A yield as a function of pulse energy and a detuning between the single exciton and the double exciton.Δ is a parameter that shifts the band gap. As a result, the level energies in the conduction band increases by this amount. This way the double exciton energy and the single exciton energy can be effectively separated by Δ. [From paper II]

Fig. 4.3 shows the calculated yield as a function of the pulse energy $\hbar\omega_{\text{pulse}}$ and the detuning Δ between the single exciton and double exciton energies. It is obtained using the formula in Eq. 4.17. A yield of 1.2 is obtained for the model system considered as it can be seen from Fig. 4.3 close to $\Delta \approx -0.0215$ eV. The calculated value for the yield agrees very well with the experimentally measured MEG yield in Ref. [65].

We were also able to describe the time evolution of the excitons for $\Delta = -0.0215$ eV where the single and double excitons are very close in energy. We are interested in the time evaluation for the two excitons $|SX\rangle$ and $|DX\rangle$. However, these states mix highly in the many-body spectrum ($|22\rangle$ and $|26\rangle$) which are both singlets. To better describe the time evolution of the excitons $|SX\rangle$ and $|DX\rangle$, a basis transformation from the many-body representation to exciton representation as described in Eqs. 4.18 and 4.19 is done. This allows to follow the evolution of the individual excitons. Fig. 4.4 show the time evolution of the ground state $|G\rangle$, low energy single exciton $|ex\rangle$, high energy single exciton $|SX\rangle$ and double exciton $|DX\rangle$ states. In addition the time evolution of the two many-body states $|22\rangle$ and $|26\rangle$ are also shown. The transformation to the exciton basis satisfy,

$$|22\rangle \approx \alpha_1|SX\rangle + \beta_1|DX\rangle, \tag{4.18}$$

and

$$|26\rangle \approx \alpha_2|SX\rangle + \beta_2|DX\rangle, \tag{4.19}$$

such that in terms of these coefficients the probability for the double exciton and single exciton is given by

$$\rho_{\text{DX,DX}} = \langle DX|\rho|DX\rangle = \alpha_1^2\rho_{26,26} + \alpha_2^2\rho_{22,22} - 2\alpha_1\alpha_2\mathcal{R}\{\rho_{22,26}\}, \tag{4.20}$$

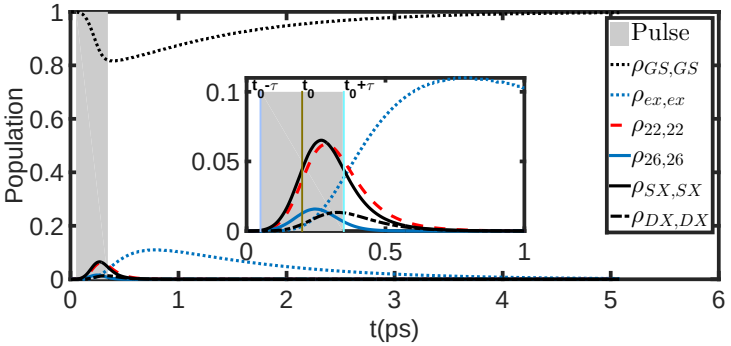

Figure 4.4: Time evolution for selected many particle states for $\Delta = -0.0215$ eV and $\hbar\omega_{\text{pulse}} = 4.255$ eV. An increased pulse area of $\Theta = \pi/2$ is used in order to emphasise the effect. The grey area depicts the duration of the pulse. The inset is an enlargement for small times and populations. [From paper II]

and

$$\rho_{SX,SX} = \langle SE|\rho|SX\rangle = \beta_1^2\rho_{26,26} + \beta_2^2\rho_{22,22} - 2\beta_1\beta_2\mathcal{R}\{\rho_{22,26}\}, \tag{4.21}$$

respectively.

The gray region in Fig. 4.4 denotes the pulse width, where coherent transfer dominates. The pulse is initially in resonance with the $|SX\rangle$ which is the first to be excited. The Coulomb ee interaction (inverse Auger recombination) causes population transfer from $|SX\rangle$ to $|DX\rangle$ around $t = t_0$. The single exciton state $|ex\rangle$ can be created by a competing relaxation process from $|SX\rangle$ which starts to grow within the pulse window. After the pulse, both the $|SX\rangle$ and $|DX\rangle$ loses their populations via recombination.

4.3 MEG Yield Optimization with Extraction and Injection (Paper III)

In paper III the yield is calculated with additional processes involving extraction and injection of electrons as shown in Fig. 4.5. The focus here is to determine parameter regimes in which the total number of extraction of charged particles from the band edges is optimal per single absorbed photon. The main parameter of interest, the yield is in this case defined as

$$\text{Yield} = \frac{\text{Number of extraction}}{\text{Absorbed Energy}} \times \hbar\omega_{\text{pulse}}, \tag{4.22}$$

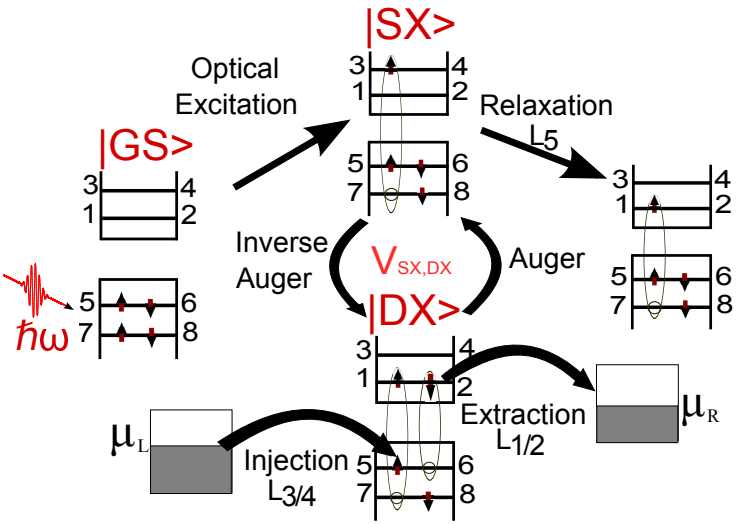

Figure 4.5: The various physical processes considered in the study namely, optical excitation by a resonant pulse, Auger recombination, extraction and injection to and from a reservoir with chemical potential μ_R and μ_L respectively. In addition we consider relaxation, which is competing with the inverse Auger process. From paper III

where the average number of extracted electron is given by

$$\text{Number of extractions} = \int_{-\infty}^{\infty} \mathrm{dt}\, \mathrm{Ext}(t), \tag{4.23}$$

with the extraction rate

$$\mathrm{Ext(t)} = \sum_{i=1,2} \Gamma_{\mathrm{Ext}}\, Tr\{\hat{L}_i \hat{\rho} \hat{L}_i^{\dagger}\}, \tag{4.24}$$

and the absorbed energy which is the total energy transferred from the light pulse to the dot is given as

$$\text{Absorbed Energy} = \int_{-\infty}^{t} \mathrm{dt}\, \mathrm{P(t)}. \tag{4.25}$$

The power $\mathrm{P(t)}$ in Eq. 4.25 is evaluated based on Eq. 4.14

$$\mathrm{P(t)} = \left\langle \frac{\partial \hat{H}_I(t)}{\partial t} \right\rangle = e\langle \hat{z} \rangle \dot{E}(t). \tag{4.26}$$

The model system used and all possible processes are shown in the schematics in Fig. 4.5. For the levels in Fig. 4.5 the convention that carriers with spin up $\uparrow$ occupy odd numbered

levels and those with spin down $\downarrow$ occupy even numbered single particle levels is used in all the definitions. Regarding the dissipative processes due to coupling with the environment, the following processes are taken into account in the model cf. Fig. 4.5:
Extraction from the conduction band edge

$$\hat{L}_1 = \hat{a}_{1\uparrow} \text{ and } \hat{L}_2 = \hat{a}_{2\downarrow}, \qquad \text{with strength } \Gamma_{\text{Ext}}.$$

Injection into the valence band edge

$$\hat{L}_3 = \hat{a}^\dagger_{5\uparrow} \text{ and } \hat{L}_4 = \hat{a}^\dagger_{6\downarrow}, \qquad \text{with strength } \Gamma_{\text{Inj}}.$$

Relaxation in the conduction band

$$\hat{L}_5 = \hat{a}^\dagger_{1\uparrow}\hat{a}_{3\uparrow} + \hat{a}^\dagger_{2\downarrow}\hat{a}_{4\downarrow}, \qquad \text{with strength } \Gamma_{\text{Rel}}.$$

Relaxation in the valence band

$$\hat{L}_6 = \hat{a}^\dagger_{7\uparrow}\hat{a}_{5\uparrow} + \hat{a}^\dagger_{4\downarrow}\hat{a}_{8\downarrow}, \qquad \text{with strength } \Gamma_{\text{Rel}}.$$

Recombination across the band gap

$$\hat{L}_7 = \hat{a}^\dagger_{5\uparrow}\hat{a}_{1\uparrow} + \hat{a}^\dagger_{6\downarrow}\hat{a}_{2\downarrow}, \qquad \text{with strength } \Gamma_{\text{Rec}}.$$

In addition, dephasing of all states

$$\begin{aligned}
\hat{L}_8 &= \hat{a}^\dagger_{1\uparrow}\hat{a}_{1\uparrow} + \hat{a}^\dagger_{2\downarrow}\hat{a}_{2\downarrow}, \\
\hat{L}_9 &= \hat{a}^\dagger_{3\uparrow}\hat{a}_{3\uparrow} + \hat{a}^\dagger_{4\downarrow}\hat{a}_{4\downarrow}, \\
\hat{L}_{10} &= \hat{a}^\dagger_{5\uparrow}\hat{a}_{5\uparrow} + \hat{a}^\dagger_{6\downarrow}\hat{a}_{6\downarrow}, \\
\hat{L}_{11} &= \hat{a}^\dagger_{7\uparrow}\hat{a}_{7\uparrow} + \hat{a}^\dagger_{8\downarrow}\hat{a}_{8\downarrow},
\end{aligned} \qquad \text{with strength } \Gamma_{\text{Deph}}.$$

In all the definitions above, the jump operators are defined in such a way that the processes with different spin that involve levels with the same energies being added together. In doing so, they all conserve the total spin if the particle number is conserved. The different decoherence mechanisms (relaxation, recombination and dephasing) which are described in Eq. (4.1), can be associated to all forms of intrinsic scattering mechanisms other than electron-electron scattering, which has already been included in the effective Hamiltonian. The strength of these processes are all assumed phenomenologically in all the simulations by looking at typical timescales for such processes in quantum dots. The dephasing rate is assumed to be $\Gamma_{\text{Deph}} = 6$ meV which corresponds to $\tau_{\text{Deph}} = 0.11$ ps. As the recombination is typically the slowest process (larger than a nanosecond time scale unless for very weak coupling to the reservoir which is not a case considered here), we neglect this process in our study and set $\Gamma_{\text{Rec}} = 0$. We did a test calculation for a finite but small recombination rate which showed only very small changes of about 5% for $\Gamma_{\text{Rec}} = 0.1$ meV with

the corresponding rate in time units of $\tau_{\mathrm{Rec}} = 6.6$ ps, which is fairly large compared to the typical recombination rates in semiconductor dots.

In modeling the extraction and injection processes an energy requirement for the incoming and outgoing particles was set. The first scenario is injection of an electron from a reservoir to the upper level in the valence band of the quantum dots (5 or 6) depending on the spin. In this case, the initial system with particle number N has an energy $E(N)$. The requirement in this case is that the incoming particle should have an energy such that it occupies either the levels 5 or 6 depending on its spin. Defining $\Delta = 0.2eV$ to be a small energy margin above the highest occupied level in the valence band and also below the lowest level in the conduction band which is an energy associated with the electrochemical potential of the contacts. Due to the injection the system energy after the jump is increased from $E(N)$ to $E(N+1)$. As a result an electron can be injected from the left contact to the system only if the energy requirement

$$\big(E(N+1) - E(N)\big) \leq \big(E_g(4) - E_g(3)\big) + \Delta, \tag{4.27}$$

is fulfilled. Where in Eq. 4.27 above $E_g(N)$ denotes the ground state energy for N particles obtained from the diagonalisation of the dot Hamiltonian $\hat{H}_0$. In all the cases, for simplicity, the broadening of the states due to coupling with the reservoirs is neglected.

The second scenario is extraction of an electron from the lowest levels in the conduction band to the contacts. Similar to injection, an energy requirement for the electron to be extracted is such that

$$\big(E(N) - E(N-1)\big) \geq \big(E_g(5) - E_g(4)\big) - \Delta, \tag{4.28}$$

since the particle number in the quantum dot has be decreased by 1.

In this work a qualitative study of the parameter regimes for optimal yield is carried out. In this respect, the main results are summarized in Fig. 4.6. In the figure, the number of extraction (Fig. 4.6a), the absorbed energy (Fig. 4.6b) and the yield (Figs. 4.6c, 4.6d) are plotted as a function of the extraction and the injection rates. The current flow through the dot can be equally described by considering either the number of extractions or the number of injections. This is due to the fact that the number of injections, as obtained by summing over the jump processes 3 and 4, equals the number of extractions, as the system returns into the ground state with 4 electrons occupying the levels 5–8 for large times. It is shown in all cases that the increase in both injection and extraction rates results in an increased yield which is normally expected since the increase in these rates means a rapid extraction while the other competing processes are slow.

In MEG the single high energy exciton $|SX\rangle$ and $|DX\rangle$ are coupled via Coulomb interaction. After excitation, the population of the single exciton is transferred to the double exciton. In the absence of extraction, the population from the double exciton will transfer back to

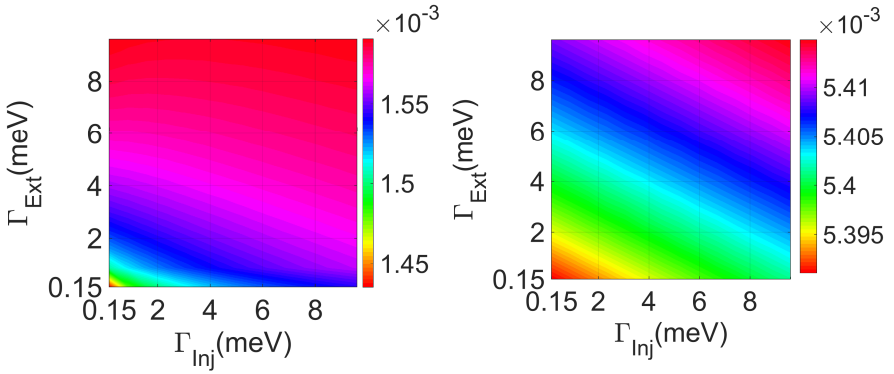

(a) Number of extraction $\Gamma_{\mathrm{Rel}} = 3.3$ meV

(b) Absorbed energy $\Gamma_{\mathrm{Rel}} = 3.3$ meV

(c) Yield $\Gamma_{\mathrm{Rel}} = 3.3$ meV

(d) Yield $\Gamma_{\mathrm{Rel}} = 1$ meV

Figure 4.6: Paper III: Number of extractions (a) and absorbed energy (b) for different reservoir coupling strengths. The ratio between these numbers determines the yield in panel (c). Panel (d) shows the yield for a reduced relaxation rate.

the single exciton and they will keep oscillating. In the case of large extraction rates, the charge carriers can actually be extracted from the double exciton state before they go back to the single exciton via Auger recombination.

In figure 4.6c a yield as a function of injection and extraction rate is given which varies between $\approx 1.13 - 1.25$ for a fixed relaxation rate $\Gamma_{\mathrm{Rel}} = 3.3$ meV. It can be seen that the increase in the yield is different for an increase of injection rate and extraction rate. The yield increases quicker and saturates faster for increasing the extraction rate compared to the increase in the injection rate. This is due to the fact that extraction involves the electrons in the conduction band, which are created as a result of the Coulomb electron-electron interaction. The yield increases following the creation of the double exciton after

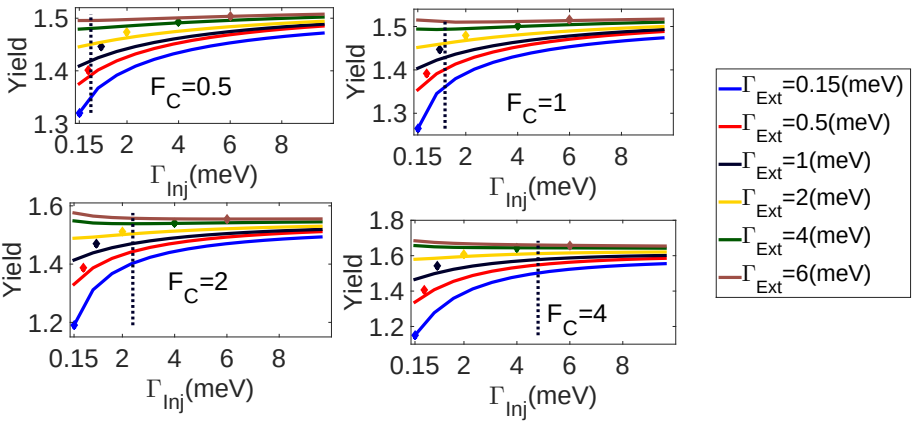

Figure 4.7: Yield as a function of the injection rates for different rates of extraction. Different strengths for the Auger coupling rate are applied in each panel. The vertical line denotes $\Gamma_{\mathrm{Inj}} = 2V^{ee}_{1263}$ and the diamonds refer to the points $\Gamma_{\mathrm{Inj}} = \Gamma_{\mathrm{Ext}}$. The relaxation rate $\Gamma_{\mathrm{Rel}} = 1$ meV is used here.

excitation and saturates. However for the injection rate, since it involves the electrons in the valence band, the yield increases only if the extraction rate is small. This increase is due to the fact that injection into the level 5/6 depending on the spin hinders the Auger process converting the $|DX\rangle$ state back to the $|SX\rangle$ state, see Fig. 4.5. This kills the coherent oscillations between the $|DX\rangle$ and $|SX\rangle$ state in the case of small extraction rate.

For small relaxation rate as shown in Figure 4.6d the overall yield increases compared to the case with higher relaxation rate as in Figure 4.6c. The reason is that a low relaxation rate results in a larger chance for the inverse Auger process to occur before the single exciton relaxes to some other low energy state. This way the creation of a double exciton is favored.

The MEG yield is highly dependent on the two competing processes. The rate of Auger (inverse Auger) scattering and the relaxation time scales. Fig. 4.7 shows the yield as a function of injection rate for the different strengths of the Coulomb coupling for the Auger terms. By modifying the strength of the Auger Coulomb matrix element, the yield as a function of the injection rate for varying values of extraction rate is studied. The dashed vertical line indicates the splitting energy between the single and double exciton energies which is about twice the Coulomb matrix element between them $|E_{SX} - E_{DX}| \approx 2|V^{ee}_{1263}|$. The diamonds on each line indicate the point at which the injection rate and the extraction rate becomes similar. The common trend from Fig. 4.7 is that an improved yield is obtained either by increasing the extraction rate or the Coulomb coupling between the single and double exciton states. In the regime where the Auger Coulomb coupling is dominant over the extraction rate, $2|V^{ee}_{1263}| > \Gamma_{\mathrm{Ext}}$, a small yield is obtained since the coherent oscillation between the single exciton and double exciton state is only damped by the re-

laxation processes. However, by injecting an electron into the valence band the double exciton state can be recovered. This way an increased yield can be obtained which saturates as $\Gamma_{\mathrm{Inj}} \gg 2|V^{ee}_{1263}|$. In the limit of high extraction rate $\Gamma_{\mathrm{Ext}} > 2|V^{ee}_{1263}|$ not much variation on the yield is obtained since the extraction is already high enough to guarantee a high yield.

Chapter 5

Two Dimensional Spectroscopy

This chapter describes the modeling of light matter interaction where combinations of time-delayed laser pulses are involved. Each pulse excites or de-excites the system creating either a coherence state or a population state based on the state of the system before the interaction. The aim is to study the dynamics of ultra-fast processes in quantum dot and molecular systems.

Multidimensional spectroscopy, specifically two dimensional (2D) optical spectroscopy, has been proven to be an efficient technique to provide an optimal information for studying the effect of an optical field on quantum systems [42, 81–89]. By exciting a sample (molecule, quantum dot, etc.), with properly designed pulses, information about the structure and dynamics of molecular systems [42, 82, 90], photosynthetic complexes [91, 92] and semiconductor nanostructures [93–95] can be obtained.

In paper IV, a simulation for excitonic system as a result of interaction with four collinear pulses[1] is studied. Theoretically, the emitted signal in conventional 2D spectroscopy can be obtained by calculating the third order response function as a function of the time delays [96–98]. Here, instead of perturbation expansion of the response function, we solve the equation of motion for the reduced density matrix in Lindblad form and calculate observables that represent different relaxation processes in the system. Our method can reproduce clear signals that can be used for interpretation of the system dynamics.

In a typical experiment a series of pulses which are time delayed excite the system. The time delay between the first and the second pulse is called the coherence time denoted as T_1 in this thesis (see Fig. 5.1). In this time the excitation of the system by the pulse creates a coherence which will be converted to either population or another coherence state by

[1] Collinear pulses are pulses which are all propagating in the same wave-vector direction $\vec{k}$.

the second pulse. After the second pulse the system evolves either in a population state or in a different coherence state than the initially created coherence. This time, which is the delay between the second and the third pulse, is called the population time denoted here as T_2. After the second pulse, in most of the cases the system is in population state, hence the name population time for T_2. After the population time, a third pulse excites the system to create a coherence state. Here the coherence evolves until the fourth (last) pulse arrives. The time delay between the third and the fourth pulse T_3 is also called coherence time. After the fourth pulse the signal is detected. The pair of first and second pulse is collectively called pump pulse and the third and fourth pulses are collectively called the probe pulse. By varying the delay between the pump and the probe pulses (the population time) a change in the system dynamics can be studied.

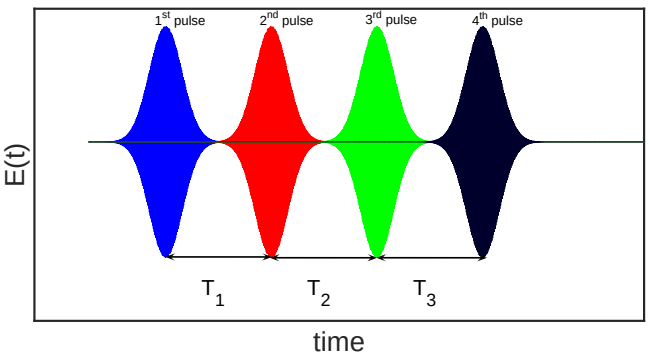

Figure 5.1: Pulse sequence in a four pulse setup. The time delays between the individual pulses is indicated.

5.1 Our Approach for Calculating 2D Signals

In the previous chapter on MEG the observables associated with different relaxation processes and absorbed energy were calculated by solving the density matrix in the Lindblad form. However, in chapter 4 the time dependent interaction Hamiltonian $\hat{H}_I(t)$ was modeled by a single oscillating field without phase modulation.

In 2D spectroscopy based on phase modulation, the interaction Hamiltonian contains four Gaussian modulated pulses with specific modulation frequencies which are time delayed. The system Hamiltonian in this case for an arbitrary quantum system can be written as

$$\hat{H}_{\text{eff}}(t) = \underbrace{\sum_i E_i a_i^\dagger a_i + \hat{H}_{ee}}_{\hat{H}_0} + \hat{H}_I(t), \tag{5.1}$$

with

$$\hat{H}_I(t) = -\hat{\mu} \cdot \vec{E}(t). \tag{5.2}$$

where $\hat{\mu}$ is the electric dipole operator and $\vec{E}(t)$ is the electric field. In the following a scheme of data collection for a typical experiment with phase modulation will be outlined. A "train" of four pulses labeled from 1 to 4 with a well defined inter-pulse delay T_1 between pulse 1 and 2, T_2 between pulse 2 and 3 and T_3 between pulse 3 and 4 is prepared. The sample is then excited by a number of pulse trains labeled by m each separated by an inter-train delay T for a certain combination of inter-pulse delays. The electric field for the mth train is given by

$$E^m(t) = E_1^m(t) + E_2^m(t) + E_3^m(t) + E_4^m(t), \tag{5.3}$$

where m counts the number of repetition which typically run from zero up to few thousands. Each pulse within the train in Eq. 5.3 is described as

$$\begin{aligned}
E_1^m(t) =& E_{01}^m \exp\left[\frac{-4\ln 2(t-\mathcal{T}_0-mT)^2}{\tau_1^2}\right]\cos\Big(\omega(t-\mathcal{T}_0-mT) + \underbrace{2\pi\Omega_1 mT}_{\phi_1}\Big),\\
E_2^m(t) =& E_{02}^m \exp\left[\frac{-4\ln 2(t-\mathcal{T}_1-mT)^2}{\tau_2^2}\right]\cos\Big(\omega(t-\mathcal{T}_1-mT) + \underbrace{2\pi\Omega_2 mT}_{\phi_2}\Big),\\
E_3^m(t) =& E_{03}^m \exp\left[\frac{-4\ln 2(t-\mathcal{T}_2-mT)^2}{\tau_3^2}\right]\cos\Big(\omega(t-\mathcal{T}_2-mT) + \underbrace{2\pi\Omega_3 mT}_{\phi_3}\Big),\\
E_4^m(t) =& E_{04}^m \exp\left[\frac{-4\ln 2(t-\mathcal{T}_3-mT)^2}{\tau_4^2}\right]\cos\Big(\omega(t-\mathcal{T}_3-mT) + \underbrace{2\pi\Omega_4 mT}_{\phi_4}\Big),
\end{aligned} \tag{5.4}$$

with

$$\begin{aligned}
\mathcal{T}_0 =& t_0,\\
\mathcal{T}_1 =& T_1 + t_0,\\
\mathcal{T}_2 =& T_1 + T_2 + t_0,\\
\mathcal{T}_3 =& T_1 + T_2 + T_3 + t_0,
\end{aligned} \tag{5.5}$$

where t_0 is the the center of the first pulse and T_1, T_2 and T_3 are the inter-pulse delays described above. $\Omega_1 - \Omega_4$ are the modulation frequencies corresponding to the pulses $1-4$, respectively. $\phi_i = 2\pi\Omega_i mT$ is the repetition dependent phase modulation for the ith pulse. In addition, E_{0i}^m is the electric field amplitude for the ith pulse in the mth train,

τ_i is the pulse width for the ith pulse, ω is the carrier frequency of the pulses. A schematic diagram for the pulse sequences considering the first two pulse trains is shown in Fig. 5.2.

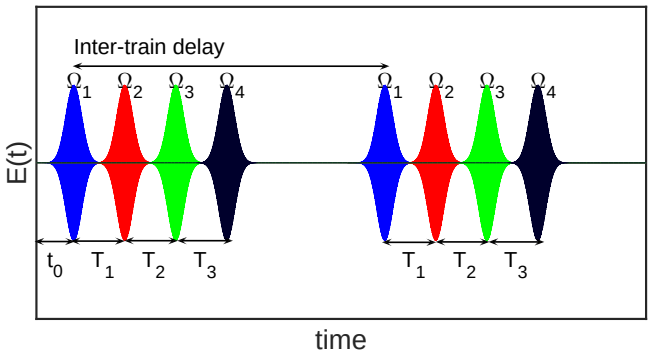

Figure 5.2: Paper IV: Pulse sequences used in the simulation as a function of time. Inter-pulse delays and inter-train delays are indicated. The first two trains of pulses are shown.

In practice, as described in Ref. [99], a train of collinear pulse pairs with a relative phase modulation at frequency ($\Omega_{21} = \Omega_2 - \Omega_1$) can be created. When a molecule or a quantum system is excited by such a train, the excited state population contains an interference contribution with a phase which is also modulated at the frequency Ω_{21}. As a result the modulated population gives rise to a time varying fluorescence signal which can be detected.

In the case of four pulse trains as described in Ref. [100] the pulses can be grouped into two independently phase-modulated pulse pairs at frequencies Ω_{21} and Ω_{43}. Here we expect different contributions to the interference depending on the combination of the modulation frequencies. Major contribution can be obtained from the so-called *linear interference contributions* to the excited state population. These populations oscillate with phases at the fundamental frequencies Ω_{21} and Ω_{43}. In addition, due to optical nonlinearities of the system one obtains population terms that oscillate at the combined so called the "sum" ($\Omega_{43} + \Omega_{21}$) and "difference" ($\Omega_{43} - \Omega_{21}$) frequencies. These signals oscillating with the "sum" and "difference" frequencies in phase modulation 2D spectroscopy are analogous to the rephasing and the non-rephasing pathway in conventional 2D spectroscopy based on third order response function [100].

In all the simulations we fix the modulation frequencies and the inter-train time delay motivated by experimental settings following Ref. [66] but with small variation for the purpose of quicker data acquisition. For the inter-train time delay $T = 14$ ns is used and

the individual modulation frequencies are

$$\begin{aligned} \Omega_1 =& 51.4 \text{ MHz}, \\ \Omega_2 =& 51.9 \text{ MHz}, \\ \Omega_3 =& 54.2 \text{ MHz}, \\ \Omega_4 =& 55 \text{ MHz}. \end{aligned} \tag{5.6}$$

The modulation frequencies in Eq. 5.6 correspond to the radio frequencies used to drive the acousto-optic modulators in typical experiments [66, 100, 101].

The possible linear combinations for the above modulation frequencies are

$$\begin{aligned} \Omega_{21} =& \Omega_2 - \Omega_1 = 500 \text{ kHz}, \\ \Omega_{31} =& \Omega_3 - \Omega_1 = 2800 \text{ kHz}, \\ \Omega_{41} =& \Omega_4 - \Omega_1 = 3600 \text{ kHz}, \\ \Omega_{32} =& \Omega_3 - \Omega_2 = 2300 \text{ kHz}, \\ \Omega_{42} =& \Omega_4 - \Omega_2 = 3100 \text{ kHz}, \\ \Omega_{43} =& \Omega_4 - \Omega_3 = 800 \text{ kHz}. \end{aligned} \tag{5.7}$$

In addition, by adding and subtracting the combinations above, non-linear terms can be obtained. Here the two non-linear combinations associated with the sum (non-rephasing) and difference (rephasing) combinations are

$$\begin{aligned} \Omega_{\text{Non-Rephasing}} =& \Omega_{43} + \Omega_{21} = 1300 \text{ kHz}, \\ \Omega_{\text{Rephasing}} =& \Omega_{43} - \Omega_{21} = 300 \text{ kHz}, \end{aligned} \tag{5.8}$$

respectively.

5.2 2D Data Collection and Analysis Example

In order to demonstrate the method of calculating 2D spectrum, an example based on a three level model system is discussed in this section. A step by step process from collecting the data in time domain to the Fourier transformed spectra will be described.

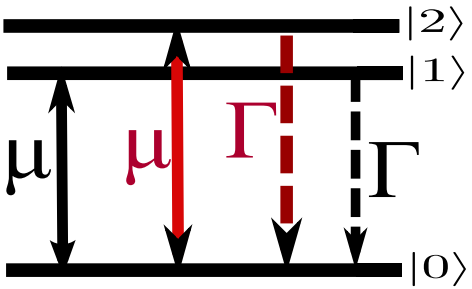

Figure 5.3: Energy level diagram and possible transitions for the three level system considered in the simulation.

Fig 5.3 shows a schematic diagram of the energy levels and the allowed transitions. Both levels $|1\rangle$ and $|2\rangle$ are coupled to the ground state via a dipole transition with transition matrix elements $\mu_{10} = \mu_{20} = \mu$. Relaxation from both levels to the ground state $|0\rangle$ is allowed as indicated in the figure. The signal in this case can be obtained by measuring the total relaxation from both levels to the ground state.

For the simulation results in this section the following parameters were assumed.

The energy levels are:

$$\begin{aligned} E_0 &= 0, \\ E_1 &= 1.5 \text{ eV}, \\ E_2 &= 2 \text{ eV}, \end{aligned} \tag{5.9}$$

Scattering terms describing the relaxation from $|2\rangle \rightarrow |0\rangle$ and $|1\rangle \rightarrow |0\rangle$ are assumed as:

$$\Gamma_{20} = \Gamma_{10} = 0.413 \text{ meV}, \text{ corresponding to } 2\pi\tau_{20} = 2\pi\tau_{10} = 10 \text{ ps}. \tag{5.10}$$

In addition, equal pure dephasing from all the levels are assumed as:

$$\Gamma_{\text{Deph}} = 51.7 \text{ meV}, \text{ corresponding to } 2\pi\tau_{\text{Deph}} = 80 \text{ fs}. \tag{5.11}$$

Pulse parameters used in the simulations are:

$$\begin{aligned} \tau_1 = \tau_2 = \tau_3 = \tau_4 &= 10 \text{ fs}, \\ \hbar\omega_{\text{pulse}} &= 1.75 \text{ eV}, \end{aligned} \tag{5.12}$$

which is tuned exactly in between the levels. These type of models are known to display both diagonal and cross peaks in the 2D spectrum [85]. The values above are adjusted to obtain a signal with reasonable computational cost. Hence we are not referring to any specific experimental system.

The relaxation rate for an arbitrary relaxation process is given by:

$$\mathrm{Rel(t)} = \Gamma_{\mathrm{rel}} Tr\{\hat{L}_{\mathrm{rel}} \hat{\rho}(t) \hat{L}^{\dagger}_{\mathrm{rel}}\}, \tag{5.13}$$

where $(\Gamma_{\mathrm{rel}}/\hbar)$ is the rate at which the process in question happens, $\hat{L}_{\mathrm{rel}}$ is the jump operator describing the specific transition by the process in the Lindblad equation (see Eq. 5.14). This can for example be $\hat{L}_{\mathrm{rel}} = a_0^{\dagger} a_1$ for relaxation from state $|1\rangle$ to $|0\rangle$ where $a^{\dagger}$ and a are creation and annihilation operators, respectively. The total relaxation is defined as the integrated relaxation rate $\mathrm{Rel(t)}$ over time, which is the quantity of interest that provides the signals. The density matrix $\hat{\rho}(t)$ in Eq. 5.13 is obtained by solving the equation of motion in the Lindblad form [79]:

$$\hbar \frac{d}{dt} \hat{\rho}_S(t) = i[\hat{\rho}_S(t), \hat{H}_{\mathrm{eff}}(t)] + \sum_{j=1}^{N_{\mathrm{jump}}} \Gamma_j \left[\hat{L}_j \hat{\rho}_S(t) \hat{L}_j^{\dagger} - \frac{1}{2} \left(\hat{\rho}_S(t) \hat{L}_j^{\dagger} \hat{L}_j + \hat{L}_j^{\dagger} \hat{L}_j \hat{\rho}_S(t) \right) \right], \tag{5.14}$$

where the Hamiltonian $\hat{H}_{\mathrm{eff}}$ is a sum of the time independent Hamiltonian $\hat{H}_0$, and the interaction Hamiltonian $\hat{H}_I(t)$

$$\hat{H}_{\mathrm{eff}} = \hat{H}_0 + \hat{H}_I(t), \tag{5.15}$$

where

$$\hat{H}_I(t) = -\hat{\mu} \cdot \vec{E}^m(t). \tag{5.16}$$

In Eq. 5.16 $\hat{\mu}$ is the electric dipole transition operator, $\vec{E}^m(t)$ is the electric field for the mth train of pulses given in Eq. 5.4. For the model system shown in Fig. 5.3 we considered: Relaxation from $|2\rangle \rightarrow |0\rangle$

$$\hat{L}_{20} = \hat{a}_0^{\dagger} \hat{a}_2, \qquad \text{with strength} \qquad \Gamma_{20}, \tag{5.17}$$

Relaxation from $|1\rangle \rightarrow |0\rangle$

$$\hat{L}_{10} = \hat{a}_0^{\dagger} \hat{a}_1, \qquad \text{with strength} \qquad \Gamma_{10}, \tag{5.18}$$

Dephasing in the all the levels

$$\begin{aligned} \hat{L}_{00} &= \hat{a}_0^\dagger \hat{a}_0, \quad \text{with strength} \quad \Gamma_{00}, \\ \hat{L}_{11} &= \hat{a}_1^\dagger \hat{a}_1, \quad \text{with strength} \quad \Gamma_{11}, \\ \hat{L}_{22} &= \hat{a}_2^\dagger \hat{a}_2, \quad \text{with strength} \quad \Gamma_{22}, \end{aligned} \tag{5.19}$$

We solve the Lindblad equation (Eq. 5.14) numerically with the initial condition that at time zero all the population is in the ground state. The signals in the 2D map are obtained by evaluating the relaxation rates and integrating over the acquisition time $t_{\text{acquisition}}$ as:

$$\text{Rel}_{10} = \int_0^{t_{\text{acquisition}}} \text{dt}\ \Gamma_{10} \text{Tr}\{\hat{L}_{10}\hat{\rho}_S(t)\hat{L}_{10}^\dagger\}, \tag{5.20}$$

$$\text{Rel}_{20} = \int_0^{t_{\text{acquisition}}} \text{dt}\ \Gamma_{20} \text{Tr}\{\hat{L}_{20}\hat{\rho}_S(t)\hat{L}_{20}^\dagger\}, \tag{5.21}$$

For a fixed set of time delays $(T_1, T_2, T_3) = (0, 0, 0)$, the necessary steps of collecting data points will be demonstrated by considering the signal due to the sum of the total relaxation from $|1\rangle \rightarrow |0\rangle$ and $|2\rangle \rightarrow |0\rangle$. In this case, a train of overlapping pulses with a total number of repetitions $N = 5000$ each separated by an inter-train delay $T = 14ns$ excites the system. For each train the integrated relaxation rate is evaluated for $t_{\text{acquisition}} = 200$ fs and stored as a vector. As a function of the number of repetitions ($m = 0, 1, 2, \cdots, N-1$), the resulting signal exhibit modulations that oscillate at linear and non-linear combination of the modulation frequencies. This is shown in Fig. 5.4.

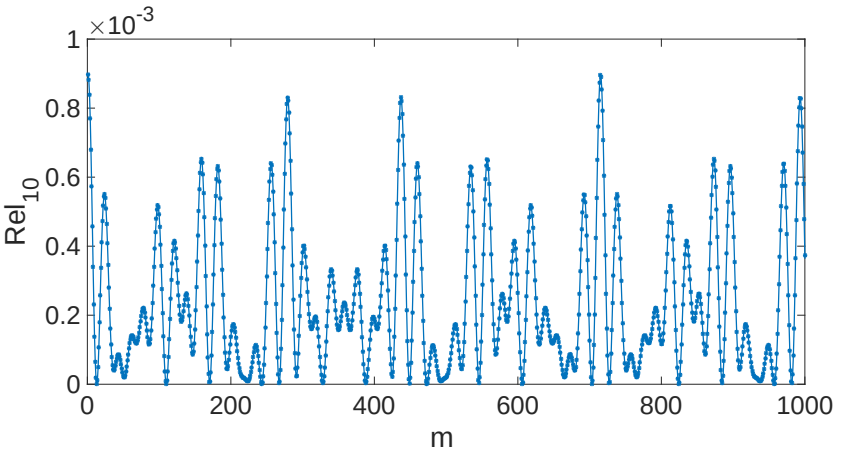

Figure 5.4: The signal from the total relaxation Rel_{10} as a function the number of repetitions m. Only 1000 repetitions are plotted.

By performing the discrete Fourier transform of the signal in Fig. 5.4, all the possible frequency components due to the linear and non-linear combinations of the modulation frequencies can be resolved.[2] The discrete Fourier transform Y of a vector, say X with length N can be computed as follows. One writes in general,

$$Y = \mathcal{F}(X), \tag{5.22}$$

such a transform is defined as

$$Y(k) = \sum_{m=0}^{N-1} X(m) e^{\frac{-2\pi imk}{N}}, \tag{5.23}$$

with an inverse transform

$$X = \mathcal{F}^{-1}(Y), \tag{5.24}$$

where

$$X(m) = \frac{1}{N} \sum_{k=0}^{N-1} Y(k) e^{\frac{2\pi imk}{N}}, \tag{5.25}$$

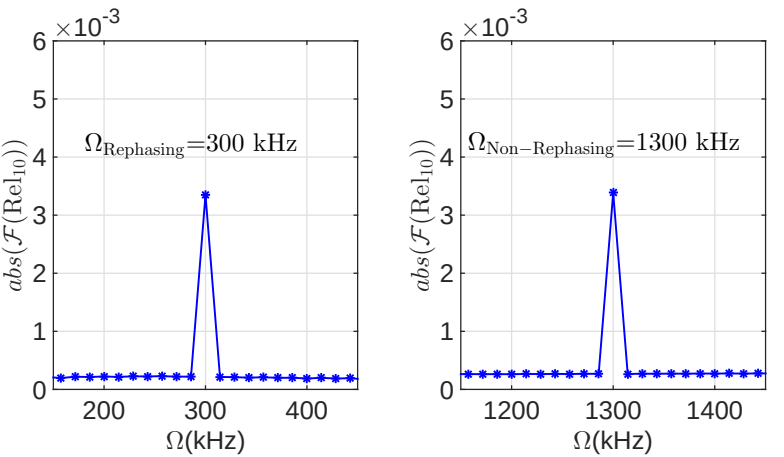

Figure 5.5: The absolute value of the Fourier transform of the signal shown in Fig. 5.4. The rephasing $\Omega = 300$ kHz and non-rephasing $\Omega = 1300$ kHz frequencies are shown.

Gathering the two dimensional data in time domain requires varying the time delays T_1 and T_3 for fixed population times T_2. For each combination of time delays (T_1, T_2, T_3),

[2]The Fourier transforms are done using the built-in fast Fourier transform of Matlab [102] software.

the rephasing (at $\Omega = \Omega_{43} - \Omega_{21} = 300kHz$) and non-rephasing (at $\Omega = \Omega_{43} + \Omega_{21} = 1300kHz$) values of the Fourier transformed complex signals are gathered from the peak values as shown in Fig. 5.5. From the complex values of the amplitudes a two dimensional data in time domain can be constructed.

Figure 5.6 shows the two dimensional time domain signals considering the sum of the total relaxation from $|1\rangle \rightarrow |0\rangle$ and $|2\rangle \rightarrow |0\rangle$.

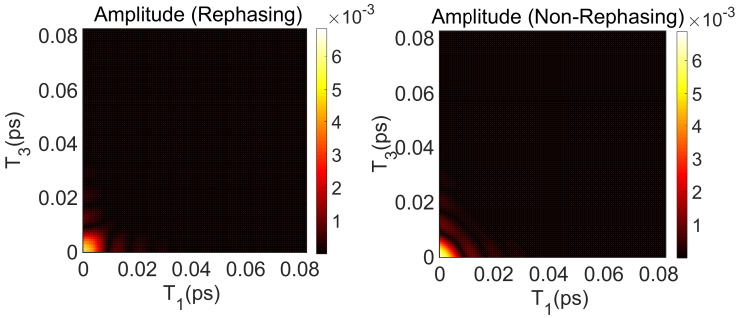

(a) Amplitude of the rephasing (left) and non-rephasing (right) signals in time domain.

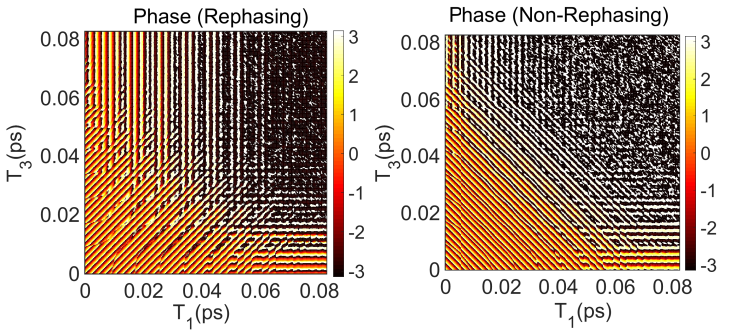

(b) Phase of the rephasing (left) and non-rephasing (right) signals in time domain.

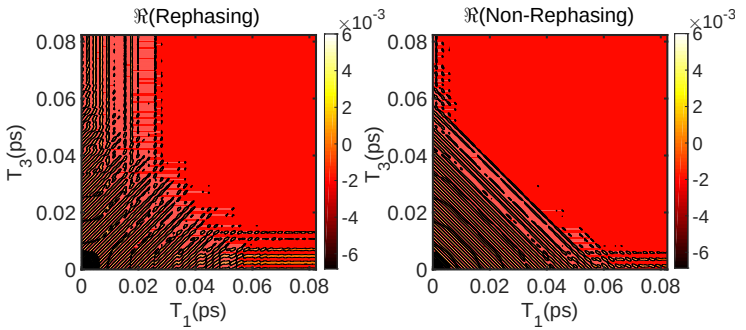

(c) Real value of the rephasing (left) and non-rephasing (right) signals in time domain.

Figure 5.6: Time domain signal for the amplitude (a) and phase (b) and real value (c) of the rephasing and non-rephasing signals.

A cut in the real part of the time domain signal either along T_1 or T_3 can reveal the oscillation frequency along these axes for the time domain signals. Fig. 5.7 shows the cut along T_1 at $T_3 = 0$. The signals for both observables in the rephasing and non-rephasing pathways are Fourier transformed to resolve the oscillation frequency. It can be seen that the signal due to the Rel_{10} observable oscillates at the resonance frequency $\omega_{10} = (E_1 - E_0)/\hbar$ and the signal due to the Rel_{20} observable oscillates at the resonance frequency $\omega_{20} = (E_2 - E_0)/\hbar$ for both rephasing and non-rephasing pathways.

A difference in the tilt (45^0) of the oscillatory features for the phase of the rephasing and non-rephasing signals can be noticed from Fig. 5.6. This originates from the fact that the coherence during T_1 has opposite sign for the rephasing and non-rephasing pathways.

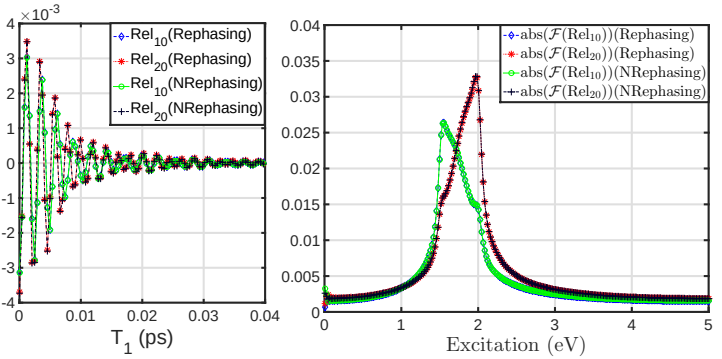

(a) The real part of the time domain signal along T_1 at $T_3 = 0$ (left) and the absolute value of the corresponding Fourier transformed data (right)

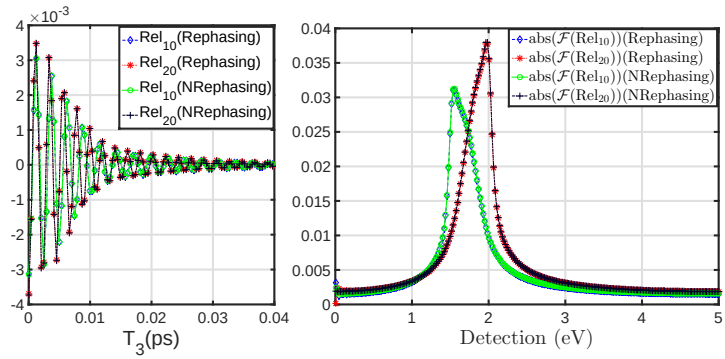

(b) The real part of the time domain signal along T_3 at $T_1 = 0$ (left) and the absolute value of the corresponding Fourier transformed data (right).

Figure 5.7: A linear scan of the real part of the time domain signal along one time axis and the corresponding Fourier transform.

The 2D spectra is obtained by Fourier transforming the time domain data shown in Fig. 5.6 in two dimensions. The axis in frequency domain[3] are labeled as 'Excitation' and 'Detection'. The excitation axis is the Fourier transform along the time T_1 and the detection axis is the Fourier transform along the time T_3.[4]

The resulting real part of the 2D spectra is shown in Fig. 5.8. Here we obtained the spectrum in their respective quadrants as discussed in the section 4.3.1 of Ref. [81]. Fourier transforming the real values of the signals result in a signal in quadrants (Excitation, Detection)=$(+,+)$ and $(-,-)$ for non-rephasing signals and in the quadrants (Excitation, Detection)=$(+,-)$ and $(-,+)$ for rephasing signals.

For the non-rephasing signal, the signal in the quadrant $(+,+)$ is symmetric to the signal in the $(-,-)$ quadrant. As a result, it is sufficient to look at only one of the two signals. A common choice is to consider the one in the $(+,+)$ quadrant. Similarly for the rephasing signal, it is sufficient to look at the $(-,+)$ quadrant due to the symmetry.

Focusing on the the signal at the quadrant $(+,+)$, it can be seen that the signals have diagonal peaks at the energies corresponding to the resonance E_2-E_0 and E_1-E_0. In addition, a small but significant off-diagonal signal due to the coherences can be observed. One of the most common ways to represent a 2D data is plotting the sum of the rephasing and non-rephasing signals to obtain a so-called *purely absorptive* (correlation) signal. Since the rephasing and non-rphasing signals lie in different quadrants of the 2D map, one has to 'flip' the rephasing signal along the excitation axis as shown in Fig. 5.8c before adding to the the non-rephasing signal. This corresponds to $(\mathrm{Excitation}, \mathrm{Detection}) \rightarrow (-\mathrm{Excitation}, \mathrm{Detection})$.

2D signals in general contain an absorptive (real) and dispersive (imaginary) signals in each dimension (excitation and detection) [81]. These absorptive and dispersive signals can not be separated easily just by taking the imaginary or the real part of the signal unlike the situation in linear spectroscopy, where it is possible to separate the absorptive and dispersive part of the signal. As a result, the 2D signal lineshapes exhibit a "phase twist" caused by the admixture of the absorptive and dispersive lineshapes [81]. These phase twisted lineshapes are shown in Fig. 5.6(a-c). The phase twists are more visible in Fig. 5.9b, where the signal due to the relaxation Rel_{10} and Rel_{20} are plotted on top of each other for better visibility of the diagonal and corss-peaks.

Often, the phase twists can complicate interpretation of spectra, specially in the case where several peaks may overlap. In such cases, it is convenient to plot the total signal by adding the rephasing and the non-rephasing with appropriate flipping. The fact that the rephasing and non-rephasing signals being in different quadrants has a consequence that the phase twists cancel when added to obtain a *purely absorptive* 2D signal [81].

[3] We changed the frequency units to energy units (eV) in all the plots.

[4] The Matlab [102] built-in fft2 function is used in a similar way as for the linear transform described.

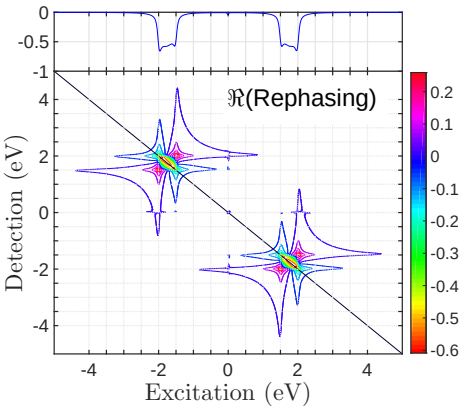

(a) Real part of rephasing signal

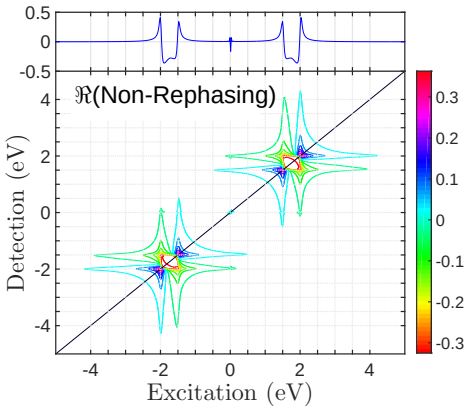

(b) Real part of non-rephasing signal

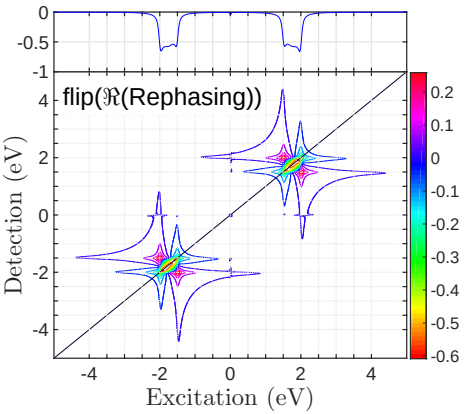

(c) Real part of the rephasing signal (flipped)

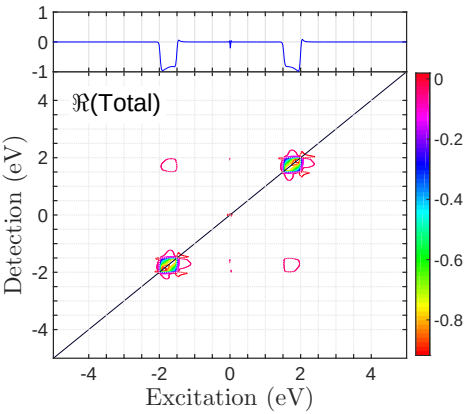

(d) Real part of the total signal

Figure 5.8: The real part of rephasing (a), non-rephasing (b), flipped rephasing (c) and total (d) Fourier transformed spectra. A cut along the anti-diagonal (a) and diagonal (b-d) is plotted on the top of each subplot.

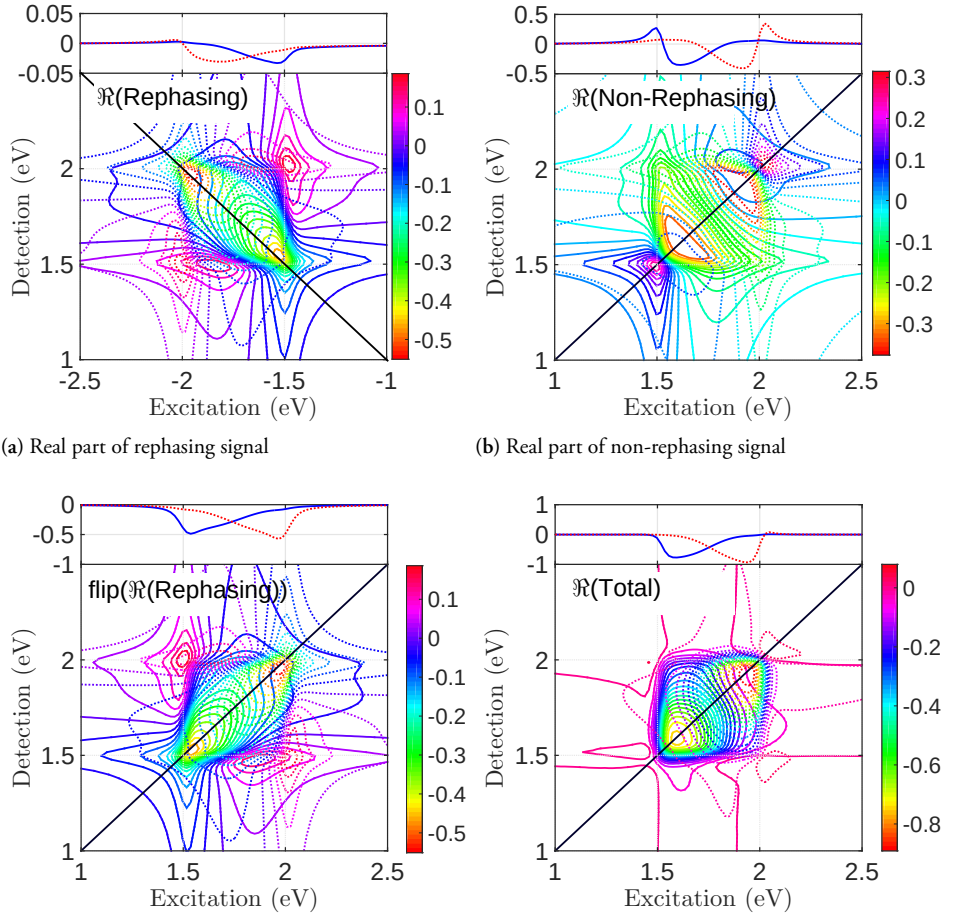

(a) Real part of rephasing signal

(b) Real part of non-rephasing signal

(c) Real part of the rephasing signal (flipped)

(d) Real part of the total signal

Figure 5.9: The real part of rephasing (a), non-rephasing (b), flipped rephasing (c) and total (d) Fourier transformed spectra. Here we focused only on one of the quadrant $(+,+)$ as the signal in the other quadrant $(-,-)$ is symmetric. A cut along the anti-diagonal (a) and diagonal (b-d) is plotted on the top of each subplot. Compared to Fig. 5.8, where the sum of the signals $\mathrm{Rel}_{10} + \mathrm{Rel}_{20}$ is plotted, here the individual total relaxations Rel_{10} (solid line) and Rel_{20} (dashed line) are plotted on top of each other for the purpose of showing the individual peaks.

5.3 Double Sided Feynman Diagrams

The action of the pulse sequences on arbitrary quantum system can be best explained by the use of the double sided Feynman diagrams [42]. In this section an introduction to the diagrams with examples on their interpretations will be given. This will help in explain-

ing the the origins of the signals obtained from the simulations. Since all the pulses are aligned in the same wave-vector direction (collinear), the $\vec{K}$ dependence of the electric field is omitted in Eq. 5.4. The electric field of the jth pulse has a general form:

$$\begin{aligned} E_j^m(t) =& \underbrace{E_{0j}^m \exp\left(\frac{-4\ln 2(t-\mathcal{T}_{j-1}-mT)^2}{\tau_2^2}\right)}_{E_{0j}(t,m)} \cos(\omega \underbrace{(t-\mathcal{T}_{j-1}-mT)}_{T_j} + 2\pi\Omega_j mT), \\ =& E_{0j}(t,m)\cos(\omega T_j + 2\pi\Omega_j mT). \end{aligned} \tag{5.26}$$

In exponential form this can be written as:

$$E_j^m(t) = \frac{E_{0j}(t,m)}{2}\Big[\exp(i(\omega T_j + 2\pi\Omega_j mT)) - \exp(-i(\omega T_j + 2\pi\Omega_j mT))\Big]. \tag{5.27}$$

Following Ref. [42], some of the rules of the diagram are:

- The density matrix is represented by two vertical lines with the bra of the density matrix being the line on the left and the ket being the line on the right.
- Time is a parameter which increases vertically from bottom to top.
- An interaction with the pulse is indicate by an arrow pointing towards or away from the vertical lines. For conveniently representing the pulse sequences as the rephasing and non-rephasing pairs we labeled the incoming and outgoing pulses by their modulation frequencies Ω.
- An arrow pointing to the left and labeled Ω_j represents the action of the first part on the right side of Eq. 5.27 i.e.

  $$\frac{E_{0j}(t,m)}{2}\exp(i(\omega T_j + 2\pi\Omega_j mT)),$$

  and an arrow pointing to the right and labeled $-\Omega_j$ represents the action of the second part on the right side of Eq. 5.27 i.e.,

  $$\frac{E_{0j}(t,m)}{2}\exp(-i(\omega T_j + 2\pi\Omega_j mT)).$$

- An incoming arrow represent absorption of a photon (excitation) and an outgoing arrow represent the opposite process of emitting a photon (de-excitation).
- The combined phase in each diagram is the sum of the individual phases for the pulse sequences involved.

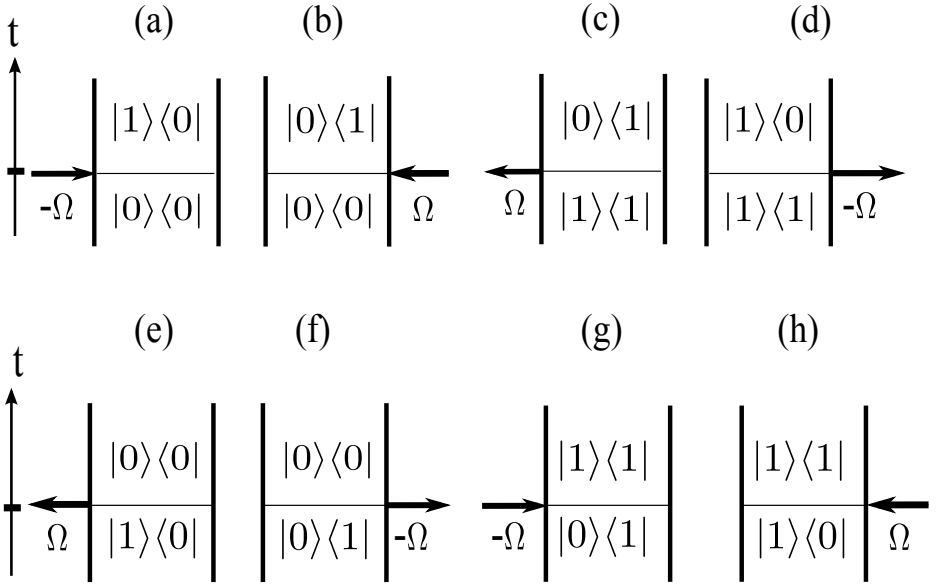

Figure 5.10: Double sided Feynman diagram showing possible actions of the pulses on populations (top) and coherences (bottom). The direction and sign of the incoming and outgoing pulses indicated by Ω are the conventions used in this thesis. For more interactions similar principle holds.

Fig. 5.10 summarizes the the diagram rules for populations ($|0\rangle\langle 0|$, $|1\rangle\langle 1|$) and coherences ($|0\rangle\langle 1|$, $|1\rangle\langle 0|$) involving two levels $|0\rangle$, $|1\rangle$. The top diagrams (a-d) show the action of a pulse on population to create coherences. For the ground state population Fig. 5.10(a) shows excitation of the system by acting on the bra of the density matrix while Fig. 5.10(b) shows excitation of the system by acting on the ket of the density matrix. Fig. 5.10(c-d) show de-exciting the population $|1\rangle\langle 1|$ by acting on the bra and ket of the density matrix. The coherences can be converted to populations by acting on the bra and ket to create population either by de-exciting Fig. 5.10(e-f) or by exciting Fig. 5.10(g-h).

In the case of four pulses, one obtains four interactions along the time axis sequentially ordered from 1-4 with time delays between each pulse. Since the ground state can not be de-excited, the first pulse does always acts inwards. In 2D fluorescent spectroscopy, since the fluorescence from an excited state is detected, the action of the fourth pulse is to put the system in an excited state. The relaxation from this excited state is the fluorescent signal [101, 103–106]. In the double sided Feynman diagram, the fluorescence is indicated by an outgoing wiggly arrow pointing outward from the population state (see Figs. 5.11, 5.12).

Below, the possible double sided Feynman diagrams for the rephasing and non-rephasing pathways for interaction of four pulses with the three level system shown in Fig. 5.3 will be

discussed. As mentioned in Eq. 5.8 the total phase in the rephasing pathway is given by

$$\Omega_{\text{Rephasing}} = \Omega_{43} - \Omega_{21} = \Omega_4 - \Omega_3 - \Omega_2 + \Omega_1,$$

and the non-rephasing pathway is

$$\Omega_{\text{Non-Rephasing}} = \Omega_{43} + \Omega_{21} = \Omega_4 - \Omega_3 + \Omega_2 - \Omega_1.$$

In both cases, the sign for the fourth pulse is positive which restricts the last pulse to point towards the left to create the final population in the excited state in all the diagrams. However, the sign for the first pulse is positive in the rephasing case and negative in the non-rephasing case. As a result all the rephasing diagrams are characterized by the first pulse pointing inwards from the right and all the non-rephasing diagrams are characterized by the first pulse pointing inwards from the left. In addition, one can also differentiate the two pathways by looking at the direction of the first and third pulse. In the case of non-rephasing, the first and the third interaction points in the same direction while for rephasing pathways they point in opposite directions.

Figure 5.12 shows the double sided Feynman diagram for the non-rephasing pathways. The different pathways are categorized as stimulated emission (SE), ground state bleaching (GSB) and quantum beating (QB) based on the action of the pulse sequences. In systems with additional high energy levels, an additional pathway associated to excited state absorption (ESA) is present. In the exciton model considered in paper IV, due to the fourth level, excited state absorption (ESA) provides a signal in the 2D spectra.

The peaks associated to the pathways are indicated in the 2D map right below each diagrams showing weather the specific pathway results in a signal contribution to the diagonal or cross peak.

The diagonal peaks are obtained by exciting and detecting with similar energy. For the model system considered here, two diagonal peaks corresponding to the excitation and detection at energies E_1 and E_2 can be obtained. On the other hand, cross peaks are obtained by exciting and detecting at different energies. Here,two cross peaks at (Excitation, Detection)=(E_1, E_2) and (Excitation, Detection)=(E_2, E_1) can be obtained for the model system.

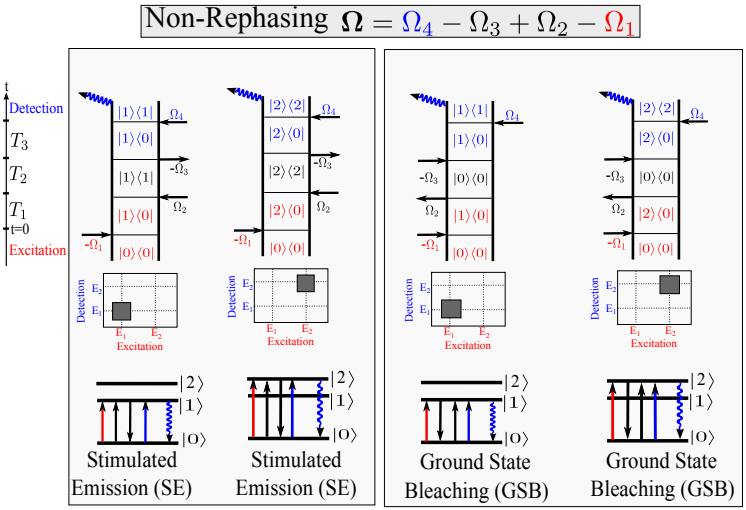

(a) Double sided Feynman diagram for non-rephasing pathway SE and GSB

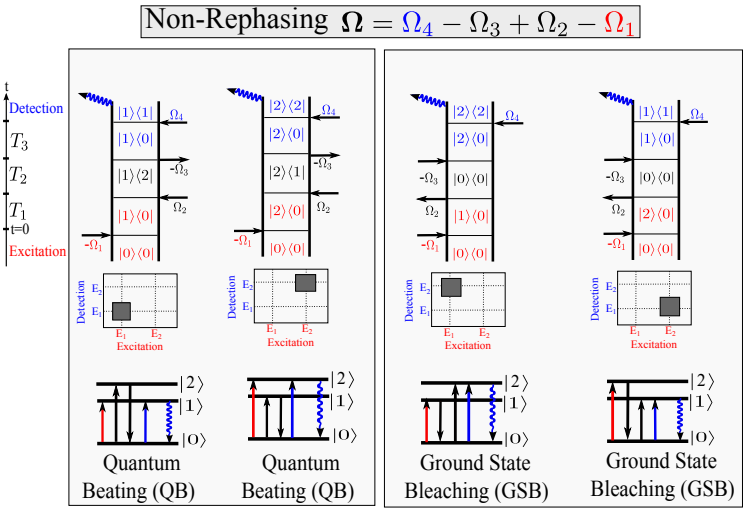

(b) Double sided Feynman diagram for non-rephasing pathway QB and GSB

Figure 5.11: Double sided Feynman diagram for the non-rephasing pathway of the three level system. Red indicates excitation and blue indicates detection processes. The 2D schematic right below the double sided Feynman diagrams indicate the peak positions for the process represented in the diagram. In addition, the action of the pulse sequences for each diagram is shown below the 2D schematics. For the three level model considered here, the non-rephasing signals mainly contribute to the diagonal peaks due to stimulated emission (SE), ground state bleaching (GSB) and quantum beating (QB) where the excitation and detection energies are equal. In addition, the signals contribute to the cross peaks due to ground state bleaching (GSB) where the excitation and detection energies are different.

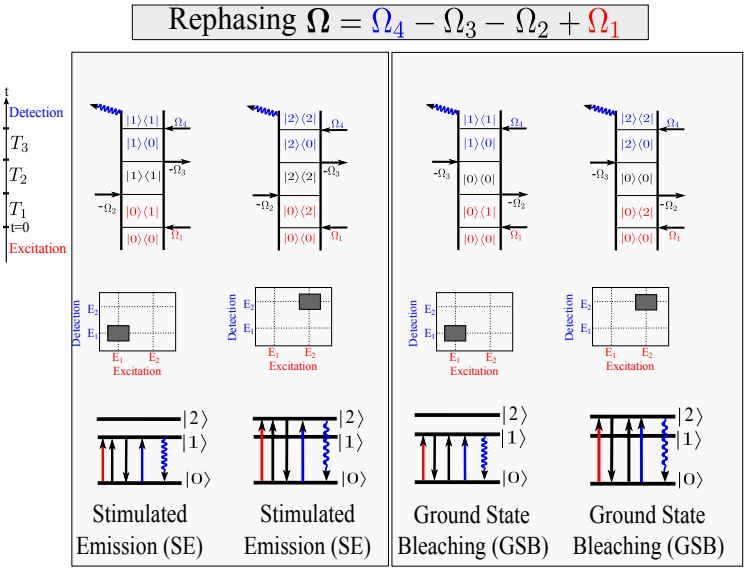

(a) Double sided Feynman diagram for rephasing pathway SE and GSB

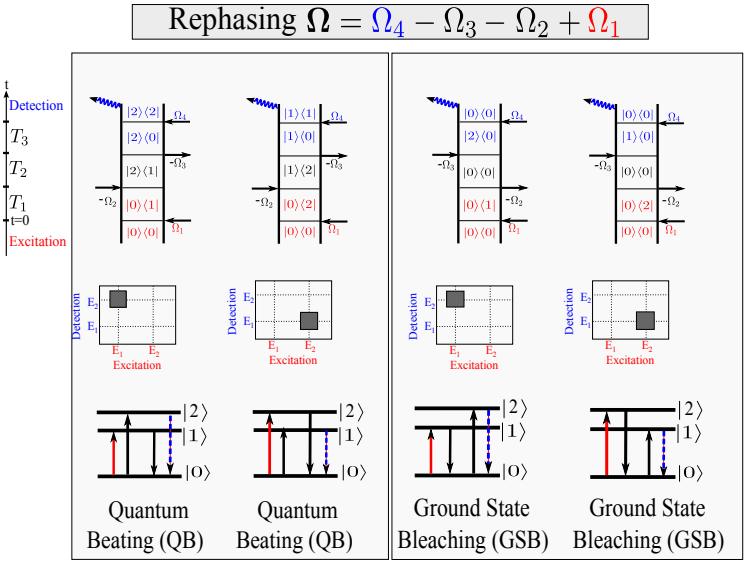

(b) Double sided Feynman diagram for rephasing pathway QB and GSB

Figure 5.12: Double sided Feynman diagram for the rephasing pathway of the three level system. Red indicates excitation and blue indicates detection processes. The 2D schematic right below the double sided Feynman diagrams indicate the peak positions for the process represented in the diagram. In addition, the action of the pulse sequences for each diagrams is shown below the 2D schematics. For the three level model considered here, the rephasing signals mainly contribute to the diagonal peaks due to stimulated emission (SE), ground state bleaching (GSB) where the excitation and detection energies are equal (a). In addition, the signals contribute to the cross peaks due to ground state bleaching (GSB) and quantum beating (QB) where the excitation and detection energies are different (b).

5.4 Study of Dynamics using 2D Spectroscopy (Paper IV)

As an application of our method for studying dynamics of a quantum system in real time, we considered a model consisting of excitons with closely spaced energies as shown in Fig. 5.13. The objective is to study the coherent beating between the two closely spaced excitons by examining the change in the diagonal and cross-peaks of the spectra as a function of population time. 2D spectroscopy has been particularly useful in investigating oscillatory beatings and their origins in coupled exciton systems [107–110]. A similar procedure as described for the three level system was used to collect and organize the data. However, in addition to the $T_2 = 0$, which was the case described in the previous sections, we explore the time dependence of the dynamics at other population times $T_2 > 0$. In order to resolve the beating frequency, the population time were varied from $T_2 = 0$ to $T_2 = 100$ fs with a time step $\Delta T_2 = 5$ fs. This provides sufficient information to observe the coherent beating with a frequency that matches the energy splitting between the two closely spaced excitons.

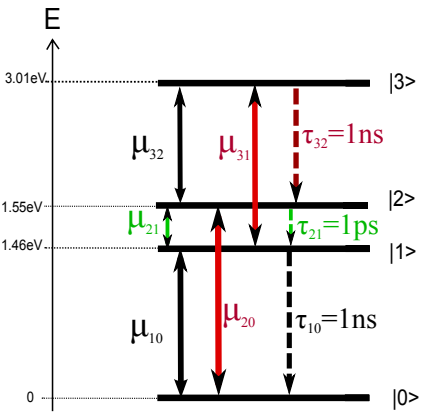

Figure 5.13: [Paper IV] Energy level diagram for the excitonic system considered in the simulation. The dipole transitions are indicated by solid double sided arrow while the relaxations are indicated by a dashed one sided arrow.

Fig. 5.14 shows the time evolution for the real part of the total, rephasing and non-rephasing signals. E_1 and E_2 indicate the energies for the two excitons. Since the total correlation signal is the sum of the rephasing and non-rephasing signals it exhibits rounded peaks compared to the rephasing and non-rephasing peaks which are elongated along the diagonal and anti-diagonal directions, respectively. The energy splitting between the two excitons is

$$\Delta E = E_2 - E_1 = 1.55 \text{ eV} - 1.4855 \text{ eV} = 91.2 \text{ meV}.$$

This corresponds to an oscillation with a period

$$T = \frac{2\pi\hbar}{\Delta E} \approx 45.35 \text{ fs}. \tag{5.28}$$

This matches the observation from Fig. 5.14 that, at $T_2 = 0$ fs the signal is maximum with a significant reduction in the amplitude around $T_2 = 15$ fs and a revival around $T_2 = 45$ fs.

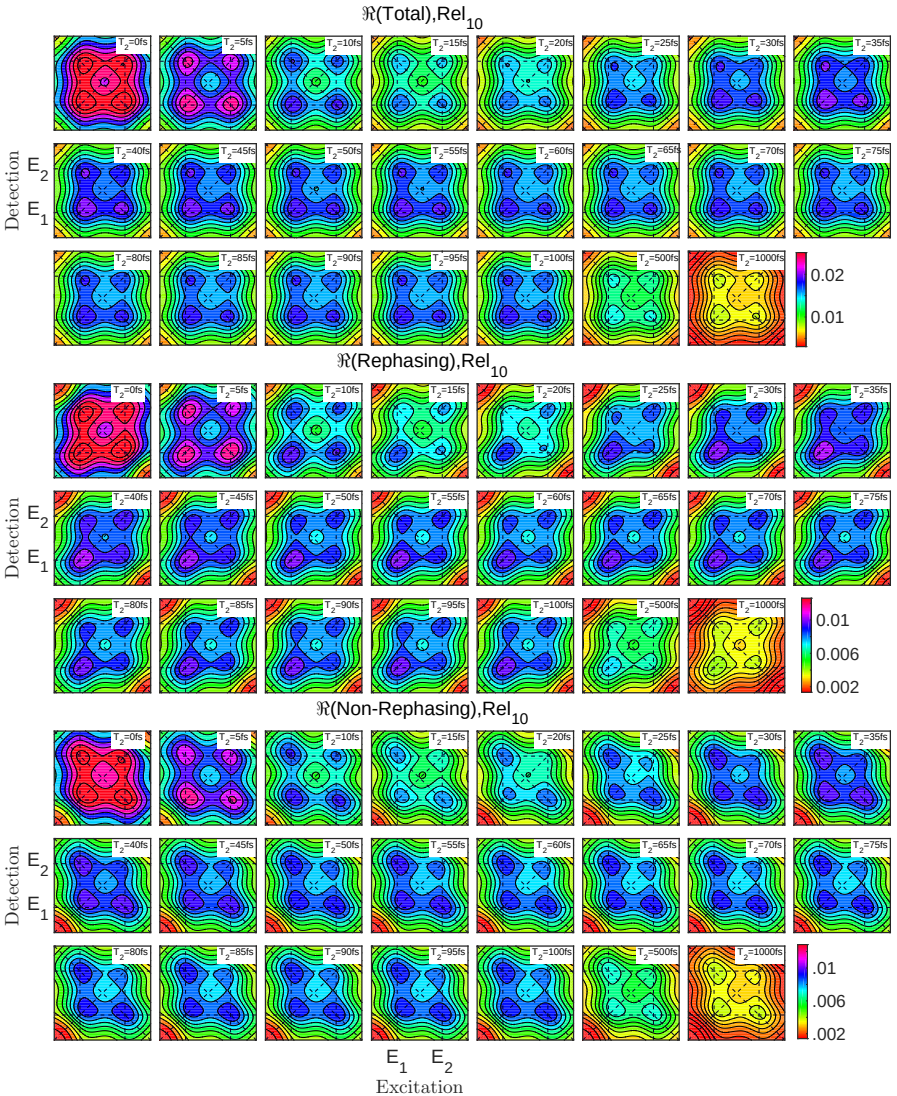

Figure 5.14: [Paper IV] Time evolution of the real part of the total, rephasing and non-rephasing signal from Rel_{10}. The population time is varied by 5fs from $T_2 = 0$ to $T_2 = 100$ fs. To see the long time behavior the spectrum at $T_2 = 500$ fs and $T_2 = 1000$ fs are also shown. In each population time T_2 the spectrum is multiplied by the maximum amplitude of the corresponding time domain data. The rephasing signals are elongated along the diagonal where as the non-rephasing signals are elongated along the anti-diagonal direction. In all the plots clear oscillation is shown as a function of population time.

Chapter 6

Discussion and Outlook

In this thesis, two different techniques of probing electron collisions in nanostructures were presented. In the first part, an enhanced transport through serially coupled triple quantum dots has been obtained due to electron-electron (ee) interactions. Here, we emphasized the importance of taking into account the different ee scattering terms into consideration while simulating current and conductance through the structure. In this regard, one could extend the problem to examine transport through more complicated setup than serially coupled dots to see if there are possible transport channels due to ee interaction which would otherwise be blocked.

The second part of the thesis described probing a quantum system with a light field to study ultrafast dynamics which occur due to ee interactions. Here the subject of multiple exciton generation (MEG) was central. We examined the situation where an initially created exciton with an energy much larger than the band gap creating a double exciton with equivalent energy. We showed that if one assumes typical parameters for a quantum dot, a quantum yield close to an experimental value can be obtained. In paper II, we calculated the yield as the number of recombinations across the band-gap per number of absorbed photons. Here as an outlook, a quantum yield for several other systems can be explored to see which materials can be used as a good candidate for solar energy harvesting.

Motivated by the good agreement of the results of paper II with experiment, we explored the condition of MEG in the case where the quantum dot is attached to external contacts in paper III. This way electrons and holes can be extracted and collected as in a realistic photovoltaic device. The yield in this case was defined as the number of extracted electrons per number of absorbed photons. A condition for optimal yield was examined and we found out that there is still a room for improved MEG yield by choosing the right type of contacts. In general, for more transparent contacts, the MEG yield can be improved to its

maximum limit, Yield ≈ 1.3, for a realistic relaxation rate. We also showed that by quick extraction, the yield can be improved as this process kills the Coulomb coupled oscillation between the single exciton and double exciton populations. As an outlook, one could explore the situation where the contacts are connected to other levels in the conduction and valence band than the band-edge states. This way simulation of more additional realistic processes can be possible.

Our method is very flexible and in principle a variety of quantum mechanical processes can be evaluated by defining an appropriate jump operators for the desired process. In all the simulations, we considered a model system with up to 8 spin degenerate single particle levels. This model captures all the important processes for MEG while taking a reasonable computational time. However, if one is interested to include more levels to describe other realistic processes, an optimization of the existing code such as parallelizing might be needed.

In paper IV, a method is developed to obtain two-dimensional spectra for studying ultrafast processes in quantum systems. Instead of calculating the response functions perturbatively as it is done in conventional 2D spectroscopy, we calculated the full density matrix in the Lindblad form and evaluated the processes associated to the different pathways fully. This way a much richer signal with all possible information can be obtained. Here, we took a model system of an exciton system which exhibits quantum beating as in excitonically coupled molecules. With our method, we obtained clear signals that showed the oscillations between the two energetically close excitons with an oscillation frequency that matches the energy splitting.

Once the method to calculate the 2D spectra is developed, various types of simulation can be carried out which will help explaining measured signals or proposing possible experiments. The possibilities to be explored via 2D spectroscopy are endless. For starters, the different pathways that contribute to the MEG signals can be studied carefully. In addition, a study of the coherent energy transfer in light harvesting complexes, which is an active area of research in efficient solar energy can be studied.

To summarize, different aspects of ee interactions and their effects in measured signals have been discussed in this thesis. It is a personal hope of the author of this thesis that, this work might contribute towards the better understanding of quantum processes in nanostructures.

References

[1] T. Perry, *CES 2015: Placing bets on the new tv technologies*, IEEE Spectrum 7 (2015), [Online; posted 07-January-2015]

[2] M. C. Beard, J. M. Luther, O. E. Semonin, and A. J. Nozik, *Third generation photovoltaics based on multiple exciton generation in quantum confined semiconductors*, Acc. Chem. Res. **46**, 1252 (2013), pMID: 23113604

[3] P. V. Kamat, *Quantum dot solar cells. the next big thing in photovoltaics*, J. Phys. Chem. Lett. **4**, 908 (2013), pMID: 26291355

[4] J. B. Sambur, T. Novet, and B. A. Parkinson, *Multiple exciton collection in a sensitized photovoltaic system*, Science **330**, 63 (2010)

[5] D. Loss and D. P. DiVincenzo, *Quantum computation with quantum dots*, Phys. Rev. A **57**, 120 (1998)

[6] T. Jamieson, R. Bakhshi, D. Petrova, R. Pocock, M. Imani, and A. M. Seifalian, *Biological applications of quantum dots*, Biomaterials **28**, 4717 (2007)

[7] D. Gammon, *Quantum dots: An optical point of view*, Nature Physics **3**, 761 (2007)

[8] M. A. Kastner, *The single-electron transistor*, Rev. Mod. Phys. **64**, 849 (1992)

[9] D. V. Averin, A. N. Korotkov, and K. K. Likharev, *Theory of single-electron charging of quantum wells and dots*, Phys. Rev. B **44**, 6199 (1991)

[10] T. A. Fulton and G. J. Dolan, *Observation of single-electron charging effects in small tunnel junctions*, Phys. Rev. Lett. **59**, 109 (1987)

[11] R. C. Ashoori, *Electrons in artificial atoms*, Nature **379**, 413 (1996)

[12] L. P. Kouwenhoven, N. C. van der Vaart, A. T. Johnson, W. Kool, C. J. P. M. Harmans, J. G. Williamson, A. A. M. Staring, and C. T. Foxon, *Single electron charging effects in semiconductor quantum dots*, Z. Phys. B - Con. Mat. **85**, 367 (1991)

[13] D. V. Averin and K. K. Likharev, *Coulomb blockade of single-electron tunneling, and coherent oscillations in small tunnel junctions*, J. Low. Temp. Phys. **62**, 345 (1986)

[14] A. D. Yoffe, *Semiconductor quantum dots and related systems: Electronic, optical, luminescence and related properties of low dimensional systems*, Adv. Phys. **50**, 1 (2001)

[15] M. C. Beard, *Multiple exciton generation in semiconductor quantum dots*, J. Phys. Chem. Lett. **2**, 1282 (2011)

[16] V. I. Klimov, *Spectral and dynamical properties of multiexcitons in semiconductor nanocrystals*, Annu. Rev. Phys. Chem. **58**, 635 (2007)

[17] W. G. van der Wiel, S. De Franceschi, J. M. Elzerman, T. Fujisawa, S. Tarucha, and L. P. Kouwenhoven, *Electron transport through double quantum dots*, Rev. Mod. Phys. **75**, 1 (2003)

[18] C. Fasth, *Transport studies of local-gate defined quantum dots in nanowires*, Ph.D. thesis, Lund University (2007)

[19] J. J. Sakurai, *Modern Quantum Mechanics* (Addison Wesley, 1993), 1st edition

[20] G. Grynberg, A. Aspect, and C. Fabre, *Introduction to Quantum Optics* (Cambridge University Press, Cambridge, 2010)

[21] W. Shockley and H. J. Queisser, *Detailed balance limit of efficiency of p-n junction solar cells*, J. Appl. Phys. **32**, 510 (1961)

[22] C. H. Henry, *Limiting efficiencies of ideal single and multiple energy gap terrestrial solar cells*, Journal of Applied Physics **51**, 4494 (1980)

[23] R. T. Ross and A. J. Nozik, *Efficiency of hot-carrier solar energy converters*, Journal of Applied Physics **53**, 3813 (1982)

[24] S. V. Boriskina, M. A. Green, K. Catchpole, E. Yablonovitch, M. C. Beard, Y. Okada, S. Lany, T. Gershon, A. Zakutayev, M. H. Tahersima, V. J. Sorger, M. J. Naughton, K. Kempa, M. Dagenais, Y. Yao, L. Xu, X. Sheng, N. D. Bronstein, J. A. Rogers, A. P. Alivisatos, R. G. Nuzzo, J. M. Gordon, D. M. Wu, M. D. Wisser, A. Salleo, J. Dionne, P. Bermel, J.-J. Greffet, I. Celanovic, M. Soljacic, A. Manor, C. Rotschild, A. Raman, L. Zhu, S. Fan, and G. Chen, *Roadmap on optical energy conversion*, Journal of Optics **18**, 073004 (2016)

[25] A. D. Vos, *Detailed balance limit of the efficiency of tandem solar cells*, Journal of Physics D: Applied Physics **13**, 839 (1980)

[26] M. J. Currie, J. K. Mapel, T. D. Heidel, S. Goffri, and M. A. Baldo, *High-efficiency organic solar concentrators for photovoltaics*, Science **321**, 226 (2008)

[27] A. Luque, A. Martí, and C. Stanley, *Understanding intermediate-band solar cells*, Nature Photonics **6**, 146 (2012)

[28] A. Nozik, *Quantum dot solar cells*, Physica E **14**, 115 (2002)

[29] B. Zhou, B. Shi, D. Jin, and X. Liu, *Controlling upconversion nanocrystals for emerging applications*, Nature nanotechnology **10**, 924 (2015)

[30] M. C. Beard, K. P. Knutsen, P. Yu, J. M. Luther, Q. Song, W. K. Metzger, R. J. Ellingson, and A. J. Nozik, *Multiple exciton generation in colloidal silicon nanocrystals*, Nano Letters **7**, 2506 (2007), pMID: 17645368

[31] R. D. Schaller and V. I. Klimov, *High efficiency carrier multiplication in PbSe nanocrystals: Implications for solar energy conversion*, Phys. Rev. Lett. **92**, 186601 (2004)

[32] X. Lan, S. Masala, and E. H. Sargent, *Charge-extraction strategies for colloidal quantum dot photovoltaics*, Nat. Mater. **13**, 233 (2014), progress Article

[33] M. L. Böhm, T. C. Jellicoe, M. Tabachnyk, N. J. L. K. Davis, F. Wisnivesky-Rocca-Rivarola, C. Ducati, B. Ehrler, A. A. Bakulin, and N. C. Greenham, *Lead telluride quantum dot solar cells displaying external quantum efficiencies exceeding 120%*, Nano Letters **15**, 7987 (2015), pMID: 26488847

[34] K. Zheng, K. Karki, K. Žídek, and T. Pullerits, *Ultrafast photoinduced dynamics in quantum dot-based systems for light harvesting*, Nano Res. **8**, 2125 (2015)

[35] M. Abdellah, R. Marschan, K. Žídek, M. E. Messing, A. Abdelwahab, P. Chábera, K. Zheng, and T. Pullerits, *Hole trapping: The critical factor for quantum dot sensitized solar cell performance*, J. Phys. Chem. C **118**, 25802 (2014)

[36] M. C. Hanna, M. C. Beard, and A. J. Nozik, *Effect of solar concentration on the thermodynamic power conversion efficiency of quantum-dot solar cells exhibiting multiple exciton generation*, The Journal of Physical Chemistry Letters **3**, 2857 (2012)

[37] A. Standard, *G173-03, (reapproved 2012), standard tables for reference solar spectral irradiances: Direct normal and hemispherical on* 37^0 *tilted surface*, ASTM International, West Conshohocken, PA (2012)

[38] R. Hanson, L. P. Kouwenhoven, J. R. Petta, S. Tarucha, and L. M. K. Vandersypen, *Spins in few-electron quantum dots*, Rev. Mod. Phys. **79**, 1217 (2007)

[39] J. N. Pedersen and A. Wacker, *Tunneling through nanosystems: Combining broadening with many-particle states*, Phys. Rev. B **72**, 195330 (2005)

[40] J. N. Pedersen, *Tunneling through Nanostructures - Interactions, Interference and Broadening*, Ph.D. thesis, Lund University (2008)

[41] O. Karlström, *Effects of Coherence and Correlations on Transport through Nanostructures*, Ph.D. thesis, Lund University (2012)

[42] S. Mukamel, *Principles of nonlinear optical spectroscopy*, volume 29 (Oxford University Press New York, 1995)

[43] A. Wacker, *Different approaches to transport through quantum systems with interaction* (2014), unpublished note version November 17, 2014

[44] A. L. Fetter and J. D. Walecka, *Quantum Theory of Many-particle Systems* (Dover Publications, 2003)

[45] G. Nylund, K. Storm, S. Lehmann, F. Capasso, and L. Samuelson, *Designed quasi-1d potential structures realized in compositionally graded inas1–xpx nanowires*, Nano Letters **16**, 1017 (2016), pMID: 26788886

[46] A. Wacker, *Semiconductor superlattices: a model system for nonlinear transport*, Phys. Rep. **357**, 1 (2002)

[47] W. W. Parson, *Resonance Energy Transfer* (Springer Berlin, 2007)

[48] H. J. Joyce, C. J. Docherty, Q. Gao, H. H. Tan, C. Jagadish, J. Lloyd-Hughes, L. M. Herz, and M. B. Johnston, *Electronic properties of gaas, inas and inp nanowires studied by terahertz spectroscopy*, Nanotechnology **24**, 214006 (2013)

[49] H. Van Amerongen, L. Valkunas, and R. Van Grondelle, *Photosynthetic excitons* (World Scientific, 2000)

[50] W. Y. Liang, *Excitons*, Physics Education **5**, 226 (1970)

[51] D. W. Snoke, *Solid State Physics: Essential Concepts* (Addison-Wesley, 2009)

[52] N. W. Ashcroft and N. D. Mermin, *Solid State Physics* (Saunders College, Philadelphia, 1976)

[53] G. D. Scholes and G. Rumbles, *Excitons in nanoscale systems*, Nature materials **5**, 683 (2006)

[54] J. Frenkel, *On the transformation of light into heat in solids. i*, Phys. Rev. **37**, 17 (1931)

[55] J. Frenkel, *On the transformation of light into heat in solids. ii*, Phys. Rev. **37**, 1276 (1931)

[56] G. H. Wannier, *The structure of electronic excitation levels in insulating crystals*, Phys. Rev. **52**, 191 (1937)

[57] I. Moreels, K. Lambert, D. Smeets, D. De Muynck, T. Nollet, J. C. Martins, F. Vanhaecke, A. Vantomme, C. Delerue, G. Allan, and Z. Hens, *Size-dependent optical properties of colloidal PbS quantum dots*, ACS Nano **3**, 3023 (2009), pMID: 19780530

[58] N. Lenngren, *Charge carrier dynamics in colloidal quantum dots tracking the dance of electrons and holes by ultrashort laser pulses*, Ph.D. thesis, Lund University (2015)

[59] I. Kang and F. W. Wise, *Electronic structure and optical properties of PbS and PbSe quantum dots*, J. Opt. Soc. Am. B **14**, 1632 (1997)

[60] D. L. Mitchell and R. F. Wallis, *Theoretical energy-band parameters for the lead salts*, Phys. Rev. **151**, 581 (1966)

[61] N. Heda, A. Rathor, V. Sharma, G. Ahmed, Y. Sharma, and B. Ahuja, *Study of electronic structure and compton profiles of PbS and PbSe*, Journal of Alloys and Compounds **463**, 47 (2008)

[62] J. O. Dimmock and G. B. Wright, *Band edge structure of PbS, PbSe, and PbTe*, Phys. Rev. **135**, A821 (1964)

[63] V. I. Klimov, *Nanocrystal quantum dots* (CRC Press, 2010)

[64] J. H. Davies, *The Physics of Low-dimensional Semiconductors: An Introduction* (Cambridge university press, 1997)

[65] K. J. Karki, F. Ma, K. Zheng, K. Zidek, A. Mousa, M. A. Abdellah, M. E. Messing, L. R. Wallenberg, A. Yartsev, and T. Pullerits, *Multiple exciton generation in nanocrystals revisited: Consistent calculation of the yield based on pump-probe spectroscopy*, Sci. Rep. **3**, 2287 (2013)

[66] K. J. Karki, J. R. Widom, J. Seibt, I. Moody, M. C. Lonergan, T. Pullerits, and A. H. Marcus, *Coherent two-dimensional photocurrent spectroscopy in a PbS quantum dot photocell*, Nat. Commun. **5**, 5869 (2014)

[67] A. J. Nozik, *Multiple exciton generation in semiconductor quantum dots*, Chem. Phys. Lett. **457**, 3 (2008)

[68] A. Shabaev, A. L. Efros, and A. J. Nozik, *Multiexciton generation by a single photon in nanocrystals*, Nano Letters **6**, 2856 (2006)

[69] M. C. Beard, A. G. Midgett, M. C. Hanna, J. M. Luther, B. K. Hughes, and A. J. Nozik, *Comparing multiple exciton generation in quantum dots to impact ionization in bulk semiconductors: Implications for enhancement of solar energy conversion*, Nano Letters **10**, 3019 (2010)

[70] R. J. Ellingson, M. C. Beard, J. C. Johnson, P. Yu, O. I. Micic, A. J. Nozik, A. Shabaev, and A. L. Efros, *Highly efficient multiple exciton generation in colloidal PbSe and PbS quantum dots*, Nano letters **5**, 865 (2005)

[71] D. Gachet, A. Avidan, I. Pinkas, and D. Oron, *An upper bound to carrier multiplication efficiency in type ii colloidal quantum dots*, Nano Letters **10**, 164 (2010), pMID: 19911830

[72] J. J. H. Pijpers, E. Hendry, M. T. W. Milder, R. Fanciulli, J. Savolainen, J. L. Herek, D. Vanmaekelbergh, S. Ruhman, D. Mocatta, D. Oron, A. Aharoni, U. Banin, and M. Bonn, *Carrier multiplication and its reduction by photodoping in colloidal inas quantum dots*, J. Phys. Chem. C **111**, 4146 (2007)

[73] R. D. Schaller, M. A. Petruska, and V. I. Klimov, *Effect of electronic structure on carrier multiplication efficiency: Comparative study of PbSe and CdSe nanocrystals*, Appl. Phys. Lett. **87**, 253102 (2005)

[74] S. K. Stubbs, S. J. O. Hardman, D. M. Graham, B. F. Spencer, W. R. Flavell, P. Glarvey, O. Masala, N. L. Pickett, and D. J. Binks, *Efficient carrier multiplication in inp nanoparticles*, Phys. Rev. B **81**, 081303 (2010)

[75] F. W. Wise, *Lead salt quantum dots: the limit of strong quantum confinement*, Acc. Chem. Res. **33**, 773 (2000), pMID: 11087314

[76] F. Träger, *Springer handbook of lasers and optics* (Springer Science & Business Media, 2007)

[77] V. I. Klimov, A. A. Mikhailovsky, D. W. McBranch, C. A. Leatherdale, and M. G. Bawendi, *Quantization of multiparticle auger rates in semiconductor quantum dots*, Science **287**, 1011 (2000)

[78] S. A. Crooker, T. Barrick, J. A. Hollingsworth, and V. I. Klimov, *Multiple temperature regimes of radiative decay in CdSe nanocrystal quantum dots: Intrinsic limits to the dark-exciton lifetime*, Appl. Phys. Lett. **82**, 2793 (2003)

[79] G. Lindblad, *On the generators of quantum dynamical semigroups*, Commun. Math. Phys. **48**, 119 (1976)

[80] H.-P. Breuer and F. Petruccione, *The Theory of Open Quantum Systems* (Oxford University Press, Oxford, 2007)

[81] P. Hamm and M. Zanni, *Concepts and methods of 2D infrared spectroscopy* (Cambridge University Press, 2011)

[82] S. Mukamel, *Multidimensional femtosecond correlation spectroscopies of electronic and vibrational excitations*, Annual Review of Physical Chemistry **51**, 691 (2000), pMID: 11031297

[83] M. Cho, *Coherent two-dimensional optical spectroscopy*, Chemical Reviews **108**, 1331 (2008), pMID: 18363410

[84] S. M. Gallagher Faeder and D. M. Jonas, *Two-dimensional electronic correlation and relaxation spectra: Theory and model calculations*, The Journal of Physical Chemistry A **103**, 10489 (1999)

[85] D. M. Jonas, *Two-dimensional femtosecond spectroscopy*, Annual Review of Physical Chemistry **54**, 425 (2003), pMID: 12626736

[86] M. Cowan, J. Ogilvie, and R. Miller, *Two-dimensional spectroscopy using diffractive optics based phased-locked photon echoes*, Chemical Physics Letters **386**, 184 (2004)

[87] J. D. Hybl, A. W. Albrecht, S. M. G. Faeder, and D. M. Jonas, *Two-dimensional electronic spectroscopy*, Chemical Physics Letters **297**, 307 (1998)

[88] J. D. Hybl, A. A. Ferro, and D. M. Jonas, *Two-dimensional fourier transform electronic spectroscopy*, The Journal of Chemical Physics **115**, 6606 (2001)

[89] D. Finkelstein-Shapiro, F. Poulsen, T. o. Pullerits, and T. Hansen, *Coherent two-dimensional spectroscopy of a fano model*, Phys. Rev. B **94**, 205137 (2016)

[90] M. Khalil, N. Demirdöven, and A. Tokmakoff, *Coherent 2d ir spectroscopy: Molecular structure and dynamics in solution*, The Journal of Physical Chemistry A **107**, 5258 (2003)

[91] T. Brixner, J. Stenger, H. M. Vaswani, M. Cho, R. E. Blankenship, and G. R. Fleming, *Two-dimensional spectroscopy of electronic couplings in photosynthesis*, Nature **434**, 625 (2005)

[92] D. B. Turner, R. Dinshaw, K.-K. Lee, M. S. Belsley, K. E. Wilk, P. M. G. Curmi, and G. D. Scholes, *Quantitative investigations of quantum coherence for a light-harvesting protein at conditions simulating photosynthesis*, Phys. Chem. Chem. Phys. **14**, 4857 (2012)

[93] G. Nardin, T. M. Autry, K. L. Silverman, and S. T. Cundiff, *Multidimensional coherent photocurrent spectroscopy of a semiconductor nanostructure*, Opt. Express **21**, 28617 (2013)

[94] S. T. Cundiff, *Coherent spectroscopy of semiconductors*, Opt. Express **16**, 4639 (2008)

[95] D. B. Turner, Y. Hassan, and G. D. Scholes, *Exciton superposition states in CdSe nanocrystals measured using broadband two-dimensional electronic spectroscopy*, Nano letters **12**, 880 (2012)

[96] T. Brixner, T. Mančal, I. V. Stiopkin, and G. R. Fleming, *Phase-stabilized two-dimensional electronic spectroscopy*, The Journal of Chemical Physics **121**, 4221 (2004)

[97] G. S. Schlau-Cohen, A. Ishizaki, and G. R. Fleming, *Two-dimensional electronic spectroscopy and photosynthesis: Fundamentals and applications to photosynthetic light-harvesting*, Chemical Physics **386**, 1 (2011)

[98] M. Cho, H. M. Vaswani, T. Brixner, J. Stenger, and G. R. Fleming, *Exciton analysis in 2d electronic spectroscopy*, The Journal of Physical Chemistry B **109**, 10542 (2005), pMID: 16852278

[99] P. F. Tekavec, T. R. Dyke, and A. H. Marcus, *Wave packet interferometry and quantum state reconstruction by acousto-optic phase modulation*, The Journal of Chemical Physics **125**, 194303 (2006)

[100] P. F. Tekavec, G. A. Lott, and A. H. Marcus, *Fluorescence-detected two-dimensional electronic coherence spectroscopy by acousto-optic phase modulation*, The Journal of Chemical Physics **127**, 214307 (2007)

[101] K. J. Karki, L. Kringle, A. H. Marcus, and T. Pullerits, *Phase-synchronous detection of coherent and incoherent nonlinear signals*, Journal of Optics **18**, 015504 (2016)

[102] MATLAB, *version 8.5.0.197613 (R2015a)* (The MathWorks Inc., Natick, Massachusetts, 2015)

[103] A. Perdomo-Ortiz, J. R. Widom, G. A. Lott, A. Aspuru-Guzik, and A. H. Marcus, *Conformation and electronic population transfer in membrane-supported self-assembled porphyrin dimers by 2d fluorescence spectroscopy*, The Journal of Physical Chemistry B **116**, 10757 (2012), pMID: 22882118

[104] G. A. Lott, A. Perdomo-Ortiz, J. K. Utterback, J. R. Widom, A. Aspuru-Guzik, and A. H. Marcus, *Conformation of self-assembled porphyrin dimers in liposome vesicles by phase-modulation 2d fluorescence spectroscopy*, Proceedings of the National Academy of Sciences **108**, 16521 (2011)

[105] J. M. Dawlaty, A. Ishizaki, A. K. De, and G. R. Fleming, *Microscopic quantum coherence in a photosynthetic-light-harvesting antenna*, Philosophical Transactions of the Royal Society of London A: Mathematical, Physical and Engineering Sciences **370**, 3672 (2012)

[106] A. K. De, D. Monahan, J. M. Dawlaty, and G. R. Fleming, *Two-dimensional fluorescence-detected coherent spectroscopy with absolute phasing by confocal imaging of a dynamic grating and 27-step phase-cycling*, The Journal of Chemical Physics **140**, 194201 (2014)

[107] J. Seibt and T. Pullerits, *Beating signals in 2d spectroscopy: Electronic or nuclear coherences? application to a quantum dot model system*, The Journal of Physical Chemistry C **117**, 18728 (2013)

[108] G. S. Engel, T. R. Calhoun, E. L. Read, T.-K. Ahn, T. Mancal, Y.-C. Cheng, R. E. Blankenship, and G. R. Fleming, *Evidence for wavelike energy transfer through quantum coherence in photosynthetic systems*, Nature **446**, 782 (2007)

[109] D. Egorova, *Oscillations in two-dimensional photon-echo signals of excitonic and vibronic systems: Stick-spectrum analysis and its computational verification*, The Journal of Chemical Physics **140**, 034314 (2014)

[110] A. Ishizaki and G. R. Fleming, *On the interpretation of quantum coherent beats observed in two-dimensional electronic spectra of photosynthetic light harvesting complexes*, The Journal of Physical Chemistry B **115**, 6227 (2011), pMID: 21488648

Printed by Media-Tryck, Lund 2017 NORDIC ECOLABEL, 3041 0903

Lund University
Faculty of Science
Department of Physics
ISBN 978-91-7753-206-4